

# Development Of Microreactor Technology For Partial Oxidation Of Ethanol on Gold Catalyst

*Erfan Behravesh*



Laboratory of Industrial Chemistry and Reaction Engineering  
Faculty of Science and Engineering/Chemical Engineering  
Åbo Akademi University

2019





Erfan Behravesht

Born 1987, Mashhad, Iran

M.Sc. Chemical Engineering 2014

Åbo Akademi University, Turku/Åbo, Finland

# Development of microreactor technology for partial oxidation of ethanol on gold catalyst

*Erfan Behravesh*



Johan Gadolin  
Process Chemistry Centre

Laboratory of Industrial Chemistry and Reaction Engineering  
Faculty of Science and Engineering/Chemical Engineering  
Åbo Akademi University  
Turku/Åbo, Finland, 2019

### ***Supervised by***

Academy Professor, Dr. Tapio Salmi

Professor, Dr. Dmitry Yu. Murzin

Docent, Dr. Narendra Kumar

Laboratory of Industrial Chemistry and Reaction Engineering

Faculty of Science and Engineering / Chemical Engineering

Åbo Akademi University

Åbo/Turku, Finland

### ***Reviewers***

Professor, Dr. Lars Pettersson

Royal Institute of Technology (KTH)

Stockholm, Sweden

*and*

Research Professor, Dr. Juha Lehtonen

VTT

Espoo, Finland

### ***Opponent***

Professor, Dr. Lars Pettersson

Royal Institute of Technology (KTH)

Stockholm, Sweden

ISBN 978-952-12-3896-3 (printed version)/ISBN 978-952-12-3897-0 (online version)

ISSN 2669-8315 (printed version)/ISSN 2670-0638 (online version)

(*Acta technologiae chemicae Aboensia 2019 A/3*), Painosalama Oy Turku/Åbo 2019

*To my mother,  
in heaven...*



*“It was morning and the new sun sparkled gold across the ripples of a gentle sea”*

*- Jonathan Livingston Seagull*





## Preface

Undertaking this doctoral dissertation has been a truly life-changing experience for me and it would not have been possible to do without the support and guidance that I received from many people.

First, I would like to express my sincere gratitude to Professor Tapio Salmi for giving me the opportunity to carry out my doctoral studies under his supervision. When great intelligence and knowledge as well as open mindedness and kindness gather in a scientist, science will definitely not go to a wrong direction. It was a privilege for me to be mentored by Tapio as a person who dedicated his life to science. I owe a very important debt to Professor Dmitry Yu. Murzin for the inspiration, sharing knowledge and experience, and all the consultations. Dmitry was more than a great scientist to me, he was my teacher.

I would like to thank Docent Narendra Kumar for all the generous supports I received from him towards the catalyst preparation and characterization. Gold would not have been valuable for us without his support. Docent Kari Eränen is gratefully acknowledged for the instrumentation and analyses. Systems could be barely calibrated without him! I would like to thank Dr. Teuvo Kilpiö, Dr. Vincenzo Russo and Professor Johan Wärnå for their contributions in the kinetic modellings and simulations, Professor Karoliina Honkala and Dr. Marko Melander from University of Jyväskylä for the contributions in the Density Functional Theory studies as well as Dr. Atte Aho and Professor Jyri-Pekka Mikkola for the contributions in the catalyst characterization.

It was an honor for me to perform part of my research at Institute of Micro Process Engineering (IMVT), Karlsruhe Institute of Technology (KIT) in Germany, 2018. For that, I would like to thank Professor Roland Dittmeyer for the opportunity he gave me to work in his group and Dr. Michael Klumpp, the group leader of microreactor coating for all the support and guidance during my stay from the weekly scientific meetings to the rock climbing lessons.

I was very lucky to work in a very international and fruitful environment meeting great people who are now more than colleagues to me. I am very grateful to Adriana, Nemanja, Pasi and Ricardo for the support, encouragement and all the good moments we had together. I am very thankful particularly to Hoorah, Ali, Amin, Soudabeh, Zuzana, Jussi and Ekaterina. I want to specifically thank Suvi for all the caring and sharing.

I am very thankful also to the Finnish society and more specifically Åbo Akademi for hosting me for over eight years. Living in such a great country changed my attitude towards life, which has been among the most valuable gifts I have ever received. Finland has become my second home and I hope that one day I will have the opportunity to serve the country.

Last but not least, my deepest appreciation goes to my family. I am deeply grateful to my parents and my brother for all the supports and encouragements they provided me during all these years of separation. My mother passed away from cancer while I was writing my doctoral dissertation. However, the cruel cancer was too weak to change her attitude towards life: devotion and love. My thesis is dedicated to her with honor.



## Abstract

Oxidation of alcohols from biological origin is of significant industrial relevance for the production of fine and specialty chemicals. Aldehydes from polyols are important intermediates in pharmaceutical and alimentary industries. Gold nanoparticles dispersed on porous materials are effective catalysts in the oxidation of hydroxyl ( $-OH$ ) to carbonyl groups ( $C=O$ ) in the presence of environmentally friendly oxidizers such as molecular oxygen. Microreactors are suitable tools for especially oxidation reactions because of having excellent heat and mass transfer properties due to a high surface-to-volume ratio. The importance of microreactors lies in their small size causing a remarkable drop in capital and energy costs along with positive environmental impacts.

In this work, a range of gold catalysts supported on zeolites and oxides were synthesized via a deposition-precipitation method. The effects of the surface charge as well as the pH of the solution on the gold particle size and loading were investigated. Moreover, the effect of gold deposition on the support acidity was revealed.

Both a fixed bed and a microreactor were used for the partial oxidation of ethanol at atmospheric pressure and temperature range of 100–250°C. Catalyst screening was conducted using neat and gold-supported catalysts in the fixed bed reactor. The activities and the selectivities of the catalysts were discussed taken into account the effect of gold particle size and the support acidity.

Two catalytic coating methods of microreactor elements were developed using an  $Au/Al_2O_3$  catalyst selected from the screening step as one of the most promising catalysts in terms of the activity and selectivity to the desired products. The first coating method was based on the use of a catalyst slurry. The advantage of this coating method lies in using a pre-prepared  $Au/Al_2O_3$  catalyst without incorporation of any binders, addressing the importance of the interplay between the catalyst particle size and the slurry viscosity in the optimization of the uniformity, stability and thickness of the coating layer. The second method was inkjet printing. In this method, the alumina suspension was first printed into the microchannels followed by gold deposition via a deposition-precipitating step. This method has the advantage of a higher precision but a more complicated chemistry since additives are needed.

A model was generated to explain the experimentally observed fixed bed reactor behavior in the ethanol oxidation on gold nanoparticles. The model for this heterogeneously catalyzed gas-phase multireaction system consisted of dynamic mass and energy balances as well as Langmuir–Hinshelwood–Hougen–Watson (LHHW), Mars van Krevelen and power law expressions for the reaction kinetics. The gas fluid flow was described with convection and dispersion terms. The axial and radial concentration and temperature profiles inside the reactor and the concentration profiles within the catalyst particles were predicted by the model. The estimated parameters were the rate constants and the activation energies as well as the adsorption parameters for LHHW and Mars van Krevelen kinetics and reaction order of oxygen for power

law kinetics. Numerical simulations were performed to illustrate the influence of the feed temperature and the catalyst loading as well as the effect of Péclet number on the obtained results.

A detailed modelling work was performed for the microreactor which resulted in a kinetic model for the reaction system. Dynamic mass balance-based generic modelling was applied to estimate the rate parameters from the experiments obtained with the microreactor. The aim of the study was to find out the operation conditions that favor the generation of the desired oxidation product.

Finally, molecular modelling computations at the DFT level were carried out to elucidate the reaction mechanism of the oxidative dehydrogenation of ethanol. Using the mechanism inspired by the computational studies, an improved kinetic model was developed by revisiting the previous data obtained with the microreactor to explain the measured rates of acetaldehyde formation. Moreover, the concentration profiles in the catalyst particles and layers were calculated numerically to evaluate the role of internal diffusion in the catalyst pores. The simulation results indicated the absence of internal mass transfer limitations for catalyst layer thicknesses less than 200  $\mu\text{m}$ .

## Referat

Oxidation av alkoholer av biologiskt ursprung har en hög industriell relevans för produktion av fin- och specialkemikalier. Aldehyder som härstammar från polyalkoholer är viktiga mellanprodukter för farmaceutisk industri och livsmedelsindustri. Nanopartiklar av guld dispergerade på porösa material är effektiva katalysatorer för oxidation av hydroxylgrupper ( $-OH$ ) till karbonylgrupper ( $C=O$ ) i närvaro av miljövänliga oxidationsmedel som molekylärt syre. Mikrostrukturerade reaktorer är lämpliga verktyg speciellt för studier av oxidationsprocesser, eftersom mikroreaktorer har utmärkta mass- och värmeöverföringsegenskaper, då förhållandet yta till volym har ett högt värde i mikrokanaler. En viktig aspekt vid tillämpningen av mikroreaktorer är deras minimala storlek, vilket leder till en avsevärd minskning i kapital- och energikostnaderna samt till positiva miljöeffekter.

I detta arbete syntetiserades en serie av guldkatalysatorer på zeolit- och oxidbärrmaterial med hjälp av deponering-utfällningsmetoden. Effekten av ytladdningen och lösningens pH på guldpartikelstorleken och metallhalten studerades ingående. Dessutom undersöktes gulddeponeringens effekt på bärrmateriallets surhet.

En konventionell packad bädd och en mikroreaktor användes för att partiellt oxidera etanol vid atmosfäriskt tryck inom temperaturintervallet 100–250°C. En omfattande kartläggning av olika katalysatorer genomfördes med ursprungliga bärrmaterial och guldkatalysatorer på bärrmaterial i den packade bäddreaktorn. Katalysatorernas aktivitet och selektivitet diskuterades speciellt med tanke på effekten av guldnanopartiklarnas storlek och bärrmateriallets surhet.

Två olika beläggningsmetoder för mikroreaktorelement utvecklades för en aluminiumoxidburen guldkatalysator ( $Au/Al_2O_3$ ) som hade valts på basis av en omfattande kartläggning av olika guldkatalysatorer. Den valda katalysatorn uppvisade en hög aktivitet och god selektivitet i avseende på önskade reaktionsprodukter. Den första beläggningsmetoden baserade sig på användning av en finfördelad suspension. Fördelen med denna beläggningsmetod ligger i användning av en färdigt preparerad  $Au/Al_2O_3$ -katalysator utan att bindemedel behöver inkorporeras. De viktigaste faktorerna i prepareringsprocessen är växelverkan mellan katalysatorpartikelns storlek och dispersionens viskositet då det gäller att optimera jämnheten, stabiliteten och tjockleken av katalysatorskiktet. Den andra metoden var bläcksprutning (*inkjet printing*). Enligt denna metod sprutas aluminiumoxidsuspensionen in i mikrokanaler varefter guld införs med deponering-utfällningsteknik. Fördelen med metoden är en hög precision men nackdelen är ett mer komplicerat kemiskt förfarande p.g.a. att tillsatsmedel behövs.

En matematisk modell skapades för att förklara det experimentellt observerade beteendet av packade bäddreaktorn som användes för att oxidera etanol på guldnanopartiklar. Modellen för detta heterogent katalyserade multireaktionssystem i gasfas bestod av dynamiska mass- och energibalanser. Reaktionskinetiska uttryck som användes i balansekvationerna var Langmuir–Hinshelwood–Hougen–

Watsons hastighetsekvation (LHHW), Mars-van-Krevelens kinetik samt potenslag. Gasströmmen beskrevs med konvektions- och dispersionstermer. Modellen var kapabel att prediktera axiella och radiella koncentrations- och temperaturprofiler i reaktorbädden samt koncentrationsprofiler inne i katalysatorpartiklar. De estimerade parametrarna var hastighetskonstanter, aktiveringsenergies och adsorptionsparametrar för LHHW- och Mars-van-Krevelen-kinetik samt reaktionsordningen i avseende på syrets koncentration för potenslagen. Numeriska simuleringsstudier genomfördes för att illustrera inverkan av tillflödets temperatur, katalysatormängden och Péclettalet på de erhållna resultaten.

Ett detaljerat modelleringsarbete genomfördes för mikroreaktorn, vilket resulterade i en kinetisk beskrivning av reaktionssystemet. Dynamisk modellering baserad på massbalanserna tillämpades på estimering av hastighetsparametrar för experimentella data som hade framtagits med mikroreaktorn. Målet för studiet var att finna sådana driftsbetingelser som gynnar bildningen av den önskade oxidationsprodukten.

I arbetets slutskede utnyttjades molekylär modellering på DFT-nivå för att belysa reaktionsmekanismen för oxidativ dehydrogenering av etanol. Genom att utnyttja en mekanism som var inspirerad av de teoretiska beräkningarna utvecklades en förbättrad kinetisk modell och tidigare data som erhållits med mikroreaktorn utnyttjades för att förklara experimentellt observerade hastigheter för bildning av acetaldehyd som huvudprodukt i reaktionsprocessen. Koncentrationsprofiler i katalysatorpartiklar och katalysatorskikt beräknades numeriskt för att utvärdera den interna diffusionens betydelse i katalysatorporerna. Simuleringsresultaten indikerade frånvaron av internt massöverföringsmotstånd för katalysatorskikt som är tunnare än 200  $\mu\text{m}$ .

## List of publications

- I. **E. Behraves**, N. Kumar, Q. Balme, J. Roine, J. Salonen, A. Schukarev, J-P. Mikkola, M. Peurla, A. Aho, K. Eränen, D. Yu. Murzin, T. Salmi, Synthesis and characterization of Au nanoparticles supported catalysts for partial oxidation of ethanol: Influence of structure and acidity of supports, *Journal of Catalysis*, 353 (2017) 223–238
- II. **E. Behraves**, N. Kumar, M. Peurla, A. Aho, K. Eränen, D. Yu. Murzin, T. Salmi, Microreactor coating with heterogeneous gold catalyst for partial oxidation of ethanol: Physico-chemical characterization and evaluation of catalytic properties, *Chemical Engineering Journal*, 378 (2019) 122179–122195
- III. T. Kilpiö, **E. Behraves**, V. Russo, K. Eränen, T. Salmi, Physical modelling of the laboratory scale packed bed reactor for partial gas phase oxidation of alcohol using gold nanoparticles as the heterogeneous catalyst, *Chemical Engineering Research and Design*, 117 (2017) 448–459
- IV. **E. Behraves**, T. Kilpiö, V. Russo, K. Eränen, T. Salmi, Experimental and modelling study of partial oxidation of ethanol in a microreactor using gold nanoparticles as the catalyst, *Chemical Engineering Science*, 176 (2018) 421–428
- V. **E. Behraves**, M. Malender, J. Wärnå, T. Salmi, K. Honkala, D. Yu. Murzin, Aerobic oxidation of ethanol on gold: Combination of experiments and computations to reveal the reaction mechanism, (*submitted*)

## Contribution of the author to the publications

- I. Performed all the experiments, wrote and edited the article
- II. Performed all the experiments, wrote and edited the article
- III. Performed all the experiments, contributed to writing and editing the article
- IV. Performed all the experiments, contributed to writing and editing the article
- V. Performed all the experiments, contributed to writing and editing the article

## List of related publications

- I. **E. Behraves**, N. Kumar, M. Peurla, A. Aho, K. Eränen, D. Yu. Murzin, T. Salmi, Micro-reactor coating with heterogeneous Au/Al<sub>2</sub>O<sub>3</sub> catalyst. 68<sup>th</sup> Canadian Chemical Engineering Conference, October 2018, Toronto, Canada – *Oral presentation*
- II. **E. Behraves**, N. Kumar, M. Peurla, A. Aho, K. Eränen, D. Yu. Murzin, T. Salmi, Au-based catalyst coatings in microstructured reactor for partial oxidation of ethanol. 15<sup>th</sup> International Conference on Microreaction Technology (IMRET), October 2018, Karlsruhe, Germany – *Oral presentation*
- III. **E. Behraves**, N. Kumar, M. Peurla, A. Aho, K. Eränen, D. Yu. Murzin, T. Salmi, Micro reactor coating for partial oxidation of ethanol. 23rd International Congress of Chemical and Process Engineering (CHISA), August 2018, Prague, Czech Republic – *Oral presentation*
- IV. **E. Behraves**, N. Kumar, M. Peurla, A. Aho, K. Eränen, D. Yu. Murzin, Preparation and characterization of Au/Al<sub>2</sub>O<sub>3</sub>-based microreactors for oxidation of ethanol. 10<sup>th</sup> World Congress of Chemical Engineering, October 2017, Barcelona, Spain – *Oral presentation*
- V. **E. Behraves**, N. Kumar, Q. Balme, J. Roine, J. Salonen, A. Schukarev, J-P. Mikkola, M. Peurla, A. Aho, K. Eränen, D. Yu. Murzin, T. Salmi, Synthesis and characterization of Au nanoparticles for ethanol oxidation: Effect of acidity and support structure. American Institute of Chemical Engineers (AIChE), November 2016, San Francisco, California, USA – *Poster presentation*
- VI. T. Kilpiö, **E. Behraves**, V. Russo, K. Eränen, T. Salmi, Modelling of the laboratory-scale packed bed reactor for partial gas-phase oxidation of alcohol using Au nanoparticles as the catalyst. 22<sup>nd</sup> International Congress of Chemical and Process Engineering (CHISA), August 2016, Prague, Czech Republic – *Poster presentation*
- VII. **E. Behraves**, N. Kumar, Q. Balme, J. Roine, J. Salonen, A. Schukarev, J-P. Mikkola, M. Peurla, A. Aho, K. Eränen, D. Yu. Murzin, T. Salmi, Gold catalyst screening studies for partial oxidation of ethanol. 17<sup>th</sup> Nordic Symposium on Catalysis, June 2016, Lund, Sweden – *Poster presentation*
- VIII. T. Kilpiö, **E. Behraves**, V. Russo, K. Eränen, T. Salmi, Models for continuously operating laboratory-scale reactor for partial oxidation of ethanol using heterogeneous gold catalyst. 17<sup>th</sup> Nordic Symposium on Catalysis, June 2016, Lund, Sweden – *Poster presentation*
- IX. **E. Behraves**, N. Kumar, K. Eränen, D. Yu. Murzin, T. Salmi, A kinetic experiment study on partial oxidation of ethanol using fixed bed tubular reactor. European Symposium on Chemical Reaction Engineering (ESCRE), October 2015, Munich, Germany – *Poster presentation*

X.T. Kilpiö, E. Behraves, V. Russo, K. Eränen, T. Salmi, Modelling of a laboratory scale packed bed reactor: Partial oxidation of ethanol as the model system. 10<sup>th</sup> European Congress of Chemical Engineering (ECCE), October 2015, Nice, France – *Poster presentation*

## **Prizes**

Best poster award for the research on microreactor coating, PCC annual meeting (Johan Gadolin Process Chemistry Centre), November 2018, Turku/Åbo, Finland

## Table of contents

|  |           |
|--|-----------|
| <b>1. Introduction</b> .....   | <b>1</b>  |
| 1.1. Partial oxidation of ethanol .....  | 1         |
| 1.2. Catalysis by gold .....   | 3         |
| 1.3. Microreactor technology .....   | 4         |
| 1.4. Research objectives .....   | 6         |
| <b>2. Experimental</b> .....   | <b>8</b>  |
| 2.1. Chemicals .....   | 8         |
| 2.2. Catalyst preparation.....   | 8         |
| 2.3. Catalyst slurry preparation for microplatelet coating (the first method)..... | 8         |
| 2.4. Microplatelet coating via the slurry method.....                              | 9         |
| 2.5. Catalyst ink preparation for microplatelets coating (the second method).....  | 9         |
| 2.6. Microplatelet coating via inkjet printing .....                               | 9         |
| 2.7. Catalyst and coated microplatelet characterization .....                      | 10        |
| 2.7.1. Nitrogen adsorption .....   | 10        |
| 2.7.2. X-ray diffraction (XRD) .....   | 10        |
| 2.7.3. Fourier transform infrared spectroscopy (FTIR) .....                        | 10        |
| 2.7.4. Scanning electron microscopy (SEM) .....                                    | 11        |
| 2.7.5. Laser diffraction.....  | 11        |
| 2.7.6. Surface charge measurements.....  | 11        |
| 2.7.7. Viscosity measurements.....   | 11        |
| 2.7.8. Transmission electron microscopy (TEM) .....                                | 11        |
| 2.7.9. Energy dispersive X-ray analysis (EDX).....                                 | 12        |
| 2.7.10. Inductively Coupled Plasma-Optical Emission Spectroscopy (ICP-OES).....    | 12        |
| 2.7.11. X-ray photoelectron spectroscopy (XPS) .....                               | 12        |
| 2.8. Catalytic experiments.....  | 13        |
| 2.8.1. Reactors system.....  | 13        |
| 2.8.2. Basic calculations.....   | 16        |
| <b>3. Results and discussion</b> .....   | <b>18</b> |
| 3.1. Catalyst preparation, characterization and screening .....                    | 18        |
| 3.1.1. Effect of Au deposition on the acidity of the catalysts .....               | 18        |
| 3.1.2. Effect of solution pH on Au particle size and size distribution .....       | 20        |
| 3.1.3. Effect of pH of the solution on Au loading and catalyst surface area .....  | 22        |

|           |   |           |
|-----------|---|-----------|
| 3.1.4.    | Catalysts activity .....  | 22        |
| 3.1.5.    | Catalysts selectivity .....   | 24        |
| 3.2.      | Catalytic coating of the microreactor.....                              | 27        |
| 3.2.1.    | First approach: slurry-based method .....                               | 27        |
| 3.2.1.1.  | Catalyst particle size .....  | 28        |
| 3.2.1.2.  | Viscosity of the catalyst slurry .....                                  | 28        |
| 3.2.1.3.  | Effect of ageing on acidity and structure of the catalyst support ..... | 29        |
| 3.2.1.4.  | Catalyst layer uniformity.....  | 30        |
| 3.2.1.5.  | Catalyst layer thickness.....   | 31        |
| 3.2.1.6.  | Catalyst layer stability, durability and regeneration studies .....     | 32        |
| 3.2.2.    | Second approach: inkjet printing.....                                   | 37        |
| 3.2.3.    | Comparison between the two coating methods .....                        | 39        |
| 3.3.      | Kinetic modelling of ethanol oxidation in the fixed bed reactor .....   | 41        |
| 3.3.1.    | Kinetic modelling .....   | 44        |
| 3.3.2.    | Parameter estimation results .....                                      | 45        |
| 3.3.3.    | Simulation studies .....  | 47        |
| 3.4.      | Kinetic modelling of ethanol oxidation in the microreactor.....         | 48        |
| 3.4.1.    | Kinetic modelling .....   | 48        |
| 3.4.2.    | Concentration profiles .....  | 52        |
| 3.5.      | Reaction mechanism by DFT studies .....                                 | 53        |
| 3.5.1.    | Role of oxygen: an experimental investigation .....                     | 55        |
| 3.5.2.    | Kinetic modelling .....   | 56        |
| 3.5.3.    | Reaction and diffusion in the porous catalyst layer.....                | 60        |
| <b>4.</b> | <b>Conclusions .....</b>  | <b>64</b> |
| <b>5.</b> | <b>Notation .....</b>   | <b>67</b> |
| <b>6.</b> | <b>Acknowledgements .....</b>   | <b>70</b> |
| <b>7.</b> | <b>References .....</b>   | <b>71</b> |



# **1. Introduction**



# 1. Introduction

## 1.1. Partial oxidation of ethanol

Selective oxidation of primary and secondary alcohols to the corresponding aldehydes, ketones and carboxylic acids is of great importance both from technological and fundamental point of view being widely applied in organic synthesis related to alimentary and pharmaceutical industries [1–3]. Among various alcohols, ethanol obtained from a renewable source can contribute to decrease in the use of fossil (fuel) reserves [4]. A recent report regarding the global energy transformation by IRENA (International Renewable Energy Agency) predicted that by 2050 the share of renewable energy in power generation would be 85%, compared to an estimated value of 25 % in 2017. Even if the composition of renewable energy mixture would change, from one dominated by bioenergy to one controlled by solar and wind-based energies (over half of renewable energy), bioenergy would continue to account for about one-third of the renewable consumption by 2050 [5]. Ethanol is typically produced from biomass via fermentation and used e.g., in fuels, solvents, fuel cells, and as a feedstock for producing bulk chemicals via selective oxidation [6].

The main product of ethanol oxidation is acetaldehyde. In 2016 the global consumption of acetaldehyde was predicted to grow 3 % annually [7]. The global market for acetaldehyde is projected to be 1.6 million tons by 2024 which is affected by the growing use of acetaldehyde as a platform chemical in production of various organic compounds such as acetic acid and acetic anhydride, based on a report by global industry analysts [8].

It is noteworthy that acetaldehyde has mainly been manufactured via oxidation of ethylene as well as hydration of acetylene [9]. Hydration of acetylene to acetaldehyde is a cost effective process but it is not favorable because of using a catalyst containing mercury which is a toxic material. The acetylene itself was derived from calcium carbide which is an environmentally unfriendly material. In the late 1950s production of acetaldehyde from acetylene was replaced in favor of an olefin-based process, the Wacker oxidation [10]. The reason was due to the more energy efficiency and thus cheaper production of olefins as well as easier handling compared to acetylene. Since then, ethylene has been the main source of acetaldehyde production [11, 12]. On the other hand, while partial oxidation of ethanol is claimed to be economically less feasible, it

has no harmful effect on environment which makes it a quite attractive topic of research. In industry this process is typically conducted on a silver catalyst at 450–550°C with the acetaldehyde selectivity of 85–95 % [12].

One of the other products which can be formed during the ethanol oxidation is acetic acid from oxidation of acetaldehyde, although the main industrial process of acetic acid production is via methanol carbonylation nowadays. Acetaldehyde oxidation is industrially operated at 50–70°C in oxidation towers made of stainless steel (bubble columns) while methanol carbonylation (with CO) is conducted at 150–200°C under pressures of up to 30 bar [12]. Acetic acid can be used as a chemical reagent for production of vinyl acetate monomer (VAM) and acetic anhydride.

Moreover, ethanol is also an essential feedstock for ethyl acetate production via esterification of acetic acid using an acidic catalyst. However, the production route depends on the availability and cost of the feedstock, for instance, in countries where ethanol is expensive or not present in sufficient quantities, usually ethyl acetate is manufactured via Tishchenko reaction with acetaldehyde. The ethyl acetate market has had a remarkable growth during the last decade [13] which is predicted to continue at least till 2024 [14]. Ethyl acetate is an important substance being widely used in paint industry, as an extraction solvent and manufacture of pharmaceuticals such as antibiotics.

A general reaction scheme of oxidation of ethanol is demonstrated in Scheme 1. As it can be seen, depending on the catalyst and the reaction conditions, besides ethanol oxidation other reactions may take place such as oxidation of acetaldehyde, esterification of acetic acid, dehydration of ethanol or even total oxidation of ethanol. Therefore, in order to optimize the selectivity towards the desired products, a broad-range catalyst screening as well as precise kinetic studies are of great importance.

- 1)  $2CH_3CH_2OH + O_2 \rightarrow 2CH_3CHO + 2H_2O$
- 2)  $2CH_3CHO + O_2 \rightarrow 2CH_3COOH$
- 3)  $CH_3CH_2OH + CH_3COOH \leftrightarrow CH_3COOCH_2CH_3 + H_2O$
- 4)  $2CH_3CH_2OH \leftrightarrow CH_3CH_2OCH_2CH_3 + H_2O$
- 5)  $CH_3CH_2OH + 3O_2 \rightarrow 2CO_2 + 3H_2O$
- 6)  $CH_3CH_2OH \leftrightarrow C_2H_4 + H_2O$

*Scheme 1. General reaction paths for oxidation of ethanol using molecular oxygen*

## 1.2. Catalysis by gold

Most of the chemical transformations carried out in industrial scale are based on the use of heterogeneous catalysts, in which a metal (e.g., Cu, Ni, Co, Mo, Pt, Pd, Re, Rh, Ru) is dispersed on a highly porous support (e.g. silica, alumina, active carbon, zeolites). In catalysis, gold was first time shown to be active in the oxidation of methanol to formaldehyde as early as in 1913 by Fokin who used asbestos as a catalyst support [15, 16]; Au and Ag powders were more active in the reaction than supported Pt. Already Sabatier referred to this work in 1913 in his book: “La Catalyse en Chimie Organique” [17] which later in 1922 was translated to English [18]. These findings were somewhat forgotten until a breakthrough was triggered by Hutchings [19] and Haruta et al. [20] in 1980s. They independently demonstrated that small gold nanoparticles are highly active in acetylene hydrogenation and low temperature CO oxidation, respectively.

It turned out that gold as nanoparticles smaller than 5 nm deposited on oxides, polymers and carbon makes unique active catalysts especially for oxidation reactions, therefore, catalysis by gold has rapidly become a hot topic in chemistry after the prosperous development of nanoscience [21–23]. Gold nanoparticles as catalysts have numerous applications in chemical transformations, for instance, in carbon monoxide oxidation [24, 25], catalytic combustion of hydrocarbons [26], hydrochlorination of acetylene [27], direct synthesis of hydrogen peroxide from hydrogen and oxygen [28], oxidation of glucose to gluconic acid [29], oxidative removal of mercury [30], ozone decomposition [31], reduction of NO<sub>x</sub> with propene [32], selective oxidation, e.g. propylene to propylene oxide [33], selective hydrogenation, e.g. of alkynes and dienes to mono-olefins [34, 35], vinyl acetate synthesis from ethane, acetic acid and oxygen [36], water gas shift [37], and biomass conversion [38]. In particular, considerable experimental and computational research efforts have been taken to improve the aerobic oxidation of alcohols with environmentally friendly oxidizers such as molecular oxygen in the presence of heterogeneous gold catalysts both in the gas and liquid phase [39–48].

Nanonsized gold dispersed on porous support materials is an effective catalyst in the oxidation of hydroxyl groups (–OH) to carbonyl (C=O) or carboxyl groups (COOH), which are important products in numerous chemical syntheses. Different reagents like primary linear (1-butanol, 1-octanol) [49] or aromatic (benzylic alcohol) [50] alcohols and polyols (glycerol, glycol, glucose) [51] have been under research.

However, utilizing gold nanoparticles as the catalyst sets new challenges while working with structure sensitive reactions to maximize the reaction rate, since tailoring of gold nanoparticles size as well as narrowing the size distribution is a very demanding task. Usually gold nanoparticles are distributed on a support e.g., oxides or zeolites to increase the surface area of the catalyst. Hence, the properties of the support material is very important in tuning the size of the gold nanoparticles as well as the metal loading, especially on some zeolite materials which have a negatively charged surface on which there would be very low electrostatic interaction with the gold ions. It is noteworthy that other effects such as interactions with the support [52] and charge transfer [53] are also decisive but to a lesser extent.

### 1.3. Microreactor technology

All chemical processes need an efficient equipment, efficient reactor and separation technology to become technically and economically feasible. Application of microreactors is associated with process intensification meaning a reduction in equipment size by several orders of magnitude, thus causing a remarkable decrease in capital and energy costs and a positive environmental impact. Development of microscale production technology is a hot topic in current chemistry and chemical engineering.

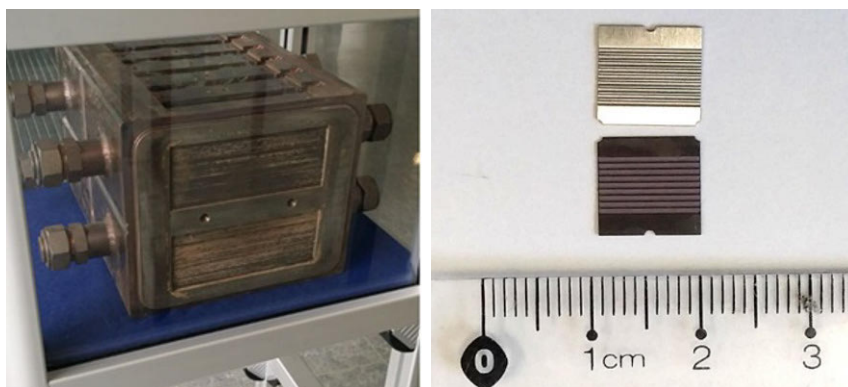


*Figure 1. One of the first microreactors constructed at Institute für Mikroverfahrenstechnik, Karlsruhe Institute of Technology, containing hundreds of microplatelets (left). The microreactor used in this work (right)*

Microreactors are efficient tools in catalyst screening and kinetic investigations because only small amounts of chemicals and materials are needed and experiments can be performed very rapidly. Moreover, the diffusion distances are short which consequently suppresses the internal and external diffusion limitations. The general slogans to promote microscale reactor technology propose high surface area-to-volume ratio

(up to 50,000 m<sup>2</sup>/m<sup>3</sup> compared to maximum 1000 m<sup>2</sup>/m<sup>3</sup> in conventional reactors [54] because of the thin catalyst layers, good heat transfer properties (~25 W/m<sup>2</sup>) [54], straightforward scale-up, because conventional scale-up can in principle be replaced by number-up [55]: a sufficient production volume is obtained by coupling microscale units in parallel. One of the big advantages of microreaction technology is inherent safety [56] without raising environmental issues; by using microreactors less amount of industrial wastes are produced. Microreactors can be used for on-line production of hazardous chemicals [57], so that the risks in road and rail transport are avoided. The extreme limits of chemistry can be approached by use of microreactors, and operation close to or even within explosion limits is proposed [58]. Many efforts have recently been made to manufacture and utilize microreactors in order to achieve a better control of the reaction parameters.

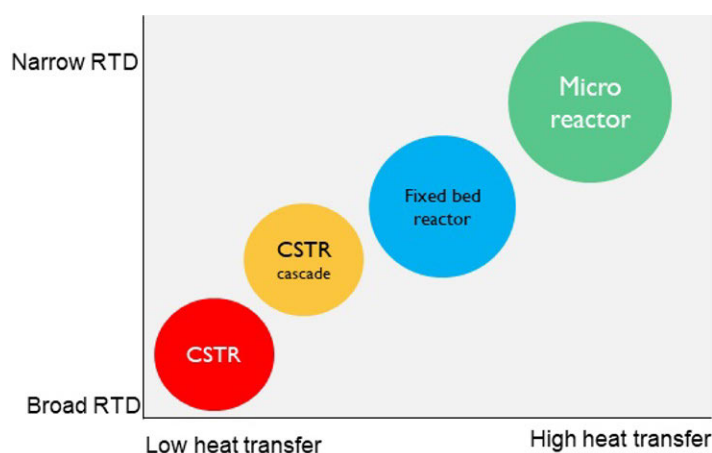


*Figure 2. Comparison of residence time distribution and heat transfer characteristics in microreactor and some conventional reactors*

One of the most demanding tasks in using microreactors hindering their widespread application is attachment of the catalytically active phase on the walls of the very low volume microchannels (down to ~0.4 µl) because the catalytic layer thickness strongly influences heat and mass transfer and consequently, the catalytic behavior of the microreactor. Important considerations to be taken into account when dealing with microreactor coating are the catalyst layer uniformity, stability and thickness which should be optimized simultaneously. Therefore, selecting the most suitable coating method and developing it for a certain catalyst is very crucial and of great importance.

#### **1.4. Research objectives**

The goal of the present work was to develop microreactor technology to be applied in selective oxidation of ethanol using gold nanoparticles as catalysts and to study the reaction kinetics and mechanism in a conventional fixed bed and a microreactor. The research hypotheses were: 1) the product selectivity could be improved by using microreactors because very well controlled conditions are guaranteed (excellent heat and mass transfer: local temperature and concentration gradients are minimized) and 2) the overall reaction rates could be considerably enhanced (compared to conventional packed bed reactors) because very thin catalyst layers are used, which minimizes the internal diffusion resistance in the catalyst layer.

The research subprojects consisted of catalyst preparation and characterization, catalyst screening, development of a coating method for the reactor elements, analysis of the reaction mechanism at the density functional theory level, as well as kinetic modelling.

## **2. Experimental**

## 2. Experimental

### 2.1. Chemicals

H-Y-12, H-Y-80, H-Beta-25 zeolites (Zeolyst International),  $\gamma$ - $\text{Al}_2\text{O}_3$  (UOP Versal VGL-25) and  $\text{SiO}_2$  (Merck & Co., Inc.) were used in this work as the catalyst supports which were modified with gold using hydrogen tetrachloroaurate(III) hydrate (99.9 %-Au) (49 % Au) (chloroauric acid) (Alfa Aesar and ABCR GmbH) as a precursor. Ammonium hydroxide  $\text{NH}_4\text{OH}$  solution 32 % (Merck) was used as a precipitation agent for pH adjustment. Ink preparation for microreactor coating via printing was performed using 20 wt% aqueous colloidal nano-suspension of alumina having a particle size ( $d_{90}$ ) of 100 nm (Alfa Aesar GmbH & Co KG) modified with ethylene glycol (Merck GmbH). Ethanol (ETAX Aa) for the oxidation reaction was obtained from ALTIA Industrial Oyj.

### 2.2. Catalyst preparation

H-Y-12 (12 =  $\text{SiO}_2/\text{Al}_2\text{O}_3$  molar ratio), H-Y-80, H-Beta-25 zeolites,  $\gamma$ - $\text{Al}_2\text{O}_3$  and  $\text{SiO}_2$  were modified with gold via deposition-precipitation method using hydrogen tetrachloroaurate (III) hydrate as a precursor. The  $\text{NH}_4^+$  form of zeolites was transformed to the proton form by calcination at  $400^\circ\text{C}$  for 4 h. The gold precursor was diluted to 1.15–2 g/l. The pH of the mixture of the support material and the gold solution was adjusted by adding ammonium hydroxide  $\text{NH}_4\text{OH}$  solution while the mixture was vigorously stirred. It should be noted that some of the  $\gamma$ - $\text{Al}_2\text{O}_3$ /gold precursor mixture solutions were heated up to  $70^\circ\text{C}$  before the pH adjustment. After reaching the intended value of pH (6.5–10.5), the solution was aged for 3 h. The catalysts were filtered and washed with 3 l distilled water to remove the chlorine species followed by drying at  $100^\circ\text{C}$  for few hours and eventually calcining at  $300^\circ\text{C}$ .

### 2.3. Catalyst slurry preparation for microplatelet coating (the first method)

The coating of the microplatelets was carried out via the suspension method in which the slurry of the ready to use catalyst is directly deposited into the microplatelet channels. 5 wt% (solid content) catalyst slurry was prepared by adding Au/ $\gamma$ - $\text{Al}_2\text{O}_3$  catalyst to distilled water without using any additives. The slurry was stirred at 300 rpm using a magnetic stirrer for 4 h at  $40^\circ\text{C}$  and afterwards at ambient temperature up to four days.

## **2.4. Microplatelet coating via the slurry method**

The microplatelets were calcined in air at 750°C for 3 h with the heating rate of 3°C/min prior to coating. This pretreatment usually leads to the formation of an oxide layer on the stainless steel plates acting as anchoring sites for a better adhesion of the catalyst on the channel walls. In order to deposit the catalyst slurry into the channels, a 0.5–10 µl Finnpiette was used. 3.5 µl slurry was deposited into the channels of each microplatelet and the excess slurry was wiped off. The plates were dried both at 6°C and room temperature. Finally, the plates were calcined at 250–300°C. Calcination at higher temperatures was avoided due to probability of the gold nanoparticles sintering. The mass of the catalyst deposited into the channels was measured by weighing the microplatelets before and after the catalyst coating.

## **2.5. Catalyst ink preparation for microplatelets coating (the second method)**

The ink was prepared using colloidal nano-suspension alumina which exists at pH 4 as pseudo-Boehmite (AlO(OH)). The colloidal suspension was further modified with 25–50 wt% ethylene glycol to adjust the alumina particle concentration.

## **2.6. Microplatelet coating via inkjet printing**

The microplatelets were calcined at 750°C prior to coating following the same calcination program as for the suspension method. The size of the ink droplets was tuned with the proper pulse and voltage of the printer being about 90 µm in diameter. Since the size of the droplets were considerably smaller than the microchannel dimensions, for instance for formation of a 1 µm catalyst layer thickness, the printing was done three times through the channel. The ink containing of alumina, ethylene glycol and water was printed into the channel followed by calcination at 550°C.

Afterwards, the gold deposition on the printed alumina support was performed via deposition-precipitation method. First, the pH of the 1.15 g/l gold solution (15 ml) was 2.6 which was increased to 8.9 by ammonia 32 % and afterwards, the microplates were immersed into the solution. The solution was stirred for 12.5 h using a magnetic stirrer at 450 rpm. The final pH was 8.3. Finally, the microplatelets were dried at 100°C for 2.5 h followed by calcination for 3 h at 300°C.

## **2.7. Catalyst and coated microplatelet characterization**

The characterizations of the catalysts, catalyst slurry and the microplatelets were carried out using nitrogen adsorption, X-ray Diffraction (XRD), Fourier Transform Infrared Spectroscopy (FTIR), Scanning Electron Microscopy (SEM), confocal white light microscopy, laser diffraction, viscosity measurements, Transmission Electron Microscopy (TEM), Energy-disperse X-ray (EDX), Inductively Coupled Plasma-Optical Emission Spectroscopy (ICP-OES) and X-ray Photoelectron Spectroscopy (XPS).

### **2.7.1. Nitrogen adsorption**

The specific surface areas and the micro/mesopore volumes of the catalysts and catalyst slurries were determined by nitrogen adsorption (Sorptometer 1900, Carlo Erba Instruments). Prior to the analysis, the catalysts were outgassed for 3 h at 150°C to remove air and moisture from the pores. BET and Dubinin equations were used for surface area calculations of meso and microporous materials, respectively. The pore volumes were calculated using the Dollimore-Heal method.

### **2.7.2. X-ray diffraction (XRD)**

The crystallinity structure of the unsupported and Au modified catalysts as well as the catalyst slurry was studied using XRD (PANalytical Empyrean X-ray powder diffractometer).

### **2.7.3. Fourier transform infrared spectroscopy (FTIR)**

Acidity of the unsupported, Au modified catalysts and the catalyst slurry was measured using FTIR (ATI Mattson). The Brønsted and Lewis acid sites were determined qualitatively and quantitatively using pyridine ( $\geq 99.5\%$ ) as the probe molecule. The samples were pelletized to a thin disc and pretreated at 450°C for 1 h prior to the measurement. Thereafter, the temperature was decreased to 100°C and pyridine was adsorbed on the catalysts for 30 min and desorbed subsequently by evacuation at 250, 350 and 450°C, respectively. Desorption of pyridine at 250–350°C corresponds to weak, medium and strong sites, 350–450°C is related to medium and strong sites while the desorption at 450°C reflects the strong sites only [59]. The intensities of spectral bands, 1545 and 1450  $\text{cm}^{-1}$ , correspond to Brønsted and Lewis acid sites, respectively. The amount of the acid sites were evaluated with the aid of molar extinction coefficients reported by Emeis [60].

#### **2.7.4. Scanning electron microscopy (SEM)**

The morphology of the catalyst powders, catalysts particle size as well as homogeneity, thickness and the catalyst layer stability inside the microchannels were studied using a scanning electron microscope (Zeiss Leo Gemini 1530). Cross-section images of the microplatelets were taken by Jeol JXA8530F field emission electron probe microanalyser.

#### **2.7.5. Laser diffraction**

The particle size measurements of the catalysts and the dried aged catalyst slurry were carried out using a Malvern Mastersizer 3000 laser diffractometer. The measured samples were dispersed in distilled water using a Hydro EV wet sample dispersion unit.

#### **2.7.6. Surface charge measurements**

The zeta potentials of the catalyst powder and catalyst slurry were measured at room temperature with Malvern Zetasizer Nano ZS. The measurements were performed by dissolving 20 mg of the catalyst in 10 ml distilled water followed by ultrasonication of the suspension. Prior to the measurements, the catalysts were dried at 100 °C for 24 h. The zeta potential was measured as a function of pH in the range of 2–11 by titrating with HCl 0.2 M, NaOH 0.02 and NaOH 0.2 M.

#### **2.7.7. Viscosity measurements**

The rheological measurements of the catalyst slurry were performed using Physica MCR 300 Rheometer (Anton Paar) with a concentric cylinder CC27. Ramp viscosity at a shear rate increasing from 0.01 to 1000 rpm and back was measured. The samples were first sheared at 0.01rpm, and then the shear was increased to 1000 rpm and reduced again to 0.01 rpm. All the measurements were conducted at room temperature.

#### **2.7.8. Transmission electron microscopy (TEM)**

Transmission electron microscopy was used to measure the Au average particle size and subsequently Au size distribution as well as for Au dispersion calculations. Electron microphotographs of the fresh and spent catalysts were obtained with a JEM 1400 Plus Transmission Electron Microscope. Average particle sizes and

particle size distributions were obtained by counting 300–800 of Au particles for each catalyst.

### **2.7.9. Energy dispersive X-ray analysis (EDX)**

The gold content of the catalyst powders, aged catalyst slurry and the spent catalyst, as well as the elemental analysis of the stainless steel microplatelets before and after the thermal treatment was evaluated by EDX (LEO Gemini 1530 with a Thermo Scientific UltraDry Silicon Drift Detector).

### **2.7.10. Inductively Coupled Plasma-Optical Emission Spectroscopy (ICP-OES)**

ICP-OES analysis of an Au/Al<sub>2</sub>O<sub>3</sub> catalyst was performed for comparison with the value obtained using EDX. For ICP-OES, argon plasma was used to excite optical emission of the elements to be analyzed.

### **2.7.11. X-ray photoelectron spectroscopy (XPS)**

XPS was conducted to reveal the oxidation state of gold on the fresh and spent catalysts. The spectra were collected with a Kratos Axis Ultra DLD electron spectrometer using monochromatized Al-K<sub>α</sub> source operated at 120 W.

## 2.8. Catalytic experiments

### 2.8.1. Reactors system

Both fixed bed and microreactor were used in this work. The catalytic tests within the packed bed reactor (Figure 3) were conducted by using catalysts (average particle size, 32–63  $\mu\text{m}$  and the catalyst mass, 160 mg). The reactor was a quartz tubular fixed bed with an inner diameter of 9 mm. The temperature inside the reactor was controlled by a PID controller (CalControls 9500 P) with a k-type thermocouple placed in the catalyst bed (with  $\pm 1$   $^{\circ}\text{C}$  accuracy).

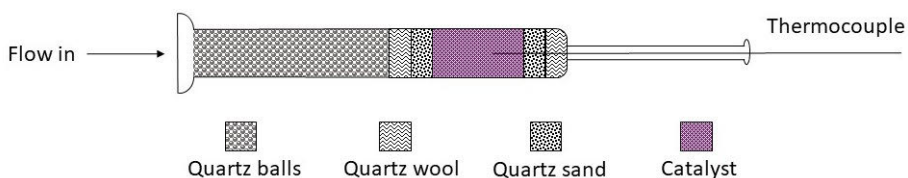


Figure 3. Schematic presentation of the fixed bed tubular reactor

The microreactor was purchased from Institute für Mikrotechnik Mainz GmbH (IMM) containing 10 etched stainless steel microplatelets (size 9.5×9.5 mm). Each microplatelet had 9 microchannels as shown in Figure 4. The microreactor consisted of 10 stack mixing plates (size 7.4×7.4 mm) having nine curved channels with different radii in order to keep the volume in the channels constant. The gases are mixed in the diffusion chamber before entering the catalyst zone. Two cylindrical cartridges were used to heat up the microreactor. Temperature was controlled by a PID controller (CalControls 9500P) with a thermocouple in the housing of the microreactor (with  $\pm 1^{\circ}\text{C}$  accuracy). Additional details about the microreactor used in this work are presented in Table 1.

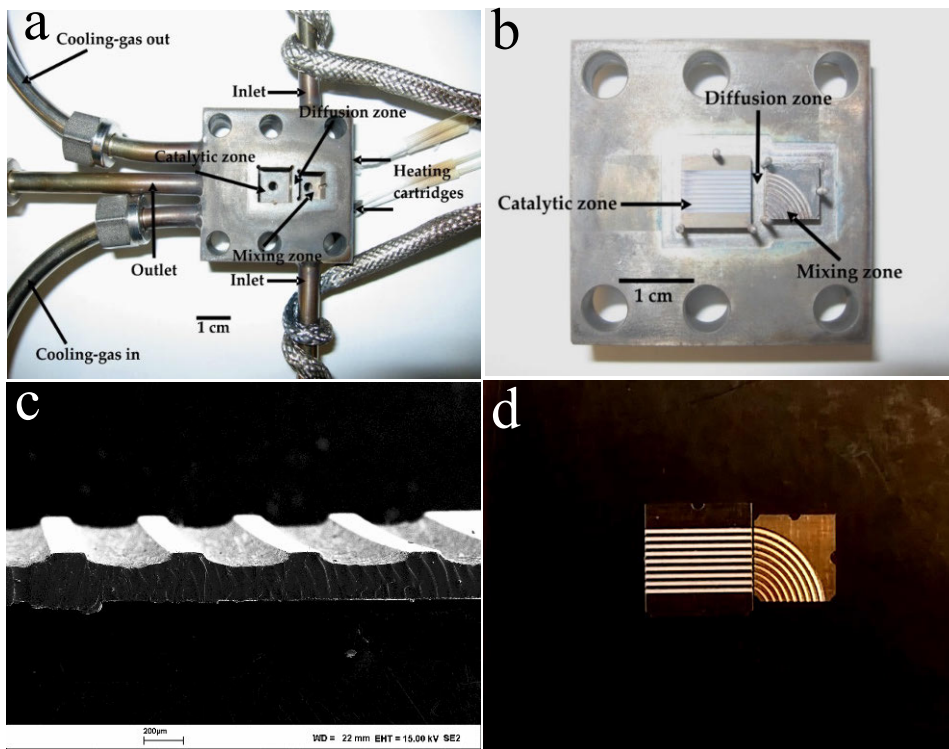


Figure 4. a) Microreactor body, b) mixing, diffusion and catalytic zone, c) cross section of a microplatelet and d) a mixing and a micro plate

Table 1. Technical data of the microreactor used in this work

| Property  | Value  |
|---|--|
| Model   | GPMR-MIX   |
| Size (L x B x H) (mm)                                       | 45 × 45 × 32   |
| Connectors (inlet/outlet)                                   | 1/4"   |
| Standard material   | Inconell 600 (2.4816) for housing and top plate; 1.4571 for mixing and catalyst plates |
| Number of mixing plates                                     | 10   |
| size of mixing plates (mm)                                  | 7.5 × 7.5  |
| Channel geometry of mixing plates (width × depth; μm)       | 180–490 × ~100   |
| Number of catalyst plates                                   | 10   |
| Size of catalyst plate (mm)                                 | 9.5 × 9.5  |
| Channel geometry of the catalyst plates (width × depth; μm) | 460 × 90   |
| Number of channels per plate                                | 9  |

The catalytic tests were conducted at atmospheric pressure. A schematic view of the experimental setup is presented in Figure 5. The gas mixture contained ethanol, oxygen and helium. Liquid ethanol was fed at room temperature by a HPLC pump (Shimadzu, LC-20AD) to a preheater. The oxygen and helium flows were controlled by Bronkhorst (HIGH-TECH) mass flow controllers. The gas mixture was in excess of oxygen and it was heated at 100°C prior to the reactor inlet. The reaction was conducted in the temperature range of 100–250°C. The temperature was varied stepwise with 25°C intervals. The heating rate was 3°C/min and the dwelling time at each temperature was 2.5 h. The gas mixture at the reactor outlet was heated at 130°C to prevent condensation and was analyzed by an on-line gas chromatograph (Agilent Technologies, 7820A) equipped with both thermal conductivity (TCD) and flame ionization (FID) detectors. The capillary column (HP-PLOT/Q) dimensions were 30 m length, 0.53 mm diameter and 40 µm film of the immobile phase.

In order to reach the steady state, prior to each experiment, the reactive gas mixture was switched on for 30 min. Some of the reactions were retested by using a fresh sample from the same catalyst batch and gave reproducibility within  $\pm 5\%$ .

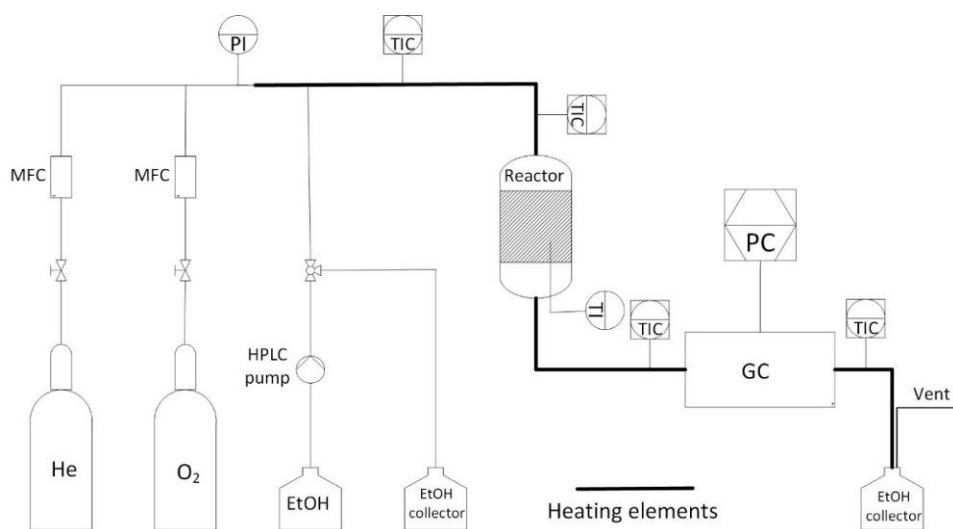


Figure 5. Process flow diagram of the experimental setup where MFC: Mass Flow Controller, HPLC: High Performance Liquid Chromatography, PI: Pressure Indicator, TI: Temperature Indicator, TIC: Temperature Indicator and Controller and PC: Personal Computer

### 2.8.2. Basic calculations

The ethanol conversion ( $X_{EtOH}$ ), the yield ( $Y$ ) and the product selectivity ( $S$ ) were calculated according to the following equations:

$$X_{EtOH} = \frac{C_{0,EtOH} - C_{EtOH}}{C_{0,EtOH}} \quad (1)$$

$$Y_i = \frac{v \cdot C_i}{C_{0,EtOH}} \quad (2)$$

$$S_i = \frac{Y_i}{X_{EtOH}} \quad (3)$$

where  $C_{0,EtOH}$  and  $C_{EtOH}$  are the concentration of ethanol at the reactor inlet and outlet, respectively, while  $C_i$  corresponds to the concentration of the product  $i$ . The constant  $v$  is equal to 1 for acetaldehyde and acetic acid, 2 for ethyl acetate, diethyl ether and ethylene, and 0.5 for carbon dioxide.

The turnover frequency (TOF) was calculated based on the following equation:

$$TOF = \frac{X_{EtOH} \cdot \dot{n}_{EtOH,in}}{n_{Au,tot} \cdot D_{Au}} \quad (4)$$

where  $X_{EtOH}$  is the ethanol conversion,  $\dot{n}_{EtOH,in}$  is the molar flow of ethanol at reactor inlet,  $n_{Au,tot}$  is the total moles of Au and  $D_{Au}$  is the Au dispersion calculated based on the following equation [61]:

$$D_{Au} = \frac{6M_{Au}}{a_{Au}\rho N_A d_{vs}} \quad (5)$$

where  $M_{Au}$  is the molar mass of gold ( $0.197 \text{ kg mol}^{-1}$ ),  $a_{Au}$  is the average effective area of an Au atom on the support surface ( $8.7 \times 10^{-20} \text{ m}^2$ ),  $\rho$  is the density of gold ( $1.932 \times 10^4 \text{ kg m}^{-3}$ ),  $N_A$  is the Avogadro number and  $d_{vs}$  is the volume-surface diameter calculated according to the equation below [61], where  $d_i$  is the measured diameter of a gold particle by TEM:

$$d_{vs} = \frac{\sum d_i^3}{\sum d_i^2} \quad (6)$$

## **3. Results and discussion**

### 3. Results and discussion

#### 3.1. Catalyst preparation, characterization and screening

A series of zeolite and oxide supported gold catalysts were synthesised via deposition-precipitation method for ethanol oxidation and the catalysts were characterized thoroughly (Table 2).

Table 2. Characterization data of the catalysts

| Catalyst                     | Nominal Au loading (wt%) | Final Au loading (wt%) | Loading efficiency (%) | Au average size (nm) | Au dispersion (%) | Specific surface area ( $\text{m}^2 \text{g}^{-1}$ ) | Pore volume ( $\text{cm}^3 \text{g}^{-1}$ ) | Solution pH |
|------------------------------|--------------------------|------------------------|------------------------|----------------------|-------------------|--|---|-------------|
| H-Y-12 [62]                  | –                        | –                      | –                      | –                    | –                 | 884  | –   | –           |
| Au/H-Y-12                    | 3.2                      | 1                      | 31                     | 16.6                 | 3.3               | 640  | 0.23  | 8.5         |
| H-Y-80                       | –                        | –                      | –                      | –                    | –                 | 1575   | 0.56  | –           |
| Au/H-Y-80                    | 3.2                      | 1.37                   | 43                     | 6.3                  | 14.4              | 797  | 0.28  | 10.5        |
| Au/H-Y-80                    | 2.5                      | 1                      | 40                     | 7.6                  | 14.2              | 645  | 0.23  | 9           |
| Au/H-Y-80                    | –                        | 2.4                    | –                      | 9.3                  | 10.9              | 501  | 0.17  | 10.5        |
| H-Beta-25                    | –                        | –                      | –                      | –                    | –                 | 970  | 0.34  | –           |
| Au/H-Beta-25                 | 2.2                      | 2.14                   | >90                    | 11.2                 | 1.1               | 652  | 0.23  | 10.5        |
| $\text{Al}_2\text{O}_3$ [63] | –                        | –                      | –                      | –                    | –                 | 303  | 1.3   | –           |
| Au/ $\text{Al}_2\text{O}_3$  | 2                        | 1.59                   | 80                     | 2.1                  | 46.2              | 266  | 0.97  | 10.2        |
| Au/ $\text{Al}_2\text{O}_3$  | 2                        | 1.64                   | 82                     | 3.7                  | 26.9              | 298  | 1   | 6.6         |
| $\text{SiO}_2$ [64]          | –                        | –                      | –                      | –                    | –                 | 496  | 0.92  | –           |
| Au/ $\text{SiO}_2$           | 2.1                      | 1                      | 47                     | 4.2                  | 18.3              | 492  | 0.76  | 6.6         |

##### 3.1.1. Effect of Au deposition on the acidity of the catalysts

Since the acidity of a catalyst plays a crucial role in its selectivity in the oxidation, therefore, it is important to measure the changes of the acidity before and after the metal modification of the catalyst support (Table 3).

The increase in the Brønsted acid sites (BAS) of H-Y-12 after deposition of Au can be due to the compensation of protons on the surface by nonacidic cations, while the increase in the Lewis acid sites (LAS)

can be attributed to the interactions of pyridine with gold metal particles which are electron acceptors and generally act as Lewis acids [65, 66]. Unlike the concentration of Lewis sites, the Brønsted sites of H-Y-80 catalysts decreased after the Au modification [67]. However, all Au/H-Y-80 catalysts had approximately the same total acid concentrations; mainly Lewis sites, which implies that an Au loading in the range of 1–2.4 wt% did not affect the total acidity of this support. The decrease in BAS of this catalyst might be due to proton migration from the bridging OH groups to Au. The highest BAS and LAS were determined for H-Beta-25. After deposition of Au on this support, the concentration of the acid sites, especially the Lewis ones dropped considerably which could be either due to interactions of some amounts of the very small metal clusters with the support inside the pores or leaching of Al in the support structure during the catalyst preparation. The structural analysis by XRD did not show any significant amorphocity in the structure of H-Beta-25 after the Au deposition; however, Al might move from the framework to the extra framework. A similar reduction in LAS on H-Beta-25 was reported after deposition of Pt on the surface which was correlated to the interactions of small Pt nanoparticles with the Lewis acid sites, although the average particles size (3.4 nm) was larger than the pore size of the support [68]. Al<sub>2</sub>O<sub>3</sub> contained only Lewis acid sites, mainly weak ones, while the least acidic catalyst was SiO<sub>2</sub> as expected. Deposition of gold did not change the acidity of Al<sub>2</sub>O<sub>3</sub>.

*Table 3. Acidity measurements of the unsupported and Au supported catalysts*

| Catalyst                                    | Brønsted acid sites (μmol/g) |       |       | Lewis acid sites (μmol/g) |       |       |
|---|------------------------------|-------|-------|---------------------------|-------|-------|
|   | 250°C                        | 350°C | 450°C | 250°C                     | 350°C | 450°C |
| H-Y-12                                      | 253                          | 211   | 145   | 36                        | 6     | 2     |
| Au/H-Y-12                                   | 272                          | 233   | 147   | 46                        | 13    | 6     |
| H-Y-80                                      | 16                           | 8     | 3     | 18                        | 8     | 1.6   |
| Au/H-Y-80 (6.3 nm)                          | 6                            | 2     | 0.8   | 32                        | 14    | 2     |
| Au/H-Y-80 (7.6 nm)                          | 8                            | 2     | 1     | 30                        | 16    | 2     |
| Au/H-Y-80 (9.3 nm)                          | 6                            | 2     | 0.1   | 34                        | 15    | 1     |
| H-Beta-25                                   | 269                          | 207   | 120   | 162                       | 125   | 113   |
| Au/H-Beta-25                                | 233                          | 202   | 141   | 143                       | 82    | 33    |
| Al <sub>2</sub> O <sub>3</sub>              | 0                            | 0     | 0     | 56                        | 17    | 8     |
| Au/ Al <sub>2</sub> O <sub>3</sub> (2.1 nm) | —                            | —     | —     | 60                        | —     | —     |
| SiO <sub>2</sub>                            | 0                            | 0     | 0     | 6                         | 0     | 0     |

### 3.1.2. Effect of solution pH on Au particle size and size distribution

The pH of the solution as a parameter controlling the surface charge governs the relative rates of nucleation and metal growth. Therefore, it is crucially important to see how the surface charge of the support changes during the catalyst synthesis. In the current work, the surface charge (zeta potential) of H-Y-80 at different steps of the catalyst synthesis namely before and after adding the gold precursor ( $\text{HAuCl}_4 \cdot 3\text{H}_2\text{O}$ ), the precipitating agent ( $\text{NH}_4\text{OH}$ ) and the calcination was investigated.

As illustrated by Figure 6-a, the variations in surface charge are more pronounced above pH 4. After adding  $\text{NH}_4\text{OH}$  to the solution, the zeta potential slightly shifted to less negative values, which can be due to neutralization of the surface charges by  $\text{NH}_4^+$  ions. However, the surface did not become positively charged which can be attributed to the dissociation of hydroxyl groups on the surface [69].

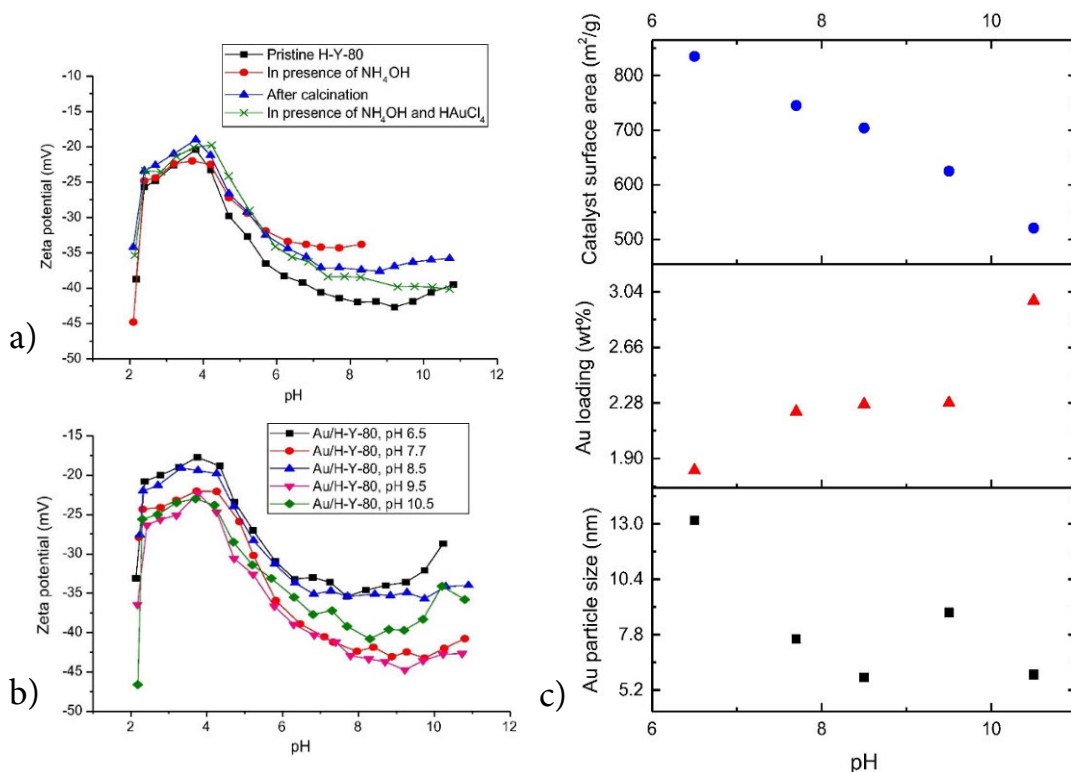


Figure 6. a) Effect of pH on H-Y-80 surface charge at different steps during catalyst preparation, b) effect of pH on H-Y-80 surface charge in presence of  $\text{HAuCl}_4$ , and c) effect of pH on Au average particle size and loading with the final specific surface area of the catalysts after Au modification

In the subsequent calcination step, the surface OH groups were removed to some extent, but led to the surface charge still higher than the pristine material. Thereafter, when  $\text{HAuCl}_4$  was added to the solution, from pH 7.5 onwards, the zeta potential values only mildly declined and distanced from the surface charge of the sample prepared in the presence of only  $\text{NH}_4\text{OH}$  which was calcined later. As a conclusion, the  $\text{NH}_4\text{OH}$  addition demonstrated a relatively stronger influence on the surface charge than calcination and the gold precursor. Therefore, in order to reveal the effect of the surface charge on the average gold particle size, size distribution and loading, five Au/H-Y-80 catalysts at different pH (6.5–10.5) were prepared and their zeta potentials were measured (Figure 6-b). As previously demonstrated, because the H-Y-80 surface is always negatively charged, it is difficult to electrostatically deposit the  $[\text{AuCl}_n(\text{OH})_{4-n}]^-$  anion species. On the other hand, a neutral surface causes agglomeration of the particles [70]. Thus, positive surface charges should be generated during catalyst preparation. As a result, none of the pH values resulted in positively charged surfaces. However, a pH range within negative values was found when negative charges on the surface led to a formation of smaller Au clusters. On the contrary, crossing over the minimum level of this range toward the neutral surface instigated Au particles to agglomerate. On the whole, raising the pH from 7.7 to 10.5 (from the lowest to highest negative surface charges) was accompanied with an increase in the gold particle size from 5.8 to 8.8 nm (Figure 6-c). By moving out of this pH range to pH 6.5, the surface became less negatively charged and larger Au clusters (13.2 nm) were formed. The reason why at pH values exceeding 6.5 smaller Au clusters were formed can be attributed either to the diameter of the Au complexes which vary with pH, or to the attractive and repulsive forces between the charged Au complexes. As the pH is raised, chloride ions are replaced by hydroxyl ions which have smaller diameter forming smaller Au complexes which are more prone to be placed inside the support pores [71]. Furthermore, at higher pH values more negative charges on the Au complexes could limit the metal growth by repulsion due to the double layer of the charged metal nanoparticles while induced electric dipole moments can lead to agglomeration of metal clusters [72].

A similar pattern was observed taking into account the Au particle size distribution: the narrowest particle size distribution (2–14 nm) formed at pH 8.5 corresponded to the lowest negative surface charges, while the catalyst prepared at pH 9.5 having the highest amount of negative surface charges, demonstrated a broad range 2–30 nm of Au clusters precipitated on the carrier surface. In the pH range of 7.7–10.5, less negatively charged surfaces resulted in narrower Au particle size distribution. Departure from this pH range to pH 6.5 led, however, to a broader particle size distribution (2–40 nm).

### 3.1.3. Effect of pH of the solution on Au loading and catalyst surface area

Based on a gold precursor hydrolysis mechanism proposed by Nechayev and Zvonareva [73] which explains pH dependency, at pH exceeding 6,  $\text{AuCl}(\text{OH})_3^-$  species are prevalent, while above pH 10,  $\text{Au}(\text{OH})_4^-$  are the dominant species. Thus, the electrostatic adsorption on a negatively charged surface cannot simply occur. A reason for precipitation of anion Au complexes on the negatively charged surface might be due to the existence of  $\text{Au}(\text{OH})_3 \cdot \text{H}_2\text{O}$  neutral species which are formed at lower pH in the solution and are in equilibrium with the anions; they interact with the surface and act as anchoring sites to precipitate the anions [71]. In this work, raising the pH from 6.5 onwards, led to a higher Au loading efficiency (1.82 to 2.98 wt%, Figure 6-c). It can be concluded that raising the pH caused the precipitation of more gold on the H-Y-80 surface. Figure 6-c depicts an increase in the loading from 1.82 wt% at pH 6.5 to 2.98 wt% at pH 10.5 which was accompanied by a decrease in the surface area from 835 to 521  $\text{m}^2/\text{g}$ .

### 3.1.4. Catalysts activity

Ethanol oxidation was carried out using the neat supports as well as the corresponding Au modified catalysts. As Figure 7 illustrates, all catalysts exhibited very low activities at 100°C; the highest conversion at 100°C was 3.4 % for Au/ $\text{Al}_2\text{O}_3$  with 2.1 nm Au, while complete conversion was achieved on Au/H-Y-80 with 6.3 nm Au at 225 °C.

The H-Y-80 catalyst did not show any reactivity even at the highest temperature illustrating a necessity of having Au nanoparticles as the active phase on this support to oxidize ethanol. Both H-Y-12 and H-Beta-25 catalysts showed almost similar conversions as their Au modified forms implying that the average gold particles larger than 11 nm with broad size distribution is not favourable for the reactivity in the oxidation process. For Au/ $\text{SiO}_2$  catalyst, the ethanol conversion did not exceed 51 % at the highest experimental temperature which can be correlated to the absence of Brønsted and Lewis acid sites on the support. On the contrary, Au/H-Y-80 which is mildly acidic displayed the highest conversion of ethanol. The results indicate the importance of acid sites in the transformation of ethanol to acetaldehyde and ethyl acetate.

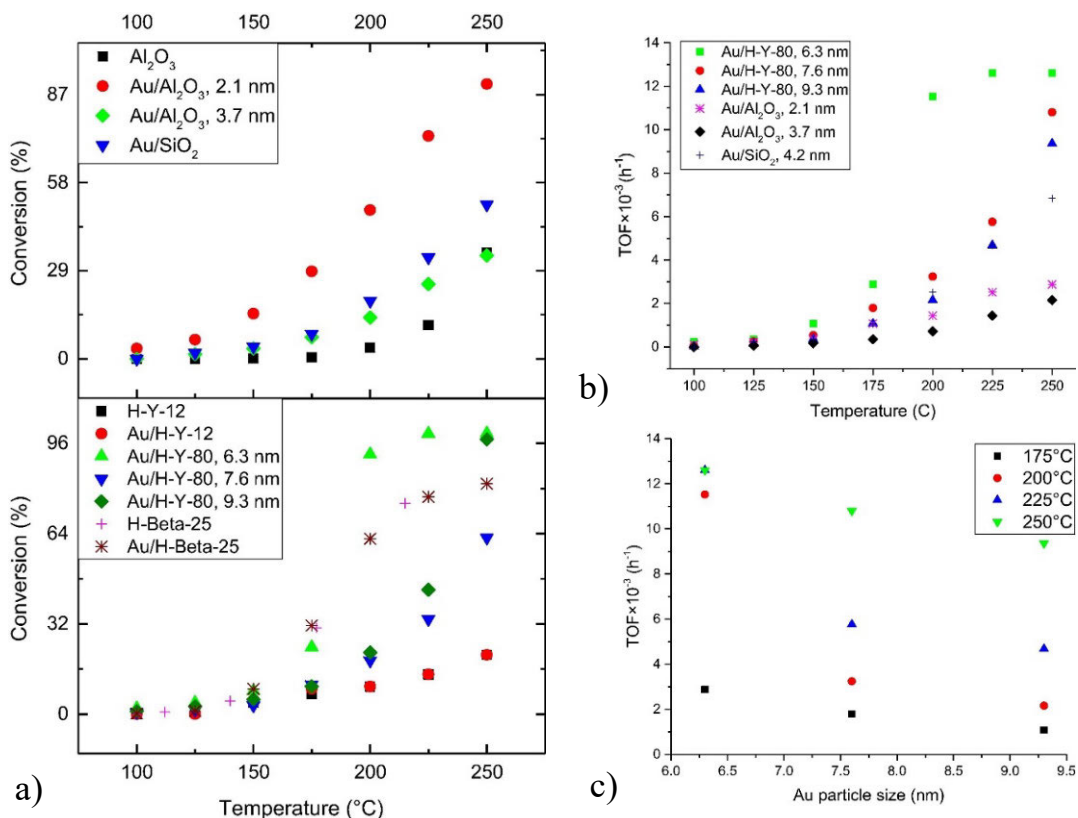


Figure 7. a) Conversion of ethanol versus temperature over neat and Au supported catalysts, b) TOF versus temperature over Au/H-Y-80, Al<sub>2</sub>O<sub>3</sub>, and SiO<sub>2</sub>, and c) effect of Au particle size (on H-Y-80) on TOF at different temperatures

The effect of the Au particle size on catalyst activity can be clearly seen for Au/H-Y-80 and Au/Al<sub>2</sub>O<sub>3</sub> catalysts (Figures 7-b and 7-c). Figure 7-b indicates that the formation of smaller particles especially less than 7 nm could increase the turnover frequency (TOF) substantially. In other words, an increase in TOF was evident with decreasing Au nanoparticle size in the range of 6.3–9.3 nm on H-Y-80. Increase in the temperature in the above mentioned range enhanced TOF significantly (Figure 7-c). A decrease in Au size from 3.7 to 2.1 nm on Al<sub>2</sub>O<sub>3</sub> approximately doubled TOF at temperatures exceeding 150°C.

### 3.1.5. Catalysts selectivity

The selectivities of the catalysts are illustrated in Figure 8. The main product formed on H-Y-12 and H-Beta-25, was diethyl ether which is due to etherification of ethanol. This can be attributed to the stronger acidity of these supports compared with H-Y-80 [74]. Ethylene was another major product formed on H-Y-12 which can be due to the transfer of the Brønsted proton to the hydroxyl group of ethanol resulting in the formation of ethylene directly or an ethyl intermediate, which could then transfer a proton giving ethylene [75].

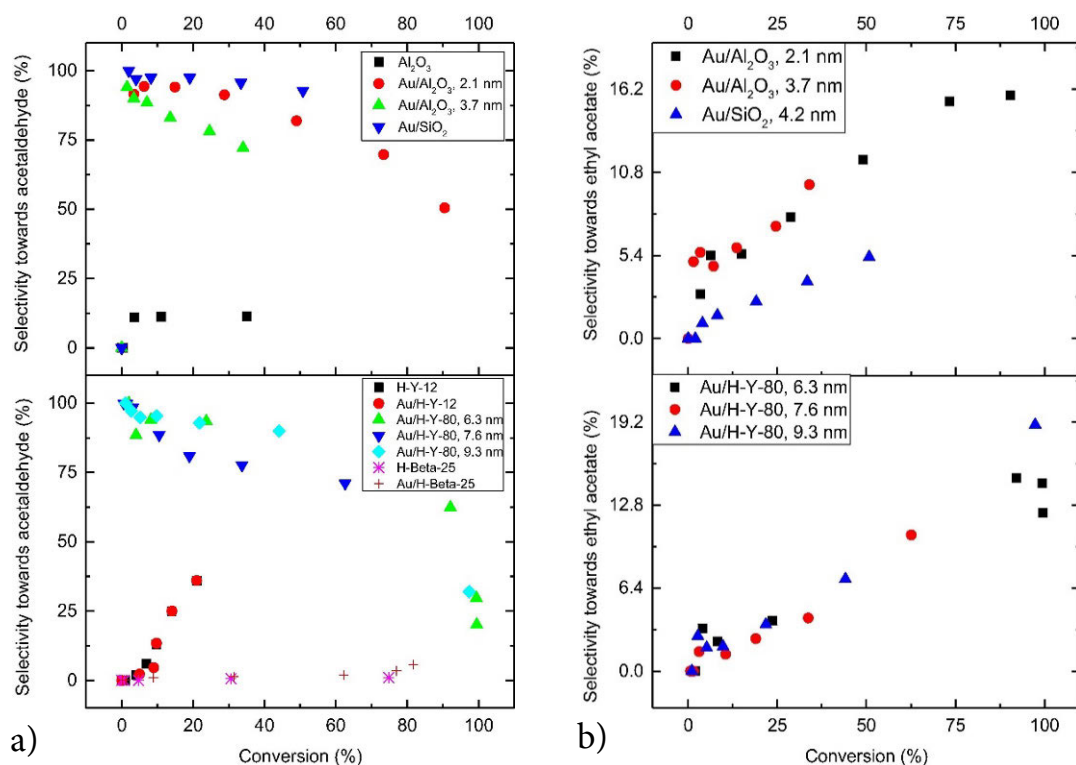


Figure 8. Selectivity towards a) acetaldehyde and b) ethyl acetate as a function of ethanol conversion

Large Au nanoparticles (16.6 nm and 11.2 nm) formed on H-Y-12 and H-Beta-25, respectively, did not alter selectivity after the Au precipitation revealing once again that Au particles of such size are inactive. It is noteworthy that diethyl ether was also the main product formed on  $\text{Al}_2\text{O}_3$  in the entire temperature range. It should be noted that no Brønsted acid sites were detected on  $\text{Al}_2\text{O}_3$ . It was confirmed by DFT calculations

that the adsorption of an oxygen atom of ethanol on the surface Al (Lewis sites) species of  $\gamma$ - $\text{Al}_2\text{O}_3$  is much stronger than on the surface Brønsted sites meaning that the etherification pathway is more favourable on Lewis acid sites leading to the formation of diethyl ether [76].

The less acidic zeolites e.g. the Au/H-Y-80 catalysts produced mainly acetaldehyde. Unlike the selectivity towards ethyl acetate being the same on all the Au/H-Y-80 catalysts, the selectivity towards acetaldehyde varied with the gold nanoparticle size. There was no considerable difference between the selectivity of H-Y-80 with 6.3 nm and 9.3 nm Au towards acetaldehyde. However, the selectivity of H-Y-80 with 7.3 nm Au was considerably lower. The trend of the selectivity change as a function of the ethanol conversion is usually concave down which was not observed here for Au/H-Y-80 (7.6 nm). The reason might be due to the formation of some other products directly from ethanol than from acetaldehyde. The selectivity values indicate that on this particular catalyst, there is a strong contribution of parallel reaction of ethanol to  $\text{CO}_2$ ; the selectivity towards  $\text{CO}_2$  did not change at different conversions of ethanol.

Introduction of gold on H-Beta-25 caused a slight increase in the selectivity towards acetaldehyde without considerable changes towards diethyl ether. However, because of large Au clusters on this support and its strong acidity, the selectivity towards the desired products was much lower than for the Au/H-Y-80 catalysts. A significant amount of  $\text{CO}_2$  was formed on the Au/H-Beta-25 surface which is much higher than on Au/H-Y-80 catalysts. The reason might stem from the differences in the acidities (Brønsted acid sites) of the supports [77]. Generally, on strongly acidic catalysts, reactions of hydrocarbons lead to formation of high amounts of coke [78].

A comparison of the selectivity before and after the gold deposition on  $\text{Al}_2\text{O}_3$  revealed that the Lewis acid sites are responsible for the formation of diethyl ether on this support. Deposition of Au on  $\text{Al}_2\text{O}_3$  prevented the generation of diethyl ether with the main product being acetaldehyde. Two explanations for this observation could be given. First, deposition of gold changes the acidity of alumina, which contradicts the results reported in Table 3 clearly confirming that acidity did not change noticeably. Another possible explanation might be the kinetic differences. In order to assess this issue, etherification under an inert atmosphere was studied. It turned out that on unmodified  $\text{Al}_2\text{O}_3$  in both presence and absence of oxygen, the yield of diethyl ether remained constant (~9 %). However, on Au/ $\text{Al}_2\text{O}_3$  the yield of diethyl ether increased to about 5 % in the absence of oxygen compared to 0.5 % in its presence, meaning that when gold

is deposited on alumina oxidative dehydrogenation becomes more prominent and suppresses etherification. The selectivity of Au/Al<sub>2</sub>O<sub>3</sub> with 2.1 nm Au towards acetaldehyde was considerably higher than that of 3.7 nm Au (Figure 8-a). It is noteworthy that a decrease in the Au nanoparticles size on Al<sub>2</sub>O<sub>3</sub> within the range of 3.7–2.1 nm, did not lead to any noticeable change in the selectivity towards ethyl acetate (Figure 8-b) but to the formation of much less diethyl ether.

On Au/SiO<sub>2</sub> as the least acidic support no diethyl ether and ethylene was detected. The main product was acetaldehyde with a selectivity higher than that observed with Au/Al<sub>2</sub>O<sub>3</sub>. However, the selectivity towards ethyl acetate on Au/SiO<sub>2</sub> was lower.

The highest selectivity towards acetic acid was observed for Au/Al<sub>2</sub>O<sub>3</sub> and Au/H-Y-80 catalysts. Among the Al<sub>2</sub>O<sub>3</sub> and H-Y-80 gold supported catalysts, the ones with the smallest gold nanoparticles (2.1 and 6.3 nm, respectively) showed the highest acetic acid selectivity. No acetic acid was observed for Au/H-Y-12, Au/H-Beta-25, Au/Al<sub>2</sub>O<sub>3</sub> (3.7 nm Au) and Au/SiO<sub>2</sub>. This ascertains the importance of both mild acid sites and small gold nanoparticles for formation of acetic acid. The favourable catalysts and conditions for formation of each product within the temperature range of 100–250°C is briefly illustrated in Figure 9.

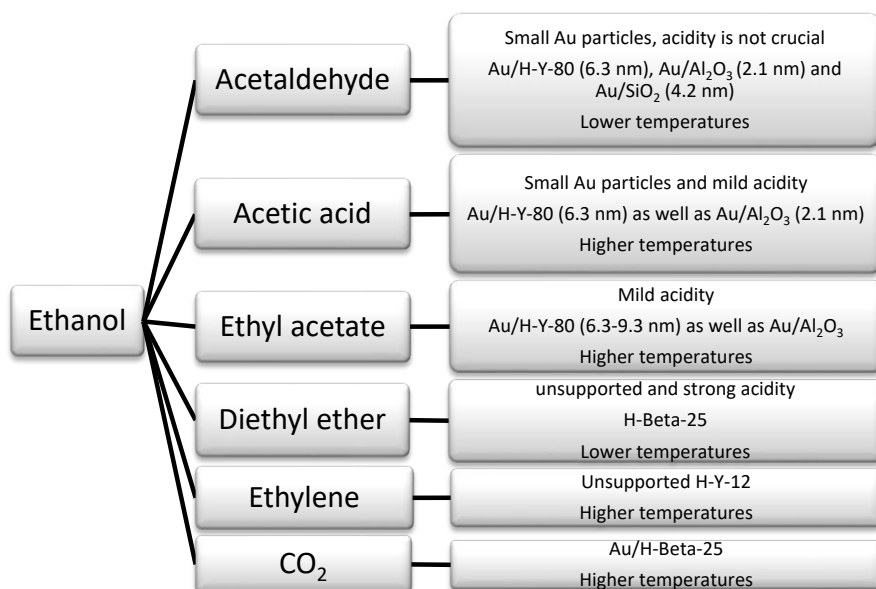


Figure 9. Illustration of the favourable catalysts and conditions for optimization of the products selectivity at comparable ethanol conversions

### 3.2. Catalytic coating of the microreactor

Turning back to the catalytic screening results, since Au/Al<sub>2</sub>O<sub>3</sub> catalyst with 2.1 nm Au showed a high activity as well as a high selectivity to the desired products, this catalyst was selected for coating of the microplatelets. In this work, two methods were applied. The first method was performed by using a ready to use catalyst i.e. Au/Al<sub>2</sub>O<sub>3</sub> without using any binders. The second approach was inkjet printing which was based that, Al<sub>2</sub>O<sub>3</sub> suspension was printed into the microchannels using additives followed by Au deposition on the support via deposition-precipitation method. The catalytic tests were conducted using the microreactor platelets coated via the first method only.

#### 3.2.1. First approach: slurry-based method

This method takes the advantage of the interplay between the catalyst particle size and the viscosity of the catalyst slurry as the most crucial parameters in coating. The catalyst used for coating was reproduced following the same recipe as for the catalyst used in the catalyst screening. The characterization data of the neat  $\gamma$ -Al<sub>2</sub>O<sub>3</sub>, Au/Al<sub>2</sub>O<sub>3</sub> and the aged Au/Al<sub>2</sub>O<sub>3</sub> slurry is summarized in Table 4.

Table 4. Characterization data of the catalyst used for coating

| Catalyst  | Specific surface area (m <sup>2</sup> g <sup>-1</sup> ) | Pore specific volume (cm <sup>3</sup> g <sup>-1</sup> ) | Average Au particle size (nm) | Au dispersion (%) | Average Au loading by EDX (wt%) |
|---|---|---|-------------------------------|-------------------|---------------------------------|
| $\gamma$ -Al <sub>2</sub> O <sub>3</sub>          | 326   | 1   | —                             | —                 | —                               |
| Au/Al <sub>2</sub> O <sub>3</sub>                 | 308   | 0.9   | 1.9                           | 42                | 0.8                             |
| Au/Al <sub>2</sub> O <sub>3</sub><br>(4 day aged) | 314   | 0.7   | —                             | —                 | 0.9                             |

No clear difference can be seen in the surface area of the catalyst after ageing, however, a reduction in the pore specific volume can be due to formation of new phases of alumina and subsequent deposition into the alumina pores. There was no clear difference in the Au loading confirming that the Au nanoparticles were stable on the alumina surface during stirring.

### 3.2.1.1. Catalyst particle size

Stirring even without using any additives or adjusting pH was a successful approach to deagglomerate the particles. Figure 10 demonstrates that the average catalyst particle size was diminished from 20 to 2  $\mu\text{m}$  after four days of stirring. This was in agreement with the scanning electron micrographs (Figure 11) showing much smaller catalyst particles after stirring.

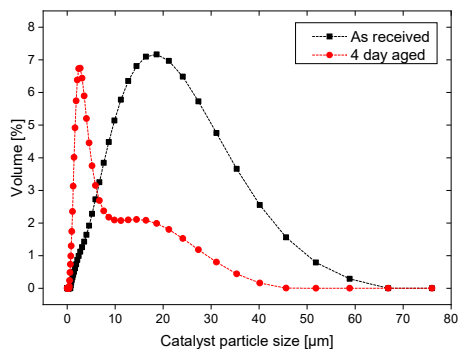


Figure 10. Particle size distribution of the catalyst before and after ageing for four days

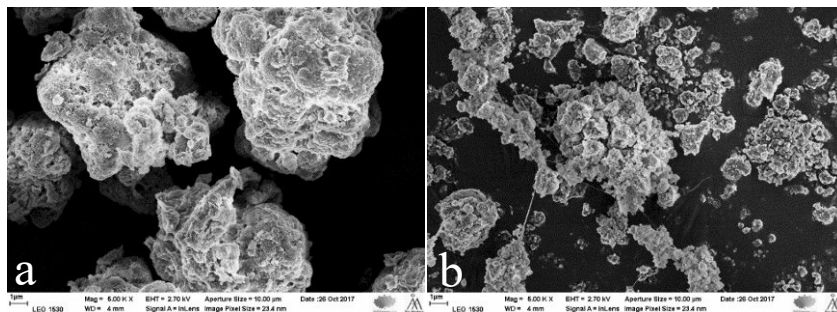


Figure 11. SEM images of the catalyst a) before and b) after four days of stirring

### 3.2.1.2. Viscosity of the catalyst slurry

Besides the catalyst particle size/size distribution, the viscosity of the catalyst slurry plays a crucial role in uniformity of the catalyst layers. Low viscosity causes the slurry to slip down the channel walls forming a catalyst layer thicker at the bottom than on the walls, whereas high viscosity does not allow the slurry to move along the channels. Therefore, viscosity of the catalyst slurry should be optimized. The viscosity

adjustment is usually done for instance by using thickeners, however, in this work, the viscosity was only adjusted by changing the catalyst particle size.

Figure 12 depicts that the viscosity of the slurry increased during ageing. It is noteworthy that viscosity is mainly dependent on pH or particles zeta potential [79] and the particles shape (crystal morphology) [80]. The pH did not change noticeably during ageing. Neither clear differences in the zeta potential measurements were observed, no SEM images showed any clear changes in the particles shape, and no crystallinity distortion of alumina was observed by XRD. Therefore, the reason of the viscosity increase can be correlated to a decrease in the particle size. In other words, as the particles become smaller, first, the effective volume fraction increases because the electric double layer is larger for smaller particles [81] and second, the mean distance between the particles becomes shorter at a given volume fraction increasing the double layer interactions and lowering fluidity [81, 82].

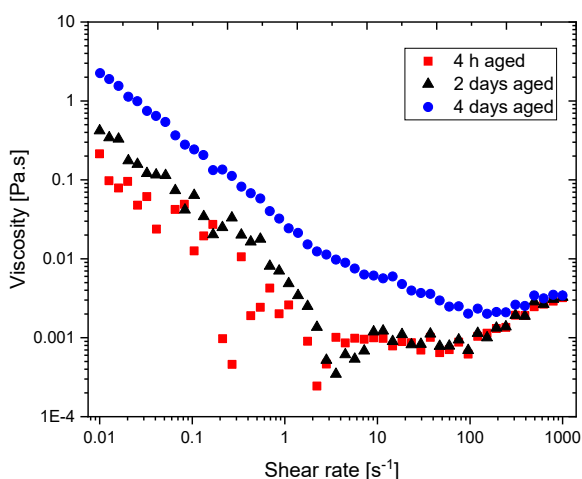


Figure 12. Viscosity measurement of the catalyst slurry during ageing

### 3.2.1.3. Effect of ageing on acidity and structure of the catalyst support

The dissolution of  $\gamma$ -alumina was also investigated by the acidity measurement (Table 5). The concentration of the weak Lewis acid sites of alumina was diminished in the presence of water after four days, which might

be indicative of Al dissolution. Generally, alteration of  $\gamma$ -Al<sub>2</sub>O<sub>3</sub> can be explained by either surface hydration through hydrolysis of Al – O bonds or dissolution of alumina and subsequent precipitation [83, 84].

Table 5. Acidity measurements of the Au/Al<sub>2</sub>O<sub>3</sub> catalyst before and after the four-day ageing

| Catalyst    | Brønsted acid sites |       |       | Lewis acid sites |           |           |
|-------------|---------------------|-------|-------|------------------|-----------|-----------|
|             | 250°C               | 350°C | 450°C | 250°C            | 350°C     | 450°C     |
| As received | 0                   | 0     | 0     | 46.8             | 17.5      | 0         |
| 4 day aged  | 0                   | 0     | 0     | 37.1             | not clear | not clear |

In order to examine the crystallinity of the catalyst, XRD analysis of the neat  $\gamma$ -Al<sub>2</sub>O<sub>3</sub> as well as the Au/Al<sub>2</sub>O<sub>3</sub> catalyst before and after the ageing was performed (Table 6). It is noteworthy that  $\gamma$ -Al<sub>2</sub>O<sub>3</sub> is thermodynamically an unstable phase and has a high tendency to transform to the other phases in aqueous solutions; for instance, 13 wt% of  $\gamma$ -alumina was transformed into bayerite while gibbsite was the minor observed phase, however, the crystallinity of  $\gamma$ -Al<sub>2</sub>O<sub>3</sub> was preserved.

Table 6. The obtained phase weight proportions  $w_i/\Sigma w$  and estimated average crystal sizes  $d_c$  based on the Rietveld refinements

| Sample  | Observed phase<br>(framework)          | $w_i/\Sigma w$ [%] | $d_c$ [nm] |
|---|--|--------------------|------------|
| $\gamma$ -Al <sub>2</sub> O <sub>3</sub>        | Al <sub>2</sub> O <sub>3</sub> (gamma) | 100                | 3 ± 1      |
| Au/Al <sub>2</sub> O <sub>3</sub> (as received) | Al <sub>2</sub> O <sub>3</sub> (gamma) | 100                | 3 ± 1      |
| Au/Al <sub>2</sub> O <sub>3</sub> (4 day aged)  | Al <sub>2</sub> O <sub>3</sub> (gamma) | 82 ± 8             | 5 ± 2      |
|   | Al(OH) <sub>3</sub><br>(bayerite)      | 13 ± 4             | 160 ± 30   |
|   | Al(OH) <sub>3</sub><br>(gibbsite)      | 5 ± 4              | 50 ± 20    |

#### 3.2.1.4. Catalyst layer uniformity

The catalyst layer uniformity inside the microchannels was studied by SEM and confocal microscopy. As illustrated by Figure 13-a, whole channels are covered by the catalyst and no severely uncoated areas were visible. Figure 13-b demonstrates that the catalyst particles stayed on the channel walls and subsequently on the bottom of the channels (Figure 13-c) look very uniform. A close up on the catalyst layer (Figure 13-d) shows only very narrow cracks which are usually formed during drying, however, no sever cracks were

observed. The catalyst layer uniformity was also studied by comparing the layer thickness in the middle and the end of the channels using confocal microscopy. The maximum difference in thickness was only  $1\mu\text{m}$  which is mainly due to the migration of the particles towards the end of the channel as soon as the drying starts.

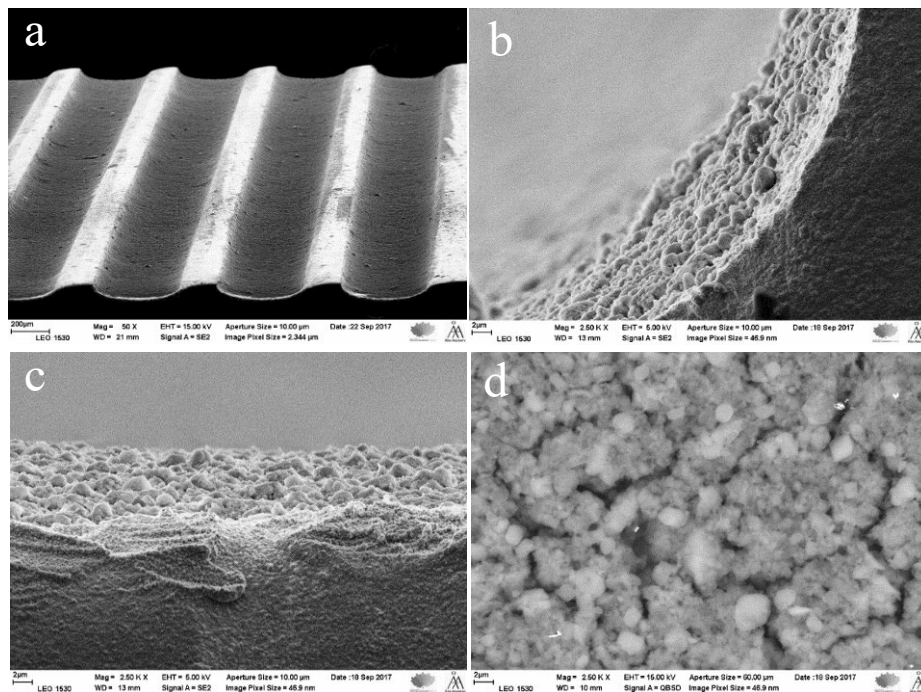


Figure 13. SEM images of a catalyst-coated microplatelet: a) overall view of the channels, b) channel wall, c) bottom of the channel and d) close up on the catalyst layer

### 3.2.1.5. Catalyst layer thickness

Adjusting the catalyst layer thickness while optimizing the uniformity and the stability of the layers is a demanding task which sets new challenges. Herein, the thickness was adjusted by changing the slurry volume ( $2.5\text{--}7\mu\text{l}$ ) while keeping the solid content constant. Table 7 shows the correlation between the slurry volume and the layer thickness.

Table 7. The correlation between 5 wt% catalyst slurry volume in each microplatelet and the coating thickness at the bottom of each channel

| Slurry volume ( $\mu\text{l}$ ) | Coating thickness ( $\mu\text{m}$ ) |
|---------------------------------|-------------------------------------|
| 2.5                             | $4.5 \pm 0.5$                       |
| 3.5                             | $7 \pm 1$                           |
| 5                               | $14 \pm 1$                          |
| 7                               | $19 \pm 1$                          |

The thickness of the catalyst layer at the bottom of the microchannel was measured by using SEM images. The increase in the thickness of the catalyst layers was observed with an increase in the volume of the slurry. On the other hand, cracks are more prone in thicker layers even though the distribution of the catalyst within the channels was uniform. The explanation for the cracks can be due to less interaction between the catalyst particles at the upper part of the thick layers and the surface of the microplates. The microplatelets with 7  $\mu\text{m}$  catalyst layer thickness were thus selected for further studies due to potential instability of thicker layers.

### 3.2.1.6. Catalyst layer stability, durability and regeneration studies

Adhesion of the catalyst layer within the plates was tested by subjecting the plates to a rapid nitrogen flow for five minutes as well as exposition for three hours to ultrasound. No damage to the catalyst layers was observed using SEM confirming a satisfactory layer stability. However, the most reliable stability test is to expose the microplatelets to the reaction conditions. Herein, a reaction test was carried out to examine the stability of the catalyst. Figure 14 shows the ethanol conversion, the turnover frequency (TOF) and the selectivities at different temperatures. As indicated by Figure 14-a, the light-off temperature for ethanol oxidation is 175°C and that the ethanol conversion of 8 % was achieved at 250°C equivalent to TOF of 0.18  $\text{s}^{-1}$ . The selectivity towards acetaldehyde was 100 % up to 200°C decreasing thereafter because of etherification (Figure 14-b). The selectivity towards diethyl ether was ca. 17 % at 225°C, while esterification took place only at the highest utilized temperature giving selectivity of 4 %. A comparison of the selectivity at a comparable ethanol conversion revealed that the main product was acetaldehyde followed by diethyl ether and ethyl acetate (Figure 14-c). No acetic acid, ethylene and  $\text{CO}_2$  were detected.

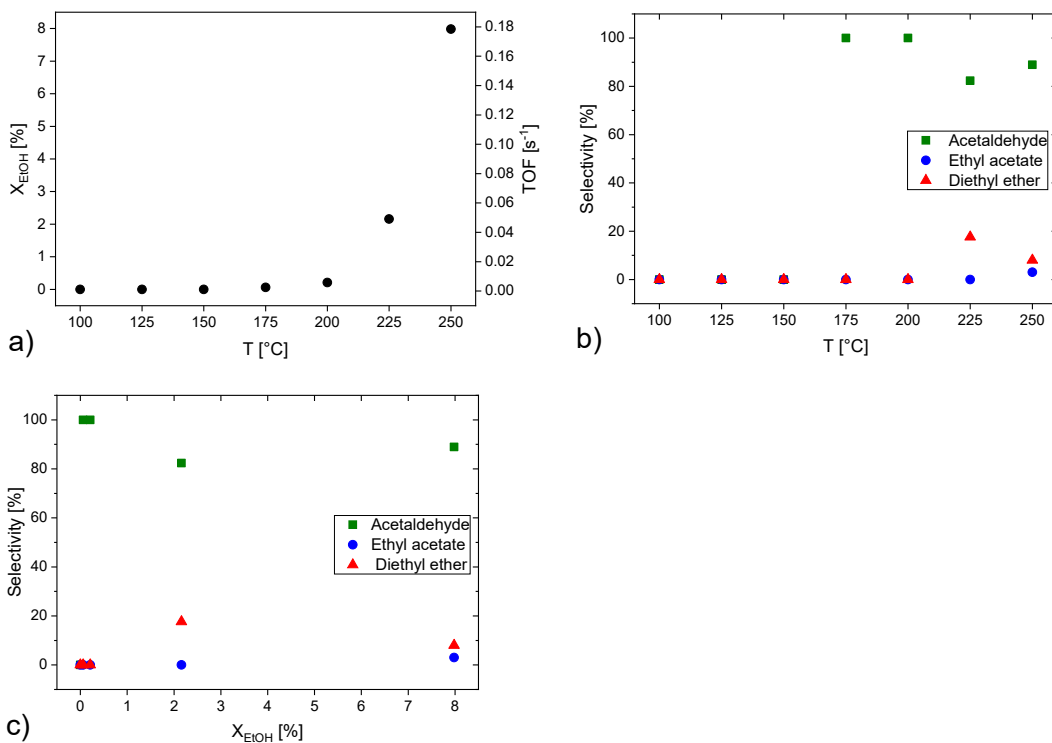


Figure 14. Activity and selectivity of the catalyst in partial oxidation of ethanol in the microreactor at different temperatures

In order to investigate the catalyst durability, a reaction test was continued by keeping the temperature constant at 250°C for about 24 days. The results are summarized in Figure 15 revealing that the catalyst activity increased at the beginning of the experiments as the ethanol conversion elevated from 8 to about 11 % in 10 h while thereafter, it was rather stable for 90 h (Figure 15-c). The ethanol conversion slowly decreased to 8 % during 273 h. The selectivity towards acetaldehyde was initially ca. 88 % and decreased to 76 % during 24 days, while the ethyl acetate selectivity indicated a minor decrease from 4 to 3% during the whole experiment. Etherification was the second dominant reaction which led to formation of diethyl ether giving a selectivity of 10 % at the beginning, but increasing to 20 % at the end of the experiment. There are several reasons for catalyst deactivation including coke formation, sintering of gold nanoparticles and changes in the oxidation state of Au. Coke formation is a very common phenomenon especially for ethanol dehydration over acidic supports being responsible for blockage of the active phase of the catalyst. Therefore, herein, a regeneration experiment was performed to burn out the coke.

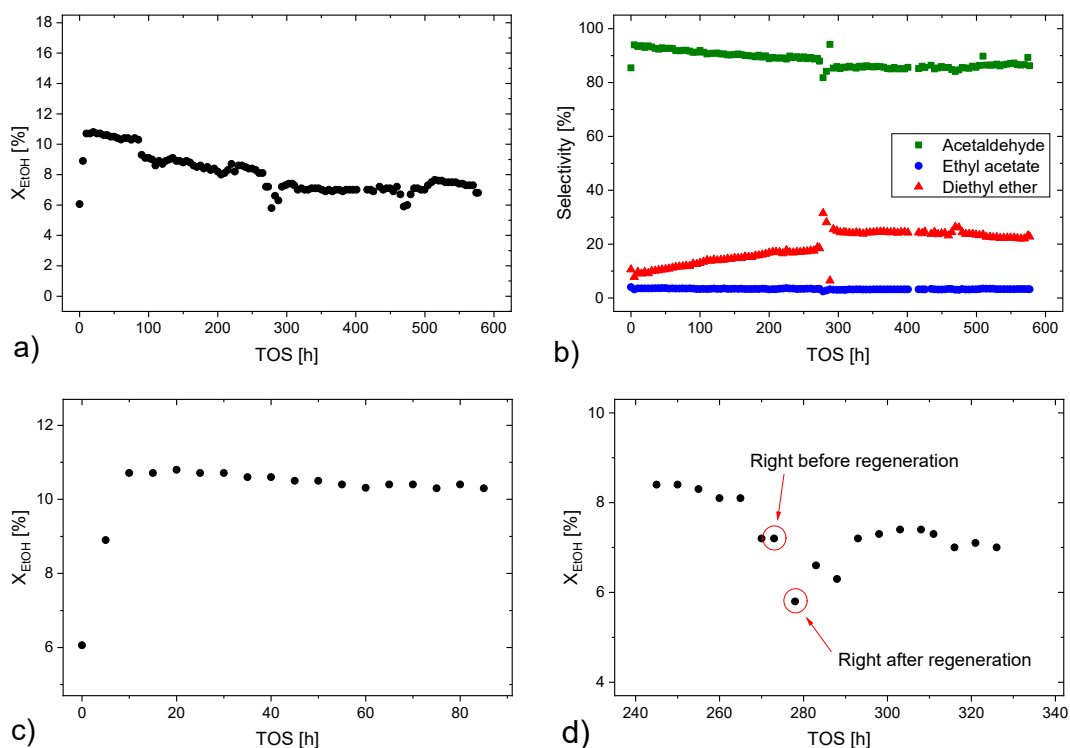


Figure 15. Activity and selectivity of the catalyst during durability studies in the microreactor at 250°C; a) ethanol conversion, b) selectivities, c) conversion at the beginning of the test and d) conversion right after regeneration

The catalyst regeneration was done in-situ by feeding oxygen in helium at 300°C. After 3 h, the oxygen flow was switched off, the temperature was decreased to 250°C followed by feeding the gas mixture of ethanol, oxygen and helium again into the reactor. As revealed by Figure 15-d, a lower ethanol conversion was unexpectedly observed after the regeneration experiment, however, it started to rise again, thereafter becoming relatively stable for 250 h. It can be thus speculated that the activity decrease after the regeneration experiment is related to the presence of leftover coke acting as a reducing agent and changing the oxidation state of Au<sup>0</sup>. Due to a very small catalyst amount, a precise quantification of the amount of coke and its nature is very challenging. Therefore, other available techniques were applied to characterize the stability of the catalyst layer in microplatelets and to reveal the reasons for the catalyst deactivation. SEM images did not reveal any damage to the coating layers within the microchannels, which is a clear indication of a strong

interaction between the catalyst coating layer and the microchannels surface, and hence, further confirming suitability of the coating method. The gold content before and after the oxidation reaction was essentially the same indicating that gold was strongly attached to alumina. The oxidation state of Au measured by XPS remained constant ( $\text{Au}^0$ ). A slight increase in the average Au particle size from 1.9 to 2.8 nm was observed in TEM images implying that sintering of the Au nanoparticles might have occurred. However, the particle size distribution was almost within the same range as for the fresh catalyst. In order to confirm whether sintering of Au nanoparticles was responsible for the decrease in the catalyst activity, structure sensitivity studies were performed using a fixed bed tubular reactor keeping the ethanol-to-oxygen molar ratio constant.

As clearly indicated by Figure 16, the optimum gold particle size was estimated to be between 1.9 and 3.6 nm which implies that Au nanoparticles sintering leading to an increase in the average gold particle size from 1.9 to 2.8 nm, should have resulted in an increase in the catalyst activity rather than deactivation.

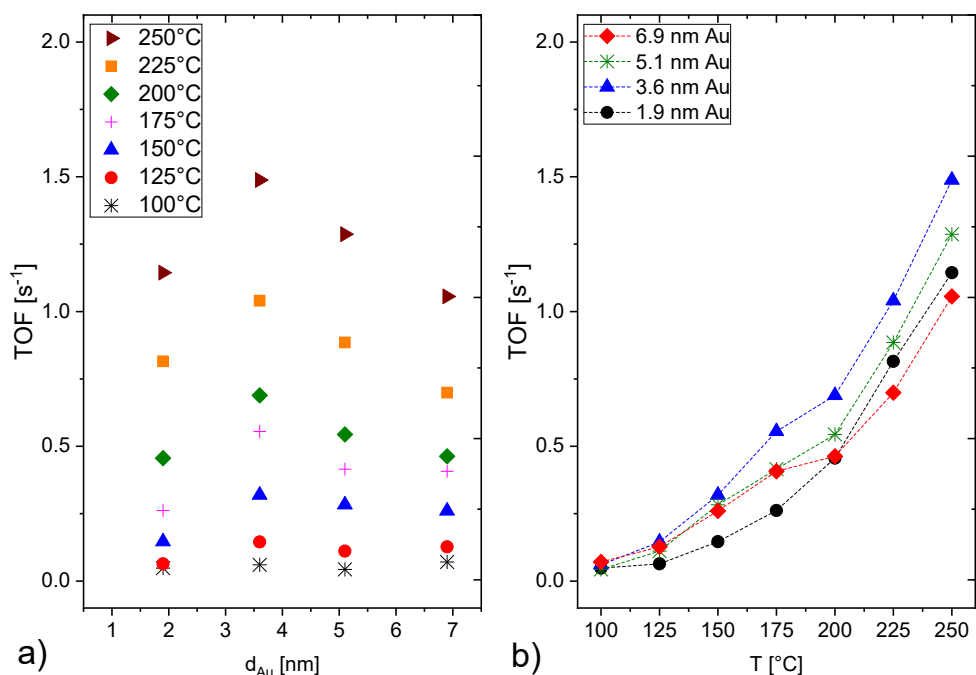


Figure 16. Structure sensitivity studies of  $\text{Au}/\text{Al}_2\text{O}_3$  catalysts in a fixed bed reactor

Summarizing, the main reasons of the catalyst deactivation could not be attributed to the gold particles sintering but can mainly be related to probable coke formation.

Unlike the catalyst deactivation, an increase in the catalyst activity was observed at the beginning of the catalyst durability experiment (Figure 15-c). In order to confirm this activation process, another set of experiments was conducted using fresh coated microplatelets in consecutive experimental cycles (increasing and decreasing the temperature with the same ramp) in the temperature range of 100–250°C (Figure 17-a). The ethanol conversion during the heating and cooling cycles at 150°C is shown in Figure 17-b.

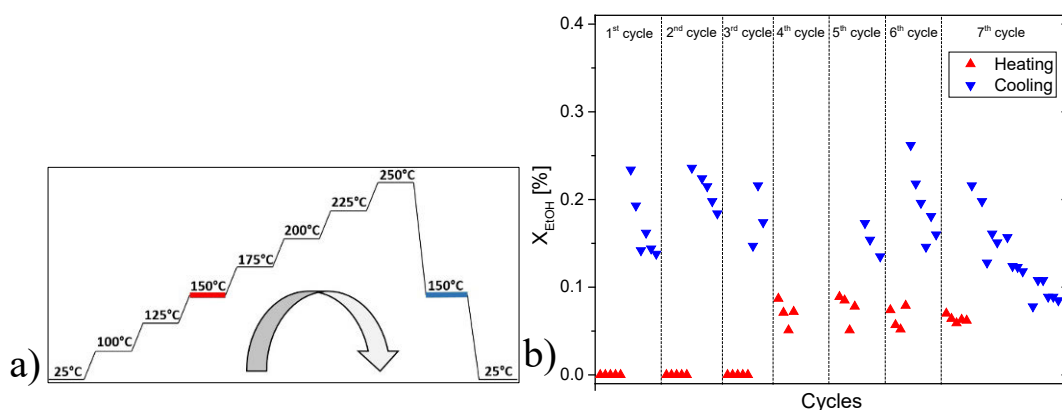


Figure 17. a) The temperature program of one experimental cycle, b) ethanol conversion in consecutive cycles at 150°C; the time interval of the values is 30 minutes

During the ascending stage, the ethanol conversion in the first cycle started from zero and after the third cycle, it was elevated to a slightly higher level, indicating some catalyst activation. A reason for this activation can be changes in the Au oxidation state which later on might have been reduced again by coke acting as reducing agent. Moreover, Figure 17 reveals that conversion is always higher during descending in all cycles compared to the corresponding ascending path. In the second cycle, the conversion of ethanol started again from zero although it was higher in descending in the first cycle. This can be correlated to local overheating of the active sites of the catalyst [85] which means that the actual temperature of the gold particles exceeds that of surroundings. Accordingly, the measured temperature of the catalyst bed decreases while the temperature of the active phase lags behind. As the last cycle indicates, ca. 10 h were required for the catalyst to approach the same conversion level as displayed during the ascending route. After the seventh cycle the

catalyst activity remained relatively constant demonstrating almost a steady-state activity within the whole temperature range.

### **3.2.2. Second approach: inkjet printing**

Inkjet printing has been applied in various industries such as chemistry [86], life sciences [87] and electronics [88], and it is believed that it can be applicable for different catalytic systems as well [89]. Generally, there are two methods of droplet formation via inkjet printing, namely continuous and drop-on-demand (DOD). In the former one, droplets are generated by Rayleigh instability while the ink is continuously pumped through an orifice. In the latter case, the droplets are generated by using a piezoelectric transducer causing pressure waves in a cavity filled with the catalyst ink. For printing especially ceramic and metallic particles, the DOD method is usually preferred as it was used in this work.

In order to print the catalyst ink, due to the small diameter of the printer nozzle, the catalyst particle size should be smaller than 2  $\mu\text{m}$ . Diminishing the catalyst particle size was done by milling and ultrasonication of Au/Al<sub>2</sub>O<sub>3</sub> ( $d_{\text{mean}}=20 \mu\text{m}$ ). Different additives were also tested to change the solid concentration, adjust the surface charge and surface tension of the particles with the aim of deagglomerating the catalyst particles in the slurry, such as ethylene glycol, polyethylene glycol, zetaspers, sodium pyrophosphate, dodecyl sulfate sodium and even by manipulating pH. None of the aforementioned approaches led to very fine particles suitable for printing. Moreover, a new catalyst was synthesized starting from nanopowder alumina having the size of  $d_{50}=20 \text{ nm}$ . This approach was also not successful because of the overlapping of the IEP (isoelectric point) of alumina and the pH at which the smallest gold nano particles are formed. As a result a broad particle size distribution was achieved as it is shown in Figure 18-a, in comparison with a uniform coating obtained via the previous method namely suspension after diminishing the particle size via stirring (Figure 18-b).

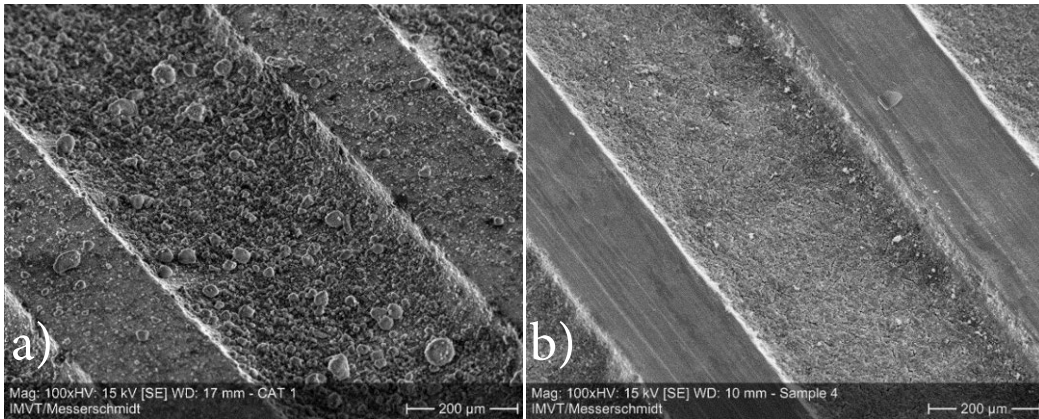


Figure 18. Two microchannels coated with the catalyst having a) broad and b) small and narrow particle size distribution

Subsequent approach was to print a colloidal suspension of alumina into the microchannels followed by deposition of gold nanoparticles later on via the deposition-precipitation method. The results of the coated channels with alumina is illustrated in Figure 19. As this figure shows, a very thin and uniform catalyst layer was successfully printed having 1 µm thickness at the bottom of the microchannels. It is noteworthy that the gold deposition was also confirmed by EDX analysis.

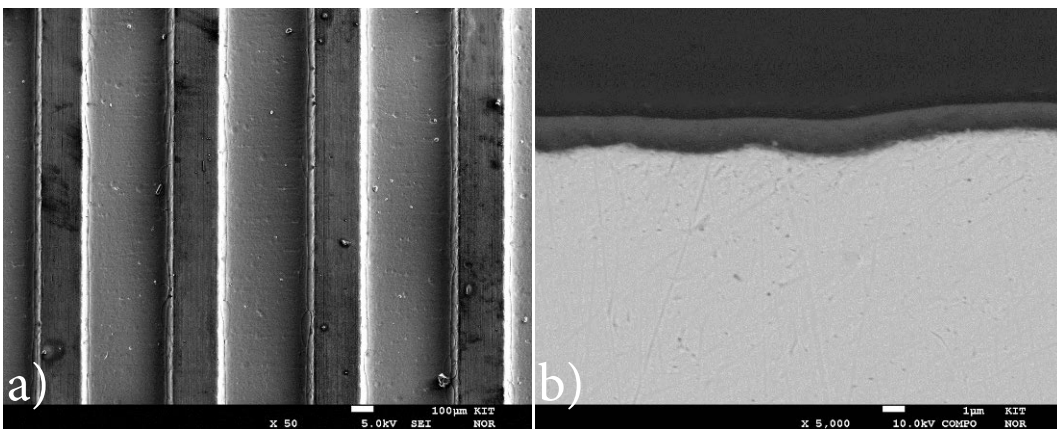


Figure 19. An alumina coated microplatelet via inkjet printing shown from a) the top and b) cross-section

### 3.2.3. Comparison between the two coating methods

In spite of the fact that there are several different methods developed for the coating of the microreactor elements, each method has its advantages as well as disadvantages. It should also be mentioned that a coating method is selected based on the specific properties of the catalyst material, channel dimensions, material of the plates, etc. In this work, two coating methods were introduced and developed for Au/Al<sub>2</sub>O<sub>3</sub> catalyst. The first method was based on a slurry which is suitable for laboratory scale coating because it is quite straightforward and inexpensive without any need for special instruments but only an access of a micropipette. Besides, an already metal modified catalyst can be used in this method. However, this approach suffers from lack of precision concerning the simultaneous coating of a large number of microplatelets at the same time.

On the other hand, inkjet printing is a more precise method; by controlling the printing pitch and droplet size the catalyst layer thickness and the catalyst amount can be regulated. However, preparation of a very stable ink (suspension) is a big challenge. Unlike the slurry based method, inkjet printing is more expensive due to the printer costs especially the printer nozzle. Moreover, in this method binders are used which makes the chemistry more complicated, add more costs to the recipe and makes more challenges such as burning off the binder without damaging the catalyst layers (formation of cracks). It is reported that for instance, temperatures even as high as 600°C is not high enough to decompose PVA binder completely, and using binders in general should be avoided since they can form metal complexes and consequently leading to redispersion of the active phase [90]. As one of the other challenges of the inkjet printing it can be referred to printing of the thick catalyst layers. This is because the ink droplets are very small (here 88 μm in diameter; Figure 20-a), therefore, many layers should be printed above each other with drying in between, which might take a long time. As a consequence, formation of cracks would be quite probable altering the layers uniformity. Alongside the aforementioned consequences, there are several technical challenges to be formulated while working with the printer such as determining the combination of voltage and pulse, stabilizing the droplets formations to avoid splashing by adjusting the viscosity and velocity of the ejected droplets.

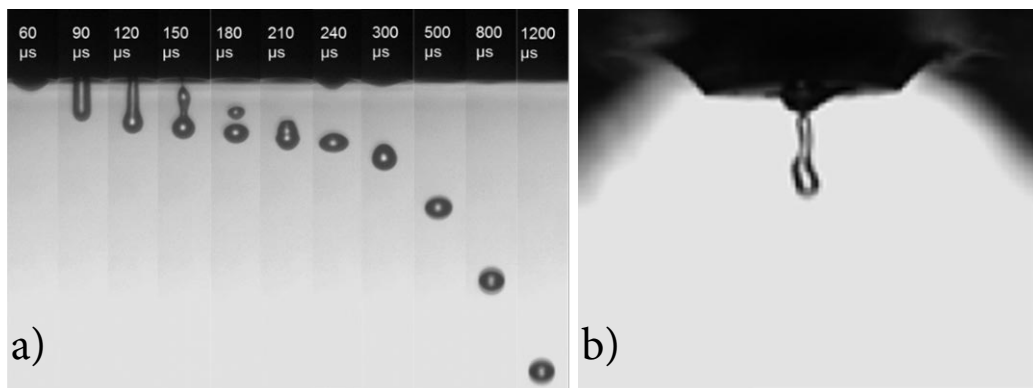


Figure 20. a) A uniform versus b) non-uniform catalyst ink droplet formation

It is noteworthy as it was mentioned above, the viscosity of the slurry/suspension is very crucial for coating since it determines the shape of the layers. As a comparison, Figure 21 illustrates the cross-section of two microchannels coated via the two different coating methods. The difference in viscosity of the catalyst slurry in the first method and the alumina suspension in the second method, caused the formation of layers so-called U (Figure 21-a) versus V shape (Figure 21-b), respectively. U-shape implies that more catalyst is deposited on the bottom of the channel than on the walls, while the opposite is valid for the V-shape.

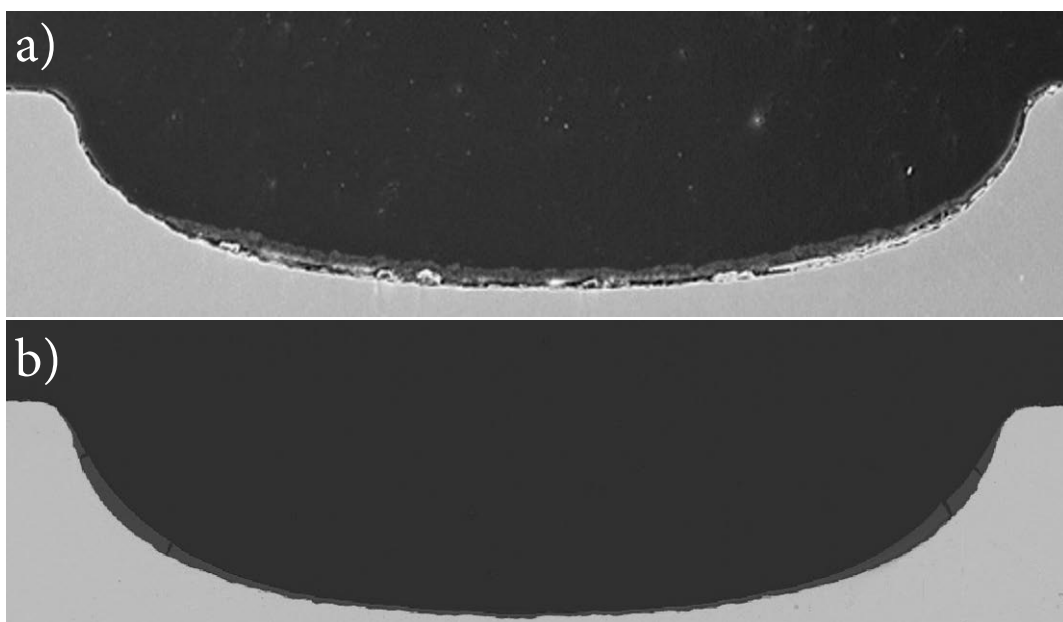


Figure 21. The cross-section of two microchannels coated via a) slurry based method and b) inkjet printing

### 3.3. Kinetic modelling of ethanol oxidation in the fixed bed reactor

A mathematical model was generated to explain the experimentally observed reactor behavior (conversion of ethanol and yields of products) in the ethanol oxidation on gold nanoparticles (here Au/H-Y-80 having 6.3 nm and 1.37 wt% Au). The model for this heterogeneously catalyzed gas-phase multi-reaction system consisted of the dynamic mass and energy balances and Langmuir–Hinshelwood–Hougen–Watson, Mars van Krevelen and power law expressions for the reaction kinetics. The fluid flow was described with convection and dispersion terms. A semi-empirical pressure drop correlation was used. The dynamic mass balances consisting of internal diffusion effects and surface reactions in the porous catalyst particles were solved simultaneously with the mass and energy balances of the whole reactor. The axial and radial concentration and temperature profiles inside the reactor and the concentration profiles in the particles were obtained as the main results. Starting from experiments performed at  $T = 125\text{--}250\text{ }^\circ\text{C}$  and  $p = 1\text{ atm}$  and superficial gas velocity of 0.03 m/s, a parameter estimation analysis was conducted. The estimated parameters were the rate constants including the activation energies and the adsorption parameters (for LHHW and Mars van Krevelen kinetics) and reaction order of oxygen (for power law kinetics). Simulation studies were done to reveal how the catalyst loading influenced the results and how the Péclet number affected the ethanol conversion and the product distribution.

The model consists of partial differential equations (PDEs) for the dynamic mass and energy balances. The PDEs were solved numerically by using the numerical method of lines. The mass balance for a gaseous component  $i$  is given by

$$\varepsilon_G \frac{\partial C_{i,G}(t,z,r)}{\partial t} = - \frac{\partial(u_G(z,r) C_{i,G}(t,z,r))}{\partial z} + \varepsilon_G D_{z,G} \frac{\partial^2 C_{i,G}(t,z,r)}{\partial z^2} + \varepsilon_G D_{r,G} \left( \frac{\partial^2 C_{i,G}(t,z,r)}{\partial r^2} + \frac{1}{r} \frac{\partial C_{i,G}(t,z,r)}{\partial r} \right) - N_{G,S,i} \quad (7)$$

where the flux of the component  $i$  from gas to the solid is

$$N_{G,S,i} = \frac{D_{eff,S}}{R_p} \frac{\partial C_{i,S}}{\partial r_p} \Big|_{r=R_p} \quad (8)$$

The energy balance of the entire catalyst bed is

$$\frac{\partial T_B(t,z,r)}{\partial t} = -\frac{\partial(u_G(z,r) T_B(t,z,r))}{\partial z} + D_{z,G} \frac{\partial^2 T_B(t,z,r)}{\partial z^2} + D_{r,G} \left( \frac{1}{r} \frac{\partial T_B(t,z,r)}{\partial r} + \frac{\partial^2 T_B(t,z,r)}{\partial r^2} \right) + \frac{\lambda_{z,B}}{\rho_B C_{p,B}} \frac{\partial^2 T_B(t,z,r)}{\partial z^2} + \frac{\lambda_{r,B}}{\rho_B C_{p,B}} \left( \frac{1}{r} \frac{\partial T_B(t,z,r)}{\partial r} + \frac{\partial^2 T_B(t,z,r)}{\partial r^2} \right) \quad (9)$$

where the terms from left to right describe accumulation, convection, axial and radial dispersion and axial and radial conduction, respectively.

The mass balance of the component  $i$  in the catalyst particle is

$$\frac{\partial C_{i,s}(t,z,r,r_p)}{\partial t} = \frac{D_{eff,i}}{\varepsilon_s} \left( \frac{\partial^2 C_{i,s}(t,z,r,r_p)}{\partial r_p^2} \right) + \frac{s}{r} \frac{\partial C_{i,G}(t,z,r,r_p)}{\partial r_p} + \rho_s \frac{\varepsilon_G}{\varepsilon_s} \sum \left( v_{i,j} r_{i,j}(t,z,r,r_p) \right) \quad (10)$$

Figure 22 illustrates the corresponding boundary conditions. At  $t=0$  the concentration and temperature were assumed to be equal to that of the feed concentration and temperature.

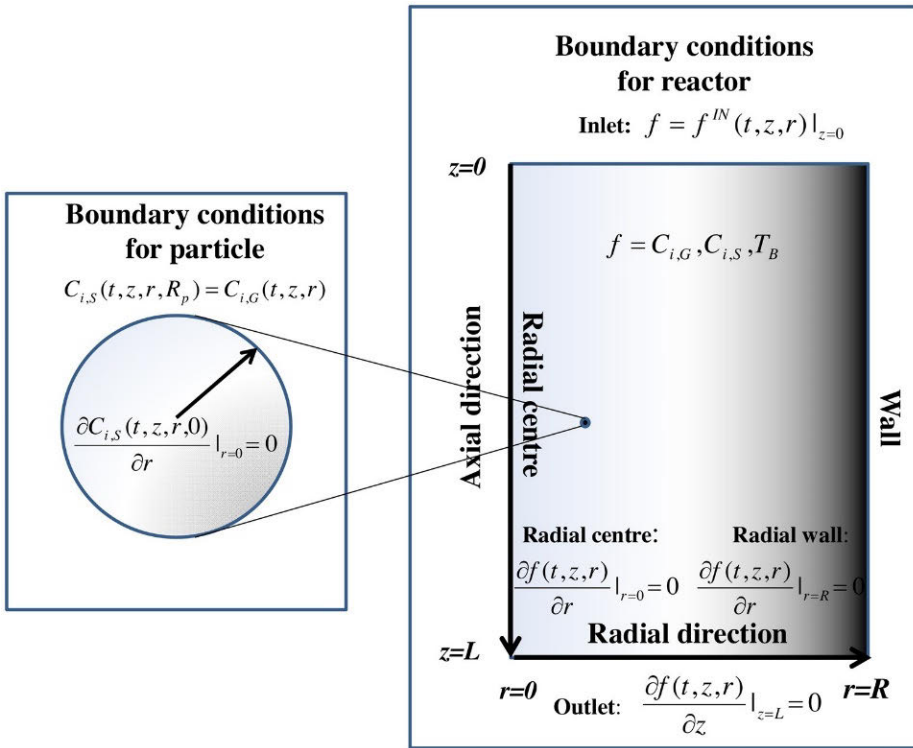


Figure 22. Illustration of the boundary conditions for the reactor and the catalyst particle

The pressure drop (Ergun equation), friction factor and the Reynolds number for the packed bed were calculated as follows [91]:

$$\Delta P/L = f_p \frac{\rho_G u_G^2}{d_p} \left( \frac{1 - \varepsilon_G}{\varepsilon_G^3} \right), \quad f_p = \frac{150}{Re_p} + 1.75, \quad Re_p = \frac{\rho u_G d_p}{(1 - \varepsilon_G) \mu_G} \quad (11-13)$$

According to Ergun equation, the generated pressure drop over the short packed bed reactor became 0.03 bar due to the low density and viscosity of the gas. A conservative value of 0.1 bar was used in the simulations because Ergun equation is given for a single particle size, whereas the particles used in the actual experiments had a size distribution.

The thermal conductivity of the fixed bed was assumed to be a kind of volume fraction weighed average conductivity of gas and solid (Eq. 15) [91]. The catalyst support had a rather low conductivity.

$$\lambda_B = \lambda_G \left( \lambda_S / \lambda_G \right)^{(1 - \varepsilon_s)} \quad (14)$$

Molecular diffusivity was calculated based on Fuller-Schettler-Giddings equation [92]

$$D_{A,B} = \frac{10^{-3} T^{1.75} \left( \frac{1}{M_A} + \frac{1}{M_B} \right)^{0.5}}{p \left( (\sum v_A)^{1/3} + (\sum v_B)^{1/3} \right)^2} \quad (15)$$

The physical properties of the gas phase and the fixed bed are summarized in Table 8.

Table 8. Physical properties of the gas inlet at feed temperatures of 125 and 250°C and 1 bar [93–95]

| Parameter                     | Value          | Unit               |
|-------------------------------|----------------|--------------------|
| $\rho_G$                      | 0.35, 0.27     | kg/m <sup>3</sup>  |
| $\mu_G$                       | 1.3e-5, 1.8e-5 | kg/(m.s)           |
| $C_{P,G}$                     | 34, 34.5       | J/(mol.K)          |
| $C_{P,B}$                     | 2              | kJ/(kg.K)          |
| $D_{EtOH}, D_{Ald}, D_{EtAc}$ | 1, 1.6         | cm <sup>2</sup> /s |
| $D_{H_2O}, D_{O_2}$           | 1.9, 3–1.6, 3  | cm <sup>2</sup> /s |
| $\lambda_B$                   | 0.15           | W/(m.K)            |
| $\Delta H_{r,1}$              | -51            | kJ/mol             |
| $\Delta H_{r,2}$              | -267           | kJ/mol             |
| $\Delta H_{r,3}$              | 34.3           | kJ/mol             |

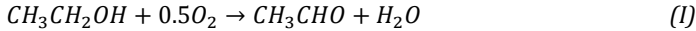
The other important parameters including the reactor and particle dimensions, reaction conditions as well as heat and mass transfer parameters are listed in Table 9.

Table 9. Dimensions, operating conditions and heat and mass transfer parameters

| Mass and heat transfer |      |           | Reactor and catalyst |                      |      | Initial conditions |          |             |
|------------------------|------|-----------|----------------------|----------------------|------|--------------------|----------|-------------|
| $Pe_G$                 | 10   | —         | $L$                  | $8 \cdot 10^{-3}$    | $m$  | $u_G^0$            | 0.03     | $m/s$       |
| $\lambda_B$            | 0.15 | $W/(m.K)$ | $R$                  | $5 \cdot 10^{-3}$    | $m$  | $C_{EtOH,G}^0$     | 2.3      | $mol/m^3$   |
|                        |      |           | $R_p$                | $3.15 \cdot 10^{-5}$ | $m$  | $C_{H_2O,G}^0$     | 0        | $mol/m^3$   |
|                        |      |           | $\omega_{cat}$       | $0.16 \cdot 10^{-3}$ | $kg$ | $C_{Alde,G}^0$     | 0        | $mol/m^3$   |
|                        |      |           | $\epsilon_G$         | 0.6                  | —    | $C_{Acid,G}^0$     | 0        | $mol/m^3$   |
|                        |      |           | $\epsilon_s$         | 0.4                  | —    | $C_{EtAc,G}^0$     | 0        | $mol/m^3$   |
|                        |      |           | $s$                  | 2                    | —    | $C_{O_2,G}^0$      | 2.3, 7   | $mol/m^3$   |
|                        |      |           |                      |                      |      | $p$                | 1        | $atm$       |
|                        |      |           |                      |                      |      | $T_B^{IN}$         | 125, 250 | $^{\circ}C$ |

### 3.3.1. Kinetic modelling

The main reactions considered in the model were ethanol oxidation to acetaldehyde, acetaldehyde oxidation to acetic acid and generation of ethyl acetate from ethanol. The extent of total oxidation of ethanol to carbon dioxide and water was insignificant under the studied conditions. The reactions included were



Based on thermodynamic calculations, the equilibrium constant of all the reactions were quite high implying irreversible reactions. Ethyl acetate can basically be formed in two ways; either via disproportionation of two acetaldehyde molecules (Tishchenko reaction) or via esterification of the acetic acid with ethanol. Since only small amounts of ethyl acetate were formed, discriminating between the two aforementioned reactions was in practice not possible. Therefore, both the reactions were incorporated in the model, showing the same results due to uncertainty in the estimated parameters. Herein, only the results obtained by considering the Tishchenko reaction are shown. The reaction kinetics of the reactions was based on LHHW, Mars van Krevelen and power law expressions (Table 10). They included the combined effect of surface reactions and adsorption steps. Oxygen, ethanol and water adsorption terms were included in the LHHW kinetics, but

only oxygen adsorption term in Mars van Krevelen expressions. Power laws are semi-empirical expressions which maintain the reaction orders constant and do not directly account for adsorption effects. In order to improve the identification of parameters in the estimation stage, the Arrhenius expression for the rate constant was rewritten in a modified form, Eq. 17. The parameters to be estimated in pursuit to obtain reaction kinetics became the reaction rate constant at the reference temperature and the activation energy of each individual reaction, the adsorption constants (LHHW and Mars van Krevelen) and the exponents for oxygen (power law).

$$k_j = k_{j,ref} \exp \left[ \frac{-E_{a,j}}{R_g} \left( \frac{1}{T_s(t, z, r, r_p)} - \frac{1}{T_{ref}} \right) \right] \quad (16)$$

Table 10. Kinetic equations for partial oxidation of ethanol (1), acetaldehyde oxidation (2) and ethyl acetate formation (3)

| Mars-van Krevelen  | LHHW  | Power law                        |
|--|---|----------------------------------|
| $r_1 = \frac{k_1 p_{EtOH}}{1 + \frac{k_1 p_{EtOH}}{2k_2 p_{O_2}^{1/2}}}$ | $r_1 = \frac{k'_1 p_{EtOH} p_{O_2}^{1/2}}{(1 + K_{EtOH} p_{EtOH} + (K_{O_2} p_{O_2})^{1/2} + K_{H_2O} p_{H_2O} + K_{Alde} p_{Alde})^2}$ | $r_1 = k_1'' p_{EtOH} p_{O_2}^m$ |
| $r_2 = \frac{k_3 p_{Alde}}{1 + \frac{k_3 p_{Alde}}{2k_2 p_{O_2}^{1/2}}}$ | $r_2 = \frac{k'_2 p_{Alde} p_{O_2}^{1/2}}{(1 + K_{EtOH} p_{EtOH} + (K_{O_2} p_{O_2})^{1/2} + K_{H_2O} p_{H_2O} + K_{Alde} p_{Alde})^2}$ | $r_2 = k_2'' p_{Alde} p_{O_2}^n$ |
| $r_3 = k_3 p_{Alde}$   | $r_3 = \frac{k'_3 p_{Alde}}{(1 + K_{EtOH} p_{EtOH} + (K_{O_2} p_{O_2})^{1/2} + K_{H_2O} p_{H_2O} + K_{Alde} p_{Alde})^2}$               | $r_3 = k_3'' p_{Alde}$           |

### 3.3.2. Parameter estimation results

The rate expressions were evaluated by conducting parameter estimation for two sets of experimental data consisting of two oxygen-to-ethanol molar ratios (1 and 3) within the temperature range of 125–250°C. The temperature was stepwise increased with 2.5 h of dwelling time at each set point, hence, steady state conditions for the system were verified. Table 11 shows the final parameter estimation results including the activation energies, rate constants as well as the adsorption parameters for LHHW and Mars-van Krevelen and the oxygen exponents for the power law experiments.

Table 11. Parameter estimation results for different kinetic expressions.  $T_{ref} = 403\text{ K}$

| Mars-van Krevelen                    |                      | LHHW                                  |                      | Power law                              |                      |
|--------------------------------------|----------------------|---------------------------------------|----------------------|--|----------------------|
| $E_{a,1}[kJ/mol]$                    | 123                  | $E_{a,1}[kJ/mol]$                     | 125.3                | $E_{a,1}[kJ/mol]$                      | 105                  |
| $E_{a,2}[kJ/mol]$                    | 87                   | $E_{a,2}[kJ/mol]$                     | 112.3                | $E_{a,2}[kJ/mol]$                      | 108                  |
| $E_{a,3}[kJ/mol]$                    | 71                   | $E_{a,3}[kJ/mol]$                     | 81.45                | $E_{a,3}[kJ/mol]$                      | 87                   |
| $E_{a,o_2\ ads}[kJ/mol]$             | 34                   | $k'_{1,ref}[\text{mol/g/s/Pa}^{1.5}]$ | $3.36 \cdot 10^{-5}$ | $k''_{1,ref}[\text{mol/g/s/Pa}^{m+1}]$ | $7.11 \cdot 10^{-5}$ |
| $k_{1,ref}[\text{mol/g/s/Pa}]$       | $4.79 \cdot 10^{-6}$ | $k'_{2,ref}[\text{mol/g/s/Pa}^{1.5}]$ | $6.13 \cdot 10^{-6}$ | $k''_{2,ref}[\text{mol/g/s/Pa}^{n+1}]$ | $1 \cdot 10^{-6}$    |
| $k_{2,ref}[\text{mol/g/s/Pa}^{0.5}]$ | $1.27 \cdot 10^{-5}$ | $k'_{3,ref}[\text{mol/g/s/Pa}]$       | $2.4 \cdot 10^{-4}$  | $k''_{3,ref}[\text{mol/g/s/Pa}]$       | $5.55 \cdot 10^{-5}$ |
| $k_{3,ref}[\text{mol/g/s/Pa}]$       | $3.1 \cdot 10^{-6}$  | $k_{EtOH}[1/Pa]$                      | $1.53 \cdot 10^{-2}$ | m [-]                                  | 1.81                 |
| $k'_{4,ref}[\text{mol/g/s/Pa}]$      | $1.98 \cdot 10^{-6}$ | $k_{O_2}[1/Pa]$                       | $1 \cdot 10^{-4}$    | n [-]                                  | 0.78                 |
|                                      |                      | $k_W[1/Pa]$                           | $2 \cdot 10^{-3}$    |  |                      |

The aim of the kinetic modelling was to compare the conversion of ethanol and the yield of the main products namely acetaldehyde and acetic acid with those obtained from the experiments. Theoretically the kinetic models differ from each other, especially the rate constants are not directly comparable. On the other hand, the activation energies could be compared as follows. The activation energy of the ethanol and acetaldehyde oxidation were around 105–125 and 100 kJ/mol, respectively. Due to the high correlation of the parameters for the power law the oxygen reaction order (m) was not reliable. The agreement between the experimental data and all the models was satisfying. The obtained concentration profiles according to the LHHW model are illustrated in Figure 23.

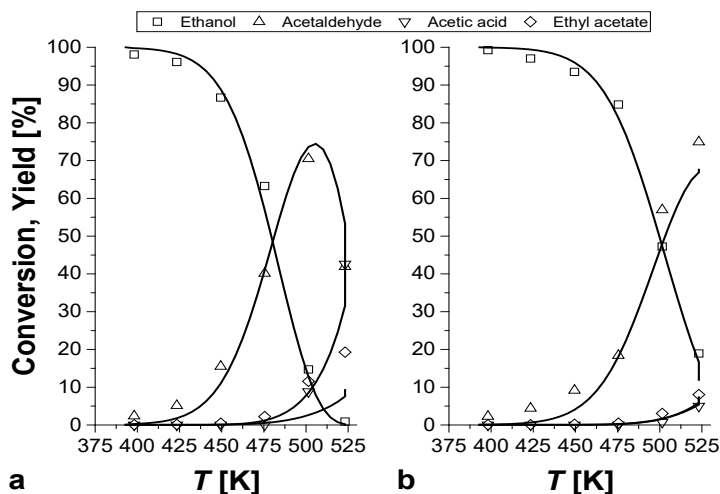


Figure 23. Experimental data collected by fixing the oxygen to ethanol ratio to a) 3 and b) 1. The calculated profiles refer to the prediction of LHHW model

All three approaches were able to describe well the experimentally observed behaviors for both equimolar and oxygen excess cases. The conversion of ethanol systematically increased as the operation temperature was increased. Acetaldehyde formation was the first reaction observed. The model was capable to predict the maximum yield at the correct temperature. Above 200°C, the acetic acid generation became gradually more important. In the excess of oxygen, the oxidation reactions took place at lower temperatures compared to the equimolar case. The reason that all kinetic approaches resulted in a similar behavior was due to having very diluted gas mixture (80 % dilution with helium) suppressing the adsorption effects.

### 3.3.3. Simulation studies

The simulation study was conducted after the parameter estimation for three purposes: to illustrate the effect of the catalyst loading and uncertainties in the Péclet number on the obtained ethanol conversion and the products yields as well as the effect of the feed temperature. Herein, the effect of catalyst loading and Péclet number are demonstrated in Figure 24.

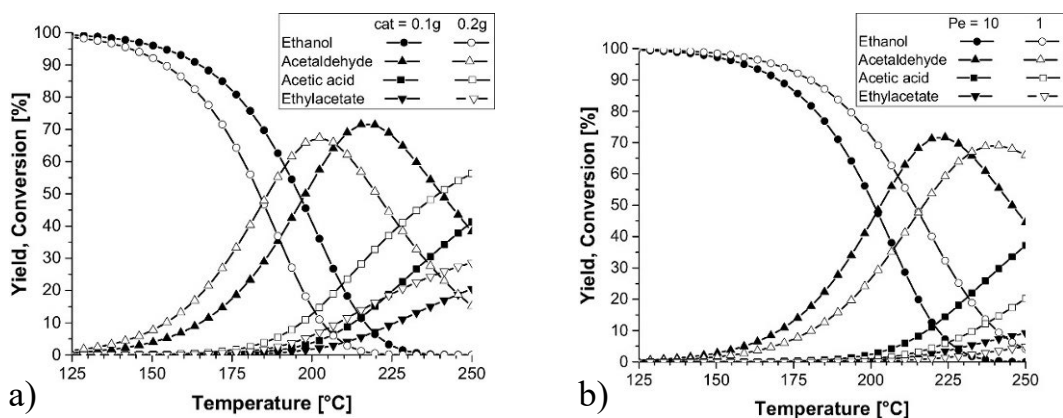


Figure 24. Effect of the catalyst loading and Péclet number on the obtained conversion and yields

Figure 24-a shows that when the catalyst amount was doubled from 0.1 to 0.2 g, the reaction rates were increased which resulted in higher yields at lower temperatures. When the Péclet number was decreased from 10 to 1 (Figure 24-b), the productivity was suppressed and higher temperatures were demanded to reach similar yields. Higher Péclet numbers up to 100 were also tested; they totally overlapped with the results of  $Pe=10$  implying that Péclet number equal to 10 was high enough to resemble a plug flow.

### 3.4. Kinetic modelling of ethanol oxidation in the microreactor

After the development of a coating method of microchannels, a separate modelling effort was conducted using a similar catalyst (Au/Al<sub>2</sub>O<sub>3</sub> with 2.1 nm and 0.56 wt% of Au) for the partial oxidation of ethanol. A kinetic model was developed for the reaction system. Dynamic mass balance-based generic modelling was applied to estimate the rate parameters. The reaction system was studied by changing the operation conditions, i.e. the residence time and temperature (100–250°C). The aim was to reveal the operation conditions that favored acetaldehyde formation. Ethyl acetate, diethyl ether and ethylene were generated to a minor extent. Formation of acetic acid was not observed under the studied circumstances. CO<sub>2</sub> was not detected, because the temperature range was selected well below the temperatures favoring total oxidation.

#### 3.4.1. Kinetic modelling

All the mass balances were written in the transient form i.e. they are expressed as PDEs. The operation of the reactor was modelled so that the reaction temperature was let rise slowly. The dwelling time at each temperature was set long enough that the system reached the steady state after each temperature jump. The mass balances were formulated as listed below.

Dynamic mass balance for each component in the gas phase:

$$\frac{\partial C_{i,G}}{\partial t} = -\frac{\partial(u_G C_{i,G})}{\partial z} + D_z \frac{\partial^2 C_{i,G}}{\partial z^2} + D_r \left( \frac{\partial^2 C_{i,G}}{\partial r^2} + \frac{1}{r} \frac{\partial C_{i,G}}{\partial r} \right) \quad (17)$$

Dynamic mass balance for each component inside the catalyst coated layer:

$$\varepsilon_p \frac{\partial C_{i,S}}{\partial t} = -D_{eff,i} \left( \frac{\partial^2 C_{i,S}}{\partial r_p^2} + \frac{1}{r_p} \frac{\partial C_{i,S}}{\partial r_p} \right) + \sum_j \nu_{ij} r_j \quad (18)$$

Boundary conditions for the mass and balances of components in the gas and solid phase:

$$z=0: \text{Feed concentrations equal: } C_{i,G} \Big|_{z=0} = C_{i,S} \Big|_{z=0} = C_{i,Feed} \quad (19)$$

$$z=L: \text{Axial gradients become zero: } \frac{\partial C_{i,G}}{\partial z} \Big|_{z=L} = \frac{\partial C_{i,S}}{\partial z} \Big|_{z=L} = 0 \quad (20)$$

$r=0$ : Radial gradients at the center of the tube become zero due to symmetry:

$$\left. \frac{\partial C_{i,G}}{\partial r} \right|_{r=0} = 0 \quad (21)$$

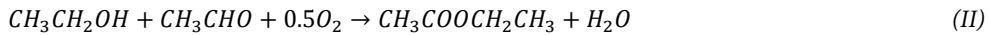
$r=R$ : Gas-solid interface:

$$C_{i,S} \Big|_{r_p=R} = C_{i,G} \Big|_{r=R} \quad (22)$$

Net flux change is equal to the flux through the interface:

$$\left. \frac{\partial(u_G C_{i,G})}{\partial z} \right|_{z=R} - D_z \frac{\partial^2 C_{i,G}}{\partial z^2} = D_{eff,i} \frac{1}{R_w - R} \left. \frac{\partial C_{i,S}}{\partial r_p} \right|_{r_p=R} \quad (23)$$

The calculations were performed by fixing a catalyst layer porosity of  $\varepsilon_p = 0.4$ , obtained from SEM images, and an axial dispersion coefficient estimated by a Péclet number of 100, which is a reasonable value for well-designed microreactors. The reactions included are listed below.



Based on thermodynamic calculations, the equilibrium constants of the ethanol oxidation and ethyl acetate formation were large, while the equilibrium constant for the diethyl ether and ethylene formation were smaller. However, since the conversion of ethanol to diethyl ether and ethylene was quite low, these two reactions were also considered irreversible.

All the reactions were modelled as being parallel processes. Turning to the conclusion of the kinetic modelling for the fixed bed reactor (Section 3.3), all the three rate expressions (Mars-van Krevelen, LHHW and power law) showed similar results with minor differences when concentrations were not high, therefore, in this microreactor study, the numerically best behaving one, the power law model was selected. The rate constants were presumed to obey the Arrhenius law (similar to eq. 16) to suppress the correlations between parameters:

The parameters to be estimated included the rate constants and the activation energies of the reactions. Both the ethanol conversion and selectivities of the products were selected to be the targets of the parameter estimation. The rate equations are listed below:

$$r_1 = k_1 C_{EtOH,S} C_{O_2,S}^{0.5} \quad (I)$$

$$r_2 = k_2 C_{EtOH,S} C_{Alde,S} C_{O_2,S} \quad (II)$$

$$r_3 = k_3 C_{EtOH,S}^2 \quad (III)$$

$$r_4 = k_4 C_{EtOH,S} \quad (IV)$$

The results after the parameter estimation along with the experimental analyses are shown in Figure 25. The difference between the experiments was the feed flow rate and, consequently, the residence time in the reactor. The temperature ramp was 1 °C/min, which was considered as being a generous enough time to guarantee the steady state prevailing. The temperature behavior for these parallel reactions was the exponential rise, which was described by the used modified Arrhenius law expressions for each parallel reaction.

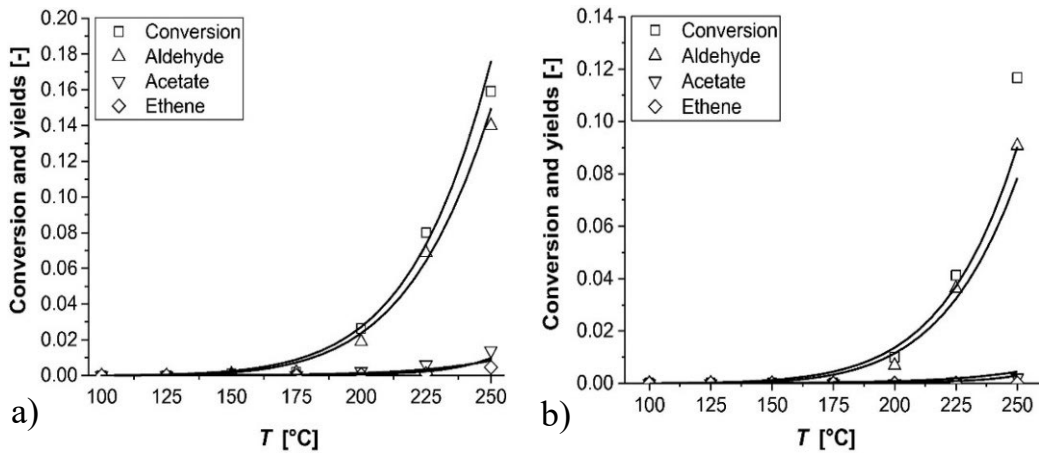


Figure 25. Ethanol conversion and products yields versus temperature at flow rate of a) 25 and b) 50 ml/min. The lines show the modelling and the marks show the experimental results

The ethanol conversion and the acetaldehyde yield (the dominating product) predicted by the model followed the experimentally observed trends reasonably well. The results of compounds present as tracer

components were calculated too. As it is evident, the respective trends were deviating a bit more, most probably due to more prominent analysis challenge.

The selectivity versus conversion plots (Figure 26) is in many cases more revealing, especially if consecutive reactions take place. Then an optimum for an intermediate can be detected. In our current case, only parallel reactions took place and, thus, the selectivity of the desired component under the studied circumstances remained approximately constant. The studied conversion range was limited by the reactor length and the flow rates. The model operated on the conservative side promising a slightly lower conversion than what was detected.

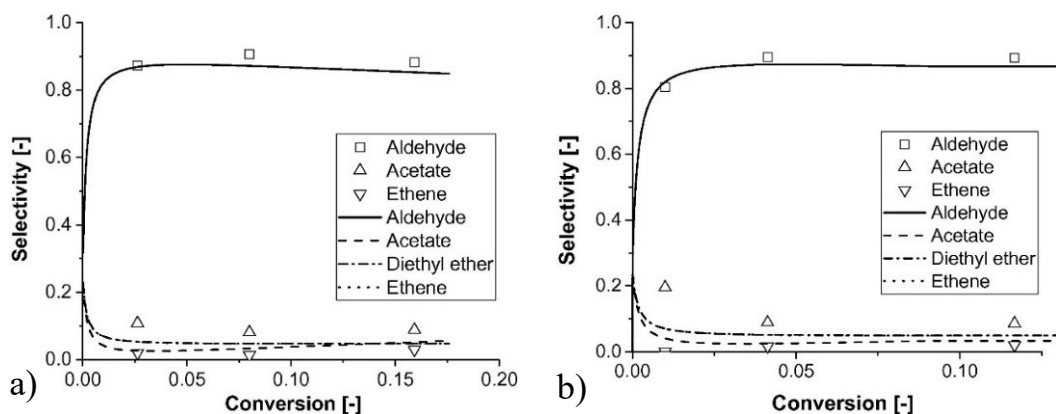


Figure 26. Products selectivity versus ethanol conversion at flow rate of a) 25 and b) 50 ml/min

Table 12 summarizes the parameter values for the dominant product acetaldehyde, and the minor compounds ethyl acetate and ethylene.

Table 12. The estimated parameters.  $T_{ref} = 423\text{ K}$

| Formation of  | $k_{ref,i} \pm 95\% \text{ confidence interval}$ | $E_{a,i} \text{ (kJ/mol)} \pm 95\% \text{ confidence interval}$ |
|---------------|--|---|
| Acetaldehyde  | $6.234 \cdot 10^{-5} \pm 0.572 \cdot 10^{-5}$    | $79110 \pm 2115$  |
| Ethyl acetate | $7.055 \cdot 10^{-9} \pm 0.453 \cdot 10^{-9}$    | $135400 \pm 15412$  |
| Ethylene      | $7.443 \cdot 10^{-4} \pm 0.675 \cdot 10^{-4}$    | $79900 \pm 4520$  |

### 3.4.2. Concentration profiles

The concentration profiles of ethanol and acetaldehyde as the main product as a function of the axial location and the time (or temperature) through the microchannels are illustrated in Figure 27. As the figure shows, at the lowest temperature of 150°C practically nothing happened, whereas, as the temperature was increased, the reaction progressed more and more rapidly. Because the conversion remained low (around 10 %) due to a short reactor length (1 cm), the gradients became more visible in the end as the temperature reached 250°C. The strongest exponential increase of the acetaldehyde generation was observed at the reactor outlet (Figure 27-b). Since the behavior of all the products was qualitatively similar, only the concentration of the main product is presented here. Figure 27-c depicts that the reaction rate increased as a function of the axial location. The rate increased exponentially as the temperature was increased and reached its highest level at 250°C. The maximum rate was at the reactor inlet and became smaller when approaching the outlet as the reactants, ethanol and oxygen were consumed gradually along the microreactor channel.

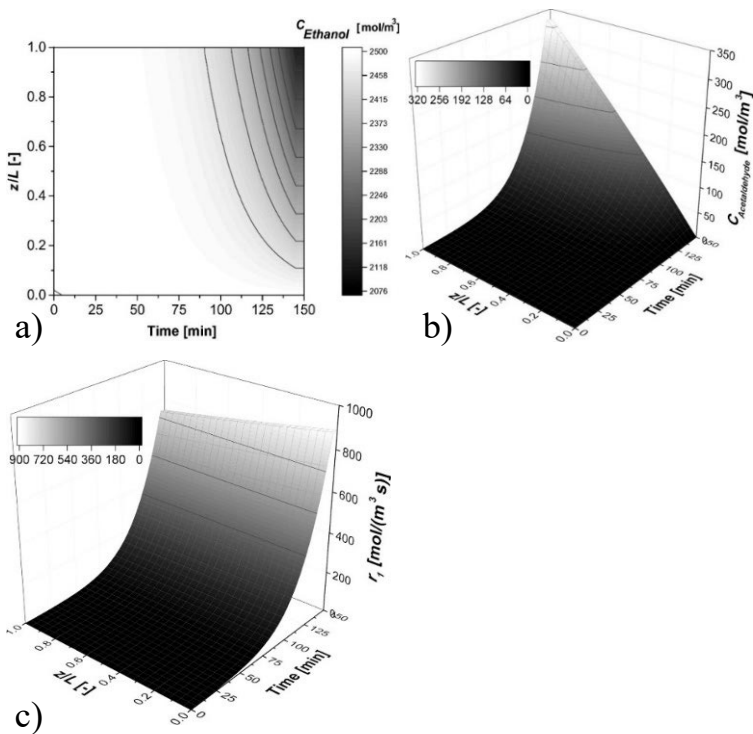


Figure 27. Concentration of a) ethanol, b) acetaldehyde and c) reaction rate of acetaldehyde as a function of time and axial location

### 3.5. Reaction mechanism by DFT studies

Atomic-level understanding of the reaction mechanisms and the nature of active sites is needed for the ethanol oxidation on gold catalysts to rationalize experimental results and to design better catalytic systems. Therefore, herein, the mechanism of oxidative dehydrogenation of ethanol on gold catalyst was analyzed with the density functional theory (DFT).

Bearing in mind that the key step in the alcohol oxidation is oxygen dissociation, which creates the reactive surface species, accordingly, the adsorption energies of  $O_2$  and EtOH on Au was calculated by taking into account both unassisted and assisted reaction paths. According to the calculations, the co-adsorption geometry with  $O_2$  on a top site is energetically more favorable and has the co-adsorption energy of -69 kJ/mol, which is -11 kJ/mol more exothermic than having reactants adsorbed separately. Both species undergo structural changes due to the co-adsorption.  $O_2$  transfers to a singlet electronic state, with the O-O bond length elongated by 0.05 Å compared to an individual adsorption geometry. The Au-O (ethanol) bond length decreases to 2.75 Å. Together these changes indicate that the interaction between the complex and Au(111) resembles chemisorption rather than physisorption. The DFT data clearly showed that unassisted  $O_2$  dissociation and O-H bond cleavage are unfeasible on Au(111) due to having very high activation (173 and 215 kJ/mol) and reaction energies (31 and 149 kJ/mol).

Figures 28 and 29 present a potential energy surface and mechanistic details of an assisted ethanol oxidation pathway, respectively. Starting from the co-adsorbed  $O_2$ -EtOH complex, the O-H bond breaks to form an adsorbed OOH-intermediate. In the most favorable pathway for the  $O_2$  assisted O-H bond cleavage,  $O_2$  stays on a bridge site during the reaction, while EtOH transfers from a top site to a tilted top site. As the activation energy is lower than the desorption energy for  $O_2$  and ethanol, the C-H bond cleavage is favored over desorption. Once the OOH species have been formed, it can break down rather easily to atomic oxygen and to a hydroxyl group. In the presence of EtO, the OOH decomposition has a barrier of 47 kJ/mol and the reaction is exothermic by -55 kJ/mol. On the bare Au(111) surface, the barrier is 64 kJ/mol and the reaction energy is -61 kJ/mol. This indicates that the presence of EtO helps the cleavage of the O-O bond probably by providing an additional H-bonding. Once the reactive oxygen species (O-H and O) have been formed, they can easily dissociate the O-H bond to form water or hydroxyl groups.

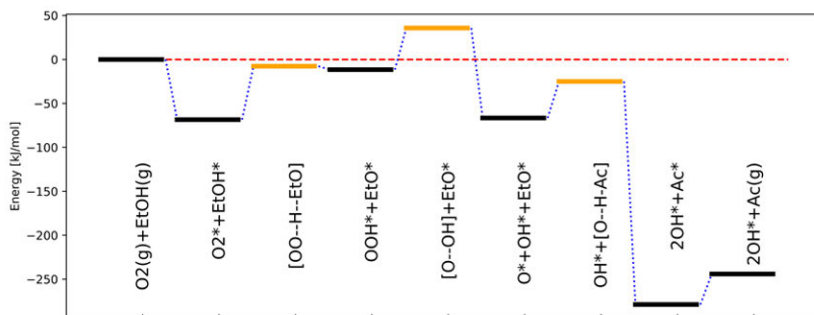


Figure 28. Minimum energy path for the assisted EtOH dehydrogenation. The black and orange bars correspond to minima and transition states, respectively. \* denotes adsorbed species, while (g) refers to gas phase species. Square brackets enclose a transition state structure where ‘- -’ marks the bond being broken

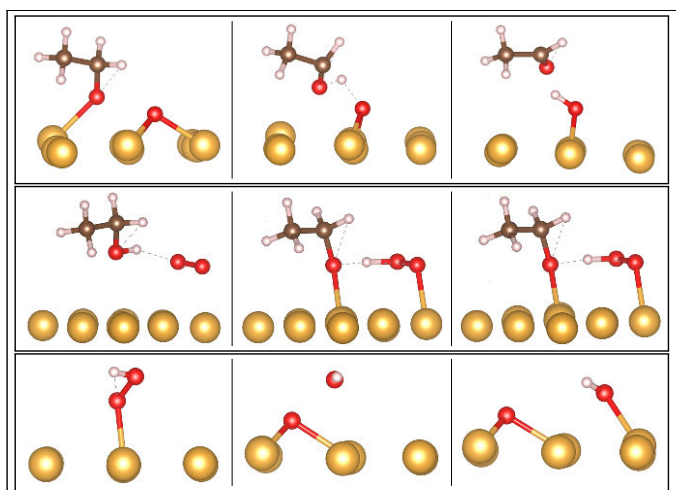


Figure 29. From top-to-bottom:  $\beta$ -H elimination forming acetaldehyde,  $O_2$  assisted O-H dissociation, and OOH dissociations. The left (right) image depicts the initial (final) state while the central image is the transition state. The dashed line indicates hydrogen bonding. The color scheme is as follows: Au atoms are yellow, C atoms brown, O atoms red, and H atoms white

The next step is the  $\beta$ -H elimination by an oxygen atom, a OH group or possibly OOH species. As the dissociation of OOH is proven to be facile, the most reactive species, namely an O atom has been investigated. The atomic oxygen readily breaks the C-H bond forming acetaldehyde. The barrier for C-H cleavage is 41 kJ/mol and the reaction is highly exothermic by -212 kJ/mol. In the present work, the energy for desorption of adsorbed acetaldehyde is 34 kJ/mol. The hydroxyl from OOH is the key intermediate in the path giving  $H_2O$ . The latter is formed after OH recombines with a second hydrogen via cleaving either

O-H or C-H bond, with low barriers ( $E_{act} \sim 10$  kJ/mol and  $E_{act} \sim 24$  kJ/mol [96], respectively). A single water molecule is weakly bound on the surface ( $E_{ads} = -33$  kJ/mol) and can desorb readily. The highly stable products, water and acetaldehyde, provide the thermodynamic driving force of the entire reaction scheme.

### 3.5.1. Role of oxygen: an experimental investigation

The role of oxygen was also experimentally revealed by exposing the Au/Al<sub>2</sub>O<sub>3</sub> (1.9 nm Au) catalyst to ethanol in the absence and presence of oxygen in the temperature range between 100–250°C.

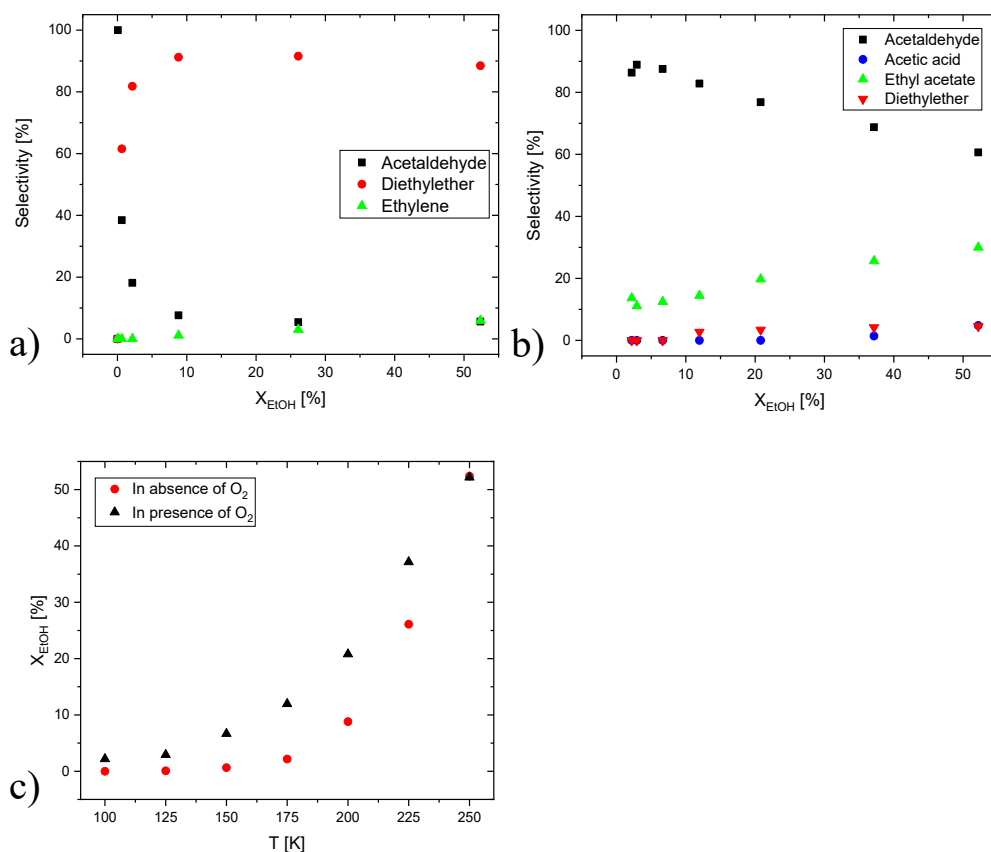


Figure 30. Selectivity in a) ethanol dehydrogenation in comparison with b) oxidative dehydrogenation as well as c) comparison of the conversions on the Au/Al<sub>2</sub>O<sub>3</sub> catalyst

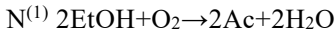
Figure 30 (a-b) demonstrates that in the absence of oxygen, etherification was the dominating reaction while in the presence of oxygen, ethanol oxidation and esterification reactions were dominant leading to

formation of acetaldehyde and ethyl acetate, respectively. As Figure 30-c illustrates, the oxidative dehydrogenation was more rapid than dehydrogenation indicating that the presence of oxygen lowers the activation energies of the key elementary steps.

### 3.5.2. Kinetic modelling

To further elucidate the kinetics associated with ethanol oxidation on the gold catalyst, a kinetic model was developed revisiting the previous data obtained using the microreactor, to explain the measured reaction rates towards the desired product, acetaldehyde. The mechanism behind the kinetic model was inspired by the computational studies and can be presented as follows:

|                                       | N <sup>(1)</sup> |
|---------------------------------------|------------------|
| 1. O <sub>2</sub> +*=O <sub>2</sub> * | 1                |
| 2. EtOH+*=EtOH*                       | 2                |
| 3. EtOH* + O <sub>2</sub> *→EtO*+OOH* | 2                |
| 4. OOH*+*→O*+OH*                      | 2                |
| 5. O*+EtO*→Ac+*+OH*                   | 2                |
| 6. 2OH*→O*+H <sub>2</sub> O+*         | 2                |
| 7. 2O*=O <sub>2</sub> *+*             | 1                |



where N<sup>(1)</sup> is the stoichiometric number of the elementary steps. Steps 1, 2 and 7 are considered to be at quasi-equilibria while steps 3-6 are irreversible. In the equation above, EtOH stands for ethanol, while Ac represents acetaldehyde and \* denotes a surface site.  $\theta_{\text{EtOH}}$ ,  $\theta_{\text{O}_2}$  and  $\theta_{\text{O}}$  correspond to the coverages of ethanol, dioxygen and oxygen, while  $\theta_V$  denotes the fraction of vacant sites.

Assuming the irreversible step 3 related to the formation of OOH species as the rate determining one the rate equation takes the form:

$$r^{(1)} = k_3 \theta_{\text{EtOH}} \theta_{\text{O}_2} = \frac{k_3 K_2 C_{\text{EtOH}} K_1 C_{\text{O}_2}}{(1 + K_2 C_{\text{EtOH}} + K_1 C_{\text{O}_2} + \sqrt{K_1 C_{\text{O}_2} / K_7})^2} \quad (24)$$

where  $k$  and  $K$  are the rate and equilibrium constants for respective steps,  $r^{(1)}$  stands for the overall reaction rate along the route N<sup>(1)</sup>.

As shown by the computational results, dioxygen does not readily dissociate on gold and hence the value of the equilibrium constant  $K_7$  is large. Consequently, the last term in the denominator of eq. 24 can safely be neglected resulting in the simplified rate equation:

$$r^{(I)} = \frac{k_3 K_2 C_{EtOH} K_1 C_{O_2}}{(1 + K_2 C_{EtOH} + K_1 C_{O_2})^2} = \frac{k_I C_{EtOH} C_{O_2}}{(1 + K_2 C_{EtOH} + K_1 C_{O_2})^2} \quad (25)$$

where  $k_I$  is a lumped constant ( $k_I = K_1 K_2 k_3$ ). According to eq. 25, based on the  $K_1$  values, the oxygen reaction order can vary in the range of -1 to 1 only, implying that in the oxidative dehydrogenation of ethanol, the reaction order of 1.81 respect to oxygen which was previously estimated using power law rate expression was uncertain (Table 11).

Preliminary calculations indicated that due to the limited experimental data the estimated values of  $K_1$  and  $K_2$  are not reliable. Therefore statistical analysis was conducted by the Monte Carlo Markov Chain (MCMC) method, the results of which are illustrated in Figure 31, showing the most probable values of constants as maxima.

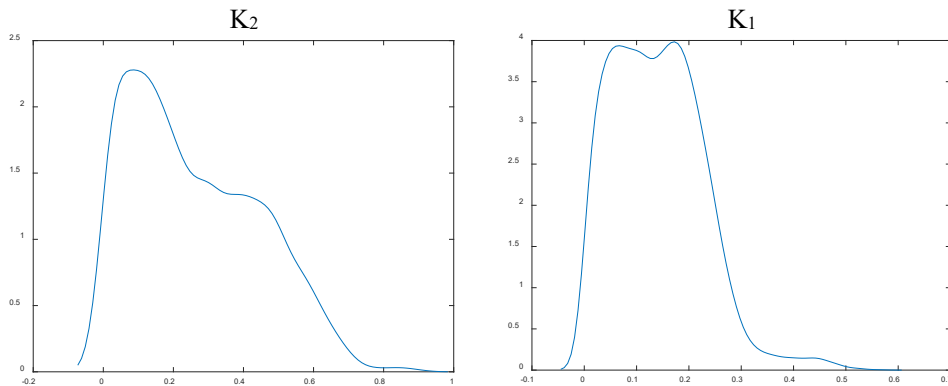
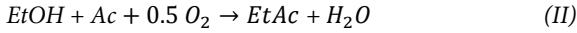


Figure 31. Statistical analysis of the adsorption constants by MCMC method

Based on statistical analysis the values of constants were fixed at  $K_1=0.17 \text{ m}^3/\text{mol}$ , and  $K_2=0.087 \text{ m}^3/\text{mol}$  during the parameter estimation.

The following reaction routes were taken into account in the kinetic modelling reflecting not only the main reaction, the acetaldehyde formation, but also the formation of the side products (ethyl acetate and diethyl ether) which occur on acid sites, as it was previously shown that oxidative dehydrogenation on  $Al_2O_3$  in the absence of gold nanoparticles is mainly selective towards diethyl ether, while the presence of both small gold nanoparticles and mild acid sites were found to be crucial for the formation of ethyl acetate.



where  $EtOH$ ,  $Ac$ ,  $EtAc$  and  $DEE$  are ethanol, acetaldehyde, ethyl acetate and diethyl ether, respectively. The formation of ethylene was neglected because it was obtained in trace amounts only. The following kinetic equations were considered in addition to eq. 25:

$$r^{(I)} = k_{II} C_{EtOH} C_{O_2} C_{Ac} \quad (26)$$

$$r^{(III)} = k_{III} C_{EtOH}^2 \quad (27)$$

The mass balances of the components are listed below assuming that there are no diffusion limitations and that the plug flow conditions prevailed in the microreactor channels.

$$\frac{d \dot{n}_{EtOH}}{dz} = m_{cat} (-r^I - r^{II} - 2r^{III}) \quad (28)$$

$$\frac{d \dot{n}_{Ac}}{dz} = m_{cat} (r^I - r^{II}) \quad (29)$$

$$\frac{d \dot{n}_{EtAc}}{dz} = m_{cat} r^{II} \quad (30)$$

$$\frac{d \dot{n}_{DEE}}{dz} = m_{cat} r^{III} \quad (31)$$

where  $m_{cat}$  is the catalyst mass,  $\dot{n}$  is the molar flow and  $z$  is the relative reactor length ( $z \in [0,1]$ ). The rate constants were presumed to obey the Arrhenius law using the mean temperature of 175°C in the parameter estimation.

The estimated values of the rate constants and the activation energies are listed in Table 13. The standard error corresponding to the second reaction was high implying that there was an apparent compensation effect between  $k_{II}$  and  $E_{a_{II}}$ . A large error could also be seen for the rate constant for route *III*. Such large errors can be associated with the slow rates of these side reactions. Based on the correlation matrix, the parameters were not correlated except the  $k$  and  $E_a$  of the same reactions. The results presented in Figure 32-a clearly demonstrate that the model was able to capture the experimental observations for the main reaction, ethanol oxidative dehydrogenation in an excellent way.

Table 13. Parameter estimation results, where  $k_i$  is the rate constant and  $E_a$  is the activation energy of the corresponding reactions

|                           | $k_I$<br>( $m^3 \cdot g^{-2} \cdot s^{-1}$ ) | $k_{II}$<br>( $m^6 \cdot mol^{-1} \cdot g^{-2} \cdot s^{-1}$ ) | $k_{III}$<br>( $m^6 \cdot mol^{-1} \cdot g^{-2} \cdot s^{-1}$ ) | $E_{a_I}$<br>(kJ/mol) | $E_{a_{II}}$<br>(kJ/mol) | $E_{a_{III}}$<br>(kJ/mol) |
|---------------------------|--|--|---|-----------------------|--------------------------|---------------------------|
| <b>Value</b>              | $1.25 \cdot 10^{-3}$                         | $0.25 \cdot 10^{-5}$   | $0.8 \cdot 10^{-4}$   | 83.7                  | 241                      | 94.8                      |
| <b>Standard error (%)</b> | 20.7   | >100   | >100  | 7                     | >100                     | 39.2                      |

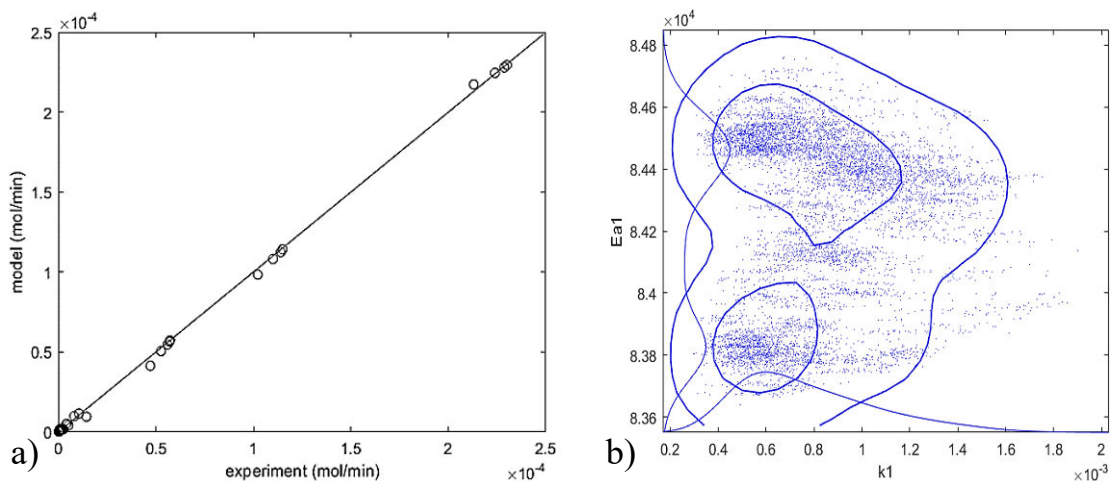


Figure 32. (a) Comparison between the kinetic model and the experimental data and (b) the sensitivity analysis by applying the Monte Carlo Markov Chain method

Statistical analysis by the Monte Carlo Markov Chain for the kinetic parameters is displayed in Figure 32-b. The parameter estimation results are usually described by contour plots relating two parameters, which

might in general have a mutual compensation. While elongated contour plots point out a strong correlation between parameters, the contours consisting of circles, as displayed in Figure 32-b for the main reaction, point out on a negligible correlation between the pre-exponential factor and the apparent activation energy.

### 3.5.3. Reaction and diffusion in the porous catalyst layer

Experimental data generated in a fixed bed reactor could in principle be influenced by external and internal mass transfer limitations. To confirm that the reaction was conducted in the kinetic regime and the regressed parameters correspond to the conditions of intrinsic kinetics, the concentration profiles in the catalyst layers with different thickness were calculated. A dynamic model for the reaction and internal diffusion was used to obtain the concentration profiles and get the insight in the dynamics of the porous catalyst layer. Because rather thin catalyst layers in the semi-elliptical channels are considered, the catalyst layer was regarded as a slab. The simulation results for the ethanol, oxygen, acetaldehyde and diethyl ether concentrations in the catalyst layers with 50–1500  $\mu\text{m}$  thickness are shown in Figure 33.

The simulations were done for the highest ethanol conversion i.e., the highest residence time (0.07 s) and temperature (250°C). The ethanol concentration profiles (Figure 33-a) indicate that there are no internal mass transfer limitations for the layer thicknesses less than 200  $\mu\text{m}$ , whereas for already layer thicknesses > 500  $\mu\text{m}$  the diffusion resistance becomes prominent. This implies that the oxidation process is retarded by internal diffusion in large-scale fixed beds where the catalyst particle diameters are typically larger than 1000  $\mu\text{m}$ . For oxygen molecule, however, due to its smaller diameter compare to ethanol, the internal diffusion limitation started for layer thicknesses > 800  $\mu\text{m}$  (Figure 33-b). For acetaldehyde a concentration maximum inside the catalyst layer was predicted in some cases, because acetaldehyde is an intermediate product (Figure 33-c).

As diffusion limitations might affect the activation energy of a reaction, herein, the activation energy obtained in this work was compared with the literature data. The activation energy (83.7 kJ/mol) is considerably higher than the values reported in the literature for the ethanol oxidation on different supported gold catalysts. An apparent activation energy of 35 kJ/mol over Au/MCM-41 within the temperature range of 170–185°C was reported by Guan and Hensen [97]. The apparent activation energies for different CeO<sub>2</sub> supported gold catalysts were in the range of 22–50 kJ/mol [98]. A similar value of the

apparent activation energy (49 kJ/mol) was observed for Au/SiO<sub>2</sub> catalyst at 120–180°C [99]. Although the average gold particle size (1.8 nm) was similar to the catalyst used in this study (~2 nm), the catalyst particle size was considerably larger (125–250 μm). The apparent activation energy for the oxidation of ethanol on Au/CeZr cordierite monolithic catalysts with unspecified thickness at 50–300°C was 84 kJ/mol in [100] similar to that of the current work. The difference in the activation energies might be correlated to the diffusion limitations. In the extreme case, the apparent activation energy is one half of the intrinsic one, which might explain the differences between the reported values of the activation energies in this work and the literature. However, it should be kept in mind that the apparent activation energy depends on the kinetic model used and can be rather different from the true activation energy [101]. Moreover, the activation energies should be compared at the same reactant concentrations and can also depend on the metal cluster size as well [102].

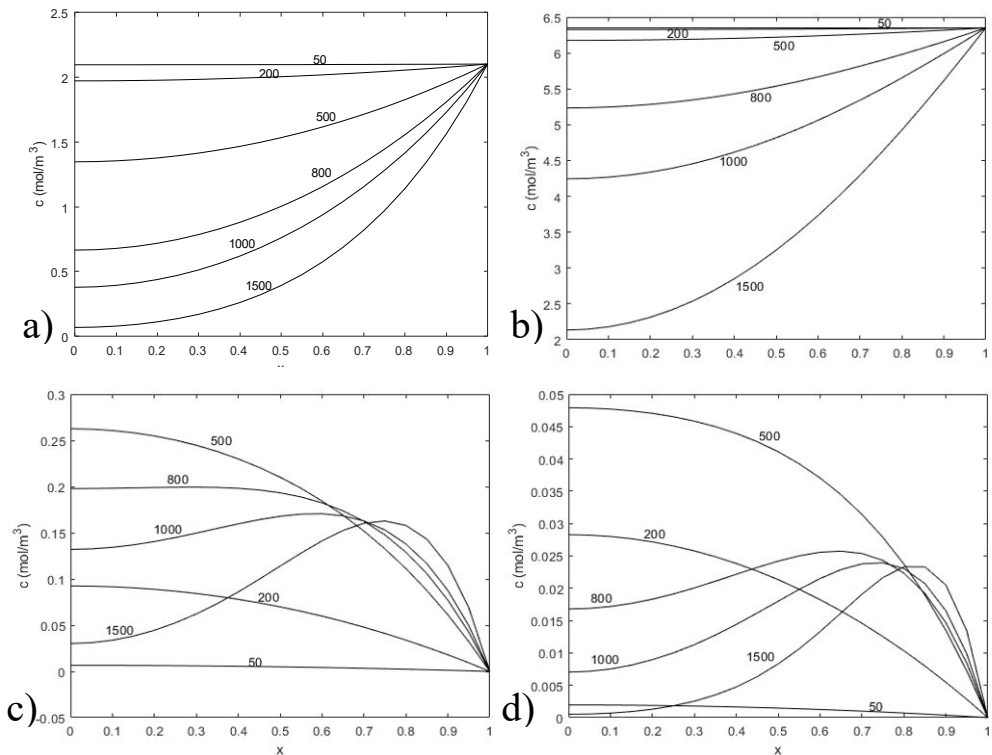


Figure 33. Concentration profiles of a) ethanol, b) oxygen, c) acetaldehyde and d) diethyl ether at 250°C inside the catalyst layer with different layer thicknesses (numbers are given in μm). The length coordinate equals to unity at the surface of the catalyst layer and becomes zero at the bottom of the layer



## **4. Conclusions**

## 4. Conclusions

This work was conducted to develop microreactor technology for partial oxidation of ethanol on gold catalyst. The first part of the thesis addresses the challenges in the gold catalyst preparation especially optimization of the gold particle size followed by catalyst screening in the fixed bed reactor and experimental kinetic studies. The second part was dedicated to the microreactor coating using the most promising catalyst in terms of the activity and selectivity from the screening section, and successfully conducted two coating methods. The reaction was tested in the coated microreactor with the aim of catalyst layer stability and durability evaluation as well as the kinetic studies. Thereafter, the kinetic modelling was performed for the fixed bed and the microreactor. In the end, the mechanism of ethanol oxidation was inspired by the computational studies and an improved kinetic model was developed revisiting the previous data obtained within the microreactor to explain the measured rate of acetaldehyde formation. The details of each section are summarized as follows.

A systematic study was conducted to reveal the effect of H-Y-80 zeolite surface charge as well as the pH of the solution on Au nanoparticles size and loading with a link to their activity and selectivity in the partial oxidation of ethanol. The effect of the catalyst support structure and acidity on activity and product selectivity were revealed. On strong acidic supports such as H-Y-12 and H-Beta 25 diethyl ether was the prevalent product. It is speculated that for generation of acetaldehyde and ethyl acetate using strong acid supports should be avoided. The structure sensitivity results showed that activity of Au/H-Y-80 and Au/Al<sub>2</sub>O<sub>3</sub> catalysts strongly depend on the Au particle size having the highest selectivity towards acetaldehyde. The catalyst activity was considerably increased for Al<sub>2</sub>O<sub>3</sub> when the Au particle size was reduced from 3.7 to 2.1 nm. Later on, it was demonstrated that the optimum Au particle size in terms of the activity is between 1.9 to 3.6 nm. A reduction in Au nanoparticle size from 9.3 to 6.3 nm was accompanied with an increase in TOF on Au/H-Y-80 catalysts.

Two catalytic microreactor coating technologies were applied based on Au/Al<sub>2</sub>O<sub>3</sub> as one of the most promising catalysts in terms of activity and selectivity towards the desired products. The first method was based on using a slurry of a pre-prepared Au/Al<sub>2</sub>O<sub>3</sub> catalyst without incorporation of any binders. It was demonstrated that the catalyst particle size and the viscosity of the catalyst slurry play a crucial role in

optimizing the coating uniformity. The drying rate and temperature were also decisive in the optimization of the coating uniformity. The second method was inkjet printing which was conducted by printing the alumina suspension into the microchannels followed by deposition of gold nanoparticles via deposition-precipitation. This method has the advantage of higher precision but a more complicated recipe since additives are necessary for having a stable suspension.

A physical model was developed for the laboratory-scale fixed bed reactor in the gas-phase oxidation of ethanol. The model was based on dynamic mass and energy balances and the reactions were assumed to take place within the porous catalyst particles. Three rate expressions namely LHHW, Mars van Krevelen and power law were used and the estimated parameters were compared. The model was tested against the experimental data obtained from catalyst screening studies. Parameter estimation results of all the three approaches were in line with the experimental observations and very similar. The reason that the kinetic approaches showed similar results was due to having a very diluted system. In other words, the concentration ranges were limited. The model was, thereafter, used in a sensitivity study to illustrate how the key parameters namely catalyst amount and Péclet number influenced the obtained results. Doubling the catalyst amount from 0.1 to 0.2 g caused an increase in the reaction rates and higher yields at lower temperatures. When the Péclet number was decreased from 10 to 1, the productivity was suppressed and higher temperatures were demanded to reach similar yields.

Microreactor modelling was also performed based on dynamic mass balance equation similarly to the model for the fixed bed reactor. The obtained selectivity for acetaldehyde formation was around 90 % at low temperatures. The mathematical model described the ethanol conversion and acetaldehyde selectivity in a reasonable agreement with the experimental observations.

The computational studies were carried out to understand the mechanism of oxidative dehydrogenation of ethanol over gold on alumina. The critical role of oxygen in the oxidative dehydrogenation was confirmed by experiments in the absence of oxygen demonstrating a low activity towards acetaldehyde and preferential dehydration to ethylene on acid sites of the catalyst support. In the presence of oxygen, acetaldehyde was the main product. Based on the combination of experimental and computational studies, it was revealed that the activation of molecular oxygen does not proceed on a bare gold but the presence of a hydrogen bond

donor *e.g.*, ethanol is needed to dissociate of molecular oxygen giving the reactive oxygen species required in oxidative dehydrogenation of ethanol to acetaldehyde.

The kinetic model developed on the basis of the mechanism, was completed with kinetic equations accounting for the formation of diethyl ether and ethyl acetate. Numerical data fitting demonstrated an adequate description of the experimental data with statistically well identified parameters. The value of the activation energy for the oxidative dehydrogenation for the experiments with the catalyst particles of ca. 30  $\mu\text{m}$  was 83.7 kJ/mol being significantly higher than reported in some previous studies. The experimentally determined activation energy for the formation of acetaldehyde, however, agrees very well with the value obtained from computational studies.

To assess the potential role of intraparticle mass transfer, performed simulations revealed that the role of mass transfer becomes prominent for catalyst particles exceeding 200  $\mu\text{m}$ , which implies that the current experimental work was carried out within the domain of intrinsic kinetics.

## 5. Notation

|                  |   |
|------------------|---|
| $A_p$            | Particle surface area [m <sup>2</sup> ]   |
| $Cat$            | Catalyst  |
| $C_{i,G}^0$      | Initial concentration of component $i$ in gas [mol/m <sup>3</sup> ]             |
| $C_{i,G}$        | Concentration of component $i$ in gas [mol/m <sup>3</sup> ]                     |
| $C_{i,G}^{IN}$   | Feed concentration of component $i$ in gas [mol/m <sup>3</sup> ]                |
| $C_{i,S}$        | Concentration inside the catalyst particle [mol/m <sup>3</sup> ]                |
| $C_{p,G}$        | Specific heat of gas phase [J/kg.K]   |
| $C_{p,B}$        | Specific heat of reactor bed [J/kg.K]   |
| $D_{eff,i}$      | Effective diffusivity of component $i$ [m <sup>2</sup> /s]                      |
| $D_i$            | Molecular diffusivity of component $i$ in gas phase [m <sup>2</sup> /s]         |
| $D_{A,B}$        | Molecular diffusivity of component A in B [m <sup>2</sup> /s]                   |
| $D_{r,G}$        | Radial dispersion coefficient [m <sup>2</sup> /s]                               |
| $D$              | Axial dispersion coefficient [m <sup>2</sup> /s]                                |
| $E_{a,j}$        | Activation energy of reaction $j$ [J/mol]                                       |
| $f$              | Function  |
| $f_p$            | Friction factor [-]   |
| $f_{active}$     | Active phase weight fraction [-]  |
| $\Delta H_{r,j}$ | Reaction enthalpy of reaction $j$ [kJ/mol]                                      |
| $i$              | Component $i$   |
| $k_1$            | Mars-van Krevelen rate parameter, [mol/g <sub>cat</sub> .s.bar]                 |
| $k_2$            | Mars-van Krevelen rate parameter, [mol/g <sub>cat</sub> .s.bar <sup>0.5</sup> ] |
| $k_3$            | Mars-van Krevelen rate parameter, [mol/g <sub>cat</sub> .s.bar]                 |
| $k'_1$           | LHHW rate parameter, [mol/g <sub>cat</sub> .s.bar <sup>1.5</sup> ]              |
| $k'_2$           | LHHW rate parameter, [mol/g <sub>cat</sub> .s.bar <sup>1.5</sup> ]              |
| $k'_3$           | LHHW rate parameter, [mol/g <sub>cat</sub> .s.bar]                              |
| $k_1^n$          | Power law rate parameter, [mol/g <sub>cat</sub> .s.bar <sup>m+1</sup> ]         |

|                 |   |
|-----------------|---|
| $k_2''$         | Power law rate parameter, [mol/g <sub>cat</sub> .s.bar <sup>n+1</sup> ] |
| $k_3''$         | Power law rate parameter, [mol/g <sub>cat</sub> .s.bar]                 |
| $k_{j,ref}$     | Mars-van Krevelen rate parameter at $T_{ref}$                           |
| $k'_{j,ref}$    | LHHW rate parameter at $T_{ref}$ ,                                      |
| $k''_{j,ref}$   | Power law rate parameter at $T_{ref}$ ,                                 |
| $K_i$           | Adsorption parameter for component $i$ [1/bar]                          |
| $L$             | Reactor length [m]  |
| $M_A, M_B$      | Molecular mass of component A and B [g/mol]                             |
| $N_{S,G,i}$     | Solid to gas molar flux of component $i$ [mol/m <sup>3</sup> .s]        |
| $p$             | Pressure [Pa]   |
| $\Delta p$      | Pressure drop [Pa]  |
| $PDE$           | Partial differential equation   |
| $Pe_G$          | Péclet number for gas [-]   |
| $P_{IN}$        | Initial pressure [Pa]   |
| $R$             | Reactor radius [m]  |
| $r$             | Radial location [m]   |
| $Re_p$          | Modified particle Reynolds number [-]                                   |
| $R_g$           | Ideal gas constant [J/mol.K]  |
| $r_j$           | Reaction $j$ rate[mol/g.s]  |
| $r_p$           | Radial location within particle [m]                                     |
| $R_p$           | Particle radius [m]   |
| $R_R$           | Reactor radius [m]  |
| $R_W$           | Reactor radius, catalyst coating layer included [m]                     |
| $s$             | Shape factor [-]  |
| $t$             | Time [s]  |
| $T_B, T_S, T_G$ | Temperature inside the catalyst bed, solid particle and gas             |
| $T_G^{IN}$      | Initial temperature [K]   |
| $T_{ref}$       | Reference temperature [403 K]   |

|                                   |   |
|-----------------------------------|---|
| $u_G^0$                           | Feed velocity of the gas phase [m/s]                            |
| $u_G$                             | Superficial gas velocity [m/s]                                  |
| $V$                               | Reactor volume [m <sup>3</sup> ]                                |
| $V_p$                             | Particle volume [m <sup>3</sup> ]                               |
| $w_{cat}$                         | Catalyst mass [g]   |
| $z$                               | Axial location [m]  |
| $\varepsilon_B$                   | Bed porosity [-]  |
| $\varepsilon_G$                   | Hold up of gas-phase [-]  |
| $\varepsilon_S$                   | Hold up of solid-phase [-]                                      |
| $\mu_G$                           | Viscosity of gas-phase [Pa.s]                                   |
| $\lambda_G, \lambda_S, \lambda_B$ | Thermal conductivity of the gas, solid and bed [W/m.K]          |
| $\lambda_{r,B}, \lambda_{z,B}$    | Radial and axial thermal conductivity of the bed [W/m.K]        |
| $\rho_G, \rho_S, \rho_B$          | Density of the gas, solid and bed [kg/m <sup>3</sup> ]          |
| $\rho_{cat}$                      | Catalyst concentration [kg/m <sup>3</sup> ]                     |
| $\nu_{i,j}$                       | Stoichiometric coefficient of component $i$ in reaction $j$ [-] |
| $\sum \nu_i$                      | Sum of the atomic contribution factors, $i=A$ or $B$            |

## 6. Acknowledgements

The present work was carried out at the Laboratory of Industrial Chemistry and Reaction Engineering, Johan Gadolin Process Chemistry Centre, Faculty of Science and Engineering, Åbo Akademi University between 2015 and 2019. The main part of the work was financed by the Graduate School in Chemical Engineering (GSCE), Academy of Finland (AKA) (Grant number 320115), Magnus Ehrnrooth Foundation and a scholarship provided by the Rector of Åbo Akademi. This research work is a part of the activities of Johan Gadolin Process Chemistry Centre (PCC) financed by Åbo Akademi University.



Magnus Ehrnrooth Foundation

## 7. References

- [1] R. Sheldon, I. Arends, G.-J. Ten Brink and A. Dijkstra, "Green, catalytic oxidations of alcohols," *Accounts of Chemical Research*, vol. 35, p. 774–781, 2002.
- [2] R. Sheldon, "Recent advances in green catalytic oxidations of alcohols in aqueous media," *Catalysis Today*, vol. 247, p. 4–13, 2014.
- [3] X. Yao, C. Bai, J. Chen and Y. Li, "Efficient and selective green oxidation of alcohols by MOF-derived magnetic nanoparticles as a recoverable catalyst," *RSC Advances*, vol. 6, p. 26921–26928, 2016.
- [4] J. Escobar, E. Lora, O. Venturini, E. Yanez, E. Castillo and O. Almazan, "Biofuels: Environment, technology and food security," *Renewable and Sustainable Energy Reviews*, vol. 13, p. 1275–1287, 2009.
- [5] "Global energy transformation: A roadmap to 2050," International Renewable Energy Agency (IRENA), Abu Dhabi, 2018.
- [6] C. Christensen, B. Jørgensen, J. Rass-Hansen, K. Egeblad, R. Madsen, S. Klitgaard, S. Hansen, M. Hansen, A. H.C and A. Riisager, "Formation of acetic acid by aqueous-phase oxidation of ethanol with air in the presence of a heterogeneous gold catalyst," *Angewandte Chemie International Edition*, vol. 45, p. 4648–4651, 2006.
- [7] "Acetaldehyde, Chemical Economics Handbook," IHS Markit, 2016. [Online]. Available: <https://ihsmarkit.com/products/acetaldehyde-chemical-economics-handbook.html>.
- [8] "Rising use of acetaldehyde in the production of various organic chemicals, sustain market growth," Global Industry analysts, Inc, 2019. [Online]. Available: <https://www.strategy.com/MarketResearch/ViewInfoGraphNew.asp?code=MCP-2007>
- [9] S. Sharma and V. Jaiswal, "Production of acetaldehyde," 2013. [Online]. Available: <https://www.scribd.com/document/292431457/Production-of-acetaldehyde>.
- [10] I.-T. Trotus, T. Zimmermann and F. Schuth, "Catalytic reactions of acetylene: A feedstock for the chemical," *Chemical Reviews–ACS Publications*, vol. 114, p. 1761–1782, 2014.
- [11] M. Eckert, G. Fleischmann, R. Jira, H. Bolt and K. Golka, "Acetaldehyde," in *Ullmann's Encyclopedia of Industrial Chemistry*, Weinheim, Wiley-VCH Verlag GmbH & Co. KGaA, 2012, p. 191–207.
- [12] K. Weissmehl and H.-J. Arpe, *Industrial organic chemistry*, Chapter 7, 4th ed., Weinheim: Wiley-VCH, 2003.

- [13] "Ethyl acetate market research report," Market Research Future, 2019. [Online]. Available: <https://www.marketresearchfuture.com/reports/ethyl-acetate-market-945>.
- [14] "Ethyl acetate market size, industry analysis report," Global Marker Insights, 2017. [Online]. Available: <https://www.gminsights.com/industry-analysis/ethyl-acetate-market>.
- [15] S. Fokin, "Catalytic oxidation reaction at high temperatures," *Russian Journal of Physical Chemistry*, vol. 45, p. 286–288, 1913.
- [16] R. Augustine, "Whither goest thou, catalysis," *Catalysis Letters*, vol. 146, p. 2393–2416, 2016.
- [17] P. Sabatier, *La catalyse en chimie organique*, Beranger, Paris, 1913.
- [18] P. Sabatier (translated by E.E: Reid), *Catalysis in organic chemistry*, Van Nostrand, New York, 1922.
- [19] G. Hutchings, "Vapor phase hydrochlorination of acetylene: Correlation of catalytic activity of supported metal chloride catalysts," *Journal of Catalysis*, vol. 96, p. 292–295, 1985.
- [20] M. Haruta, T. Kobayashi, H. Sano and N. Yamada, "Novel gold catalysts for the oxidation of carbon monoxide at a temperature far below 0°C," *Chemistry Letters*, vol. 16, p. 405–408, 1987.
- [21] S. Shahzad, M. Sajid, Z. Khan and D. Canseco-Gonzalez, "Gold catalysis in organic transformations: A review," *Synthetic Communications*, vol. 47, p. 735–755, 2017.
- [22] Y. Zhang, X. Cui, F. Shi and Y. Deng, "Nano-gold catalysis in Fine chemical synthesis," *Chemical Reviews*, vol. 112, p. 2467–2505, 2012.
- [23] R. Ciriminna, E. Falletta, C. Della Pina, J. Teles and M. Pagliaro, "Industrial applications of gold catalysis," *Angewandte Chemie International Edition*, vol. 55, p. 14210–14217, 2016.
- [24] G. Bond, "Gold-catalysed oxidation of carbon monoxide," *Gold Bulletin*, vol. 33, p. 41–50, 2000.
- [25] S. Scirè, C. Crisafulli, S. Minicò, G. Condorelli and A. Di Mauro, "Selective oxidation of CO in H<sub>2</sub>-rich stream over gold/iron oxide: An insight on the effect of catalyst pretreatment," *Journal of Molecular Catalysis A: Chemical*, vol. 284, p. 24–32, 2008.
- [26] R. Waters, J. Weimer and J. Smith, "An investigation of the activity of coprecipitated gold catalysts for methane oxidation," *Catalysis Letters*, vol. 30, p. 181–188, 1995.
- [27] B. Nkosi, N. Coville, G. Hutchings, M. Adams, J. Friedl and F. Wagner, "Hydrochlorination of acetylene using gold catalysts: A study of catalyst deactivation," *Journal of Catalysis*, vol. 128, p. 366–377, 1991.

- [28] B. Solsona, J. Edwards, P. Landon, A. Carley, A. Herzing, C. Kiely and G. Hutchings, "Direct synthesis of hydrogen peroxide from H<sub>2</sub> and O<sub>2</sub> using Al<sub>2</sub>O<sub>3</sub> supported Au-Pd catalysts," *Chemistry of Materials*, vol. 18, p. 2689–2695, 2006.
- [29] Y. Cao, X. Liu, S. Iqbal, P. Miedziak, J. Edwards, R. Armstrong, D. Morgan, J. Wang and G. Hutchings, "Base-free oxidation of glucose to gluconic acid using supported gold catalysts," *Catalysis Science and Technology*, vol. 6, p. 107–117, 2016.
- [30] Y. Zhao, M. Mann, J. Pavlish, B. Mibeck, G. Dunham and E. Olson, "Application of gold catalyst for mercury oxidation by chlorine," *Environmental Science and Technology*, vol. 40, p. 1603–1608, 2006.
- [31] Z. Hao, D. Cheng, Y. Guo and Y. Liang, "Supported gold catalysts used for ozone decomposition and simultaneous elimination of ozone and carbon monoxide at ambient temperature," *Applied Catalysis B: Environmental*, vol. 33, p. 217–222, 2001.
- [32] J. Leerat, S. Osuwan and E. Gulari, "Lean-burn NO<sub>x</sub> reduction by propene over gold supported on alumina catalysts derived from the sol–gel method," *Catalysis Letters*, vol. 141, p. 62–67, 2011.
- [33] J. Bravo-Suárez, K. Bando, J. Lu, T. Fujitani and S. Oyama, "Oxidation of propane to propylene oxide on gold catalysts," *Journal of Catalysis*, vol. 255, p. 114–126, 2008.
- [34] J. Jia, K. Haraki, J. Kondo, K. Domen and K. Tamaru, "Selective hydrogenation of acetylene over Au/Al<sub>2</sub>O<sub>3</sub> catalyst," *Journal of Physical Chemistry*, vol. 104, p. 11153–11156, 2000.
- [35] Y. Segura, N. López and J. Pérez-Ramírez, "Origin of the superior hydrogenation selectivity of gold nanoparticles in alkyne + alkene mixtures: Triple- versus double-bond activation," *Journal of Catalysis*, vol. 247, p. 383–386, 2007.
- [36] T. Thuening and W. Tysoe, "Vinyl acetate formation on Au/Pd(100) alloy surfaces," *Catalysis Letters*, vol. 148, p. 79–89, 2018.
- [37] F. Tao and Z. Ma, "Water–gas shift on gold catalysts: catalyst systems and fundamental studies," *Physical Chemistry Chemical Physics*, vol. 15, p. 15260–15270, 2013.
- [38] O. Simakova, R. Davis and D. Murzin, *Biomass processing over gold catalysts*, Heidelberg: Springer, 2013.
- [39] A. Lackmann, C. Mahr, M. Schowalter, L. Fitzek, J. Weissmüller, A. Rosenauer and A. Wittstock, "A comparative study of alcohol oxidation over nanoporous gold in gas and liquid phase," *Journal of Catalysis*, vol. 353, p. 99–106, 2017.

- [40] S. Meenakshisundaram, E. Nowicka, P. Miedziak, G. Brett, R. Jenkins, N. Dimitratos, S. Taylor, D. Knight, D. Bethell and G. Hutchings, "Oxidation of alcohols using supported gold and gold-palladium nanoparticles," *Faraday Discussions*, vol. 145, p. 341–356, 2010.
- [41] A. Abad, A. Corma and H. García, "Catalyst parameters determining activity and selectivity of supported gold nanoparticles for the aerobic oxidation of alcohols: The molecular reaction mechanism," *Chemistry-A European Journal*, vol. 14, p. 212–222, 2008.
- [42] J. Sun, X. Tong, Z. Liu, S. Liao and S. Xue, "Gold-catalyzed selectivity-switchable oxidation of benzyl alcohol in the presence of molecular oxygen," *Catalysis Communications*, vol. 85, p. 70–74, 2016.
- [43] E. Behraves, N. Kumar, Q. Balme, J. Roine, J. Salonen, A. Schukarev, J. Mikkola, M. Peurla, A. Aho, K. Eränen, D. Murzin and T. Salmi, "Synthesis and characterization of Au nano particles supported catalysts for partial oxidation of ethanol: Influence of solution pH, Au nanoparticle size, support structure and acidity," *Journal of Catalysis*, vol. 353, p. 223–238, 2017.
- [44] M. Alhumaimess, Z. Lin, W. Weng, N. Dimitratos, N. Dummer, S. Taylor, J. Bartley, C. Kiely and G. Hutchings, "Oxidation of benzyl alcohol by using gold nanoparticles supported on ceria foam," *CHEMSUSCHEM*, vol. 5, p. 125–131, 2012.
- [45] S. Klitgaard, A. DeLa Riva, S. Helveg, R. Werchmeister and C. Christensen, "Aerobic oxidation of alcohols over gold catalysts: Role of acid and base," *Catalysis Letters*, vol. 126, p. 213–217, 2008.
- [46] M. Personick, R. Madix and C. Friend, "Selective oxygen-assisted reactions of alcohols and amines catalyzed by metallic gold: Paradigms for the design of catalytic processes," *ACS Catalysis*, vol. 7, p. 965–985, 2017.
- [47] K. Sakata, K. Tada, S. Yamada, Y. Kitagawa, T. Kawakami, S. Yamanaka and M. Okumura, "DFT calculations for aerobic oxidation of alcohols over neutral Au<sub>6</sub> cluster," *Molecular Physics*, vol. 112, p. 385–392, 2014.
- [48] C. Shang and Z. Liu, "Origin and activity of gold nanoparticles as aerobic oxidation catalysts in aqueous solution," *Journal of the American Chemical Society*, vol. 133, p. 9938–9947, 2011.
- [49] E. Cao, M. Sankar, S. Firth, K. Fung Lam, D. Bethell, D. Knight, G. Hutchings, P. McMillan and A. Gavriilidis, "Reaction and Raman spectroscopic studies of alcohol oxidation on gold-palladium catalysts in microstructured reactors," *Chemical Engineering Journal*, vol. 167, p. 734–743, 2011.
- [50] D. Enache, J. Edwards, P. Landon, B. Solsona-Espriu, A. Carley, A. Herzing, M. Watanabe, C. Kiely, D. Knight and G. Hutchings, "Solvent-free oxidation of primary alcohols to aldehydes using Au-Pd/TiO<sub>2</sub> catalysts," *Science*, vol. 311, p. 362–365, 2006.

- [51] L. Prati, A. Villa, C. Campione and P. Spontoni, "Effect of gold addition on Pt and Pd catalysts in liquid phase oxidations," *Topics in Catalysis*, vol. 44, p. 319–324, 2007.
- [52] F. Boccuzzi, C. A. S. Tsubota and M. Haruta, "FTIR study of carbon monoxide oxidation and scrambling at room temperature over gold supported on ZnO and TiO<sub>2</sub>," *Journal of Physical Chemistry*, vol. 100, p. 3625–3631, 1996.
- [53] A. Sanchez, S. Abbet, U. Heiz, W. Schneider, H. Hakkinen, R. Barnett and U. Landman, "When gold is not noble: Nanoscale gold catalysts," *Journal of Physical Chemistry*, vol. 103, p. 9573–9578, 1999.
- [54] W. Ehrfeld, V. Hessel and H. Löwe, *Microreactors: New technologies for modern chemistry*, Weinheim,: Wiley-VCH, 2004.
- [55] M. Saber, J. Commenge and L. Falk, "Microreactor numbering-up in multi-scale networks for industrial-scale applications: Impact of flow maldistribution on the reactor performances," *Chemical Engineering Science*, vol. 65, p. 372–379, 2010.
- [56] B. Sun, J. Jiang, N. Shi and W. Xu, "Application of microfluidics technology in chemical engineering for enhanced safety," *Process Safety Progress*, vol. 35, p. 365–373, 2016.
- [57] T. Illg, A. Knorr and L. Fritzsche, "Microreactors- A powerful tool to synthesize peroxy-carboxylic esters," *Molecules*, vol. 21, p. 5–21, 2016.
- [58] B. Sun, H. Zhu, W. Liang, X. Zhang, J. Feng and W. Xu, "A safe and clean way to produce H<sub>2</sub>O<sub>2</sub> from H<sub>2</sub> and O<sub>2</sub> within the explosion limit range," *International Journal of Hydrogen Energy*, vol. 44, p. 19547–19554, 2019.
- [59] D. Kubička, N. Kumar, P. Mäki-Arvela, M. Tiitta, V. Niemi, T. Salmi and D. Murzin, "Ring opening of decalin over zeolites: I. Activity and selectivity of proton-form zeolites," *Journal of Catalysis*, vol. 222, p. 65–79, 2004.
- [60] C. Emeis, "Determination of integrated molar extinction coefficients for infrared adsorption bands of pyridine adsorbed on solid acid catalysts," *Journal of Catalysis*, vol. 141, p. 347–357, 1993.
- [61] J. R. Anderson, *Structure of metallic catalysts*, London: Academic Press, 1975.
- [62] A. Aho, N. Kumar, K. Eränen, T. Salmi, M. Hupa and D. Murzin, "Catalytic pyrolysis of woody biomass in a fluidized bed reactor: Influence of the zeolite structure," *Fuel*, vol. 87, p. 2493–2501, 2008.
- [63] M. Stekrova, N. Kumar, A. Aho, L. Sinev, W. Grünert, J. Dahl, J. Roine, S. Arzumanov, P. Mäki-Arvela and D. Murzin, "Isomerization of  $\alpha$ -pinene oxide using Fe-supported catalysts: Selective synthesis of campholenic aldehyde," *Applied Catalysis A: General*, vol. 470, p. 162–176, 2014.

- [64] V. Sobolev, K. Koltunov, O. Simakova, A. Leino and D. Murzin, "Low temperature gas-phase oxidation of ethanol on Au/TiO<sub>2</sub>," *Applied Catalysis A: General*, Vols. 433-434, p. 88–95, 2012.
- [65] V. Nieminen, N. Kumar, J. Datka, J. Päivärinta, M. Hotokka, E. Laine, T. Salmi and D. Murzin, "Active copper species in 1-butene skeletal isomerization: Comparison between copper-modified MCM-41 and beta catalysts," *Microporous and Mesoporous Materials*, vol. 60, p. 159–171, 2003.
- [66] A. Auroux, A. Gervasini and C. Guimon, "Acidic character of metal-loaded amorphous and crystalline silica-aluminas determined by XPS and adsorption calorimetry," *Journal of Physical Chemistry B*, vol. 103, p. 7195–7205, 1999.
- [67] D. Kubička, N. Kumar, T. Venäläinen, H. Karhu, I. Kubičková, H. Österholm and D. Murzin, "Metal-support interactions in zeolite-supported noble metals: Influence of metal crystallites on the support acidity," *Journal of Physical Chemistry B*, vol. 110, p. 4937–4946, 2006.
- [68] D. Kubička, N. Kumar, P. Mäki-Arvela, M. Tiitta, V. Niemi, H. Karhu, T. Salmi and D. Murzin, "Ring opening of decalin over zeolites-II. Activity and selectivity of platinum-modified zeolites," *Journal of Catalysis*, vol. 227, p. 313–327, 2004.
- [69] T. Kuzniatsova, Y. Kim, K. Shqau, P. Dutta and H. Verweij, "Zeta potential measurements of zeolite Y: Application in homogeneous deposition of particle coatings," *Microporous and Mesoporous Materials*, vol. 103, p. 102–107, 2007.
- [70] L. Lebovka, "Aggregation of charged colloidal particles," in *Polyelectrolyte complexes in the dispersed and solid state I*, *Advances in polymer science*, N. Müller, Ed., Verlag, Advances in Polymer Science, 2014, p. 57–96.
- [71] F. Moreau, G. Bond and A. Taylor, "Gold on titania catalysts for the oxidation of carbon monoxide: Control of pH during preparation with various gold contents," *Journal of Catalysis*, vol. 231, p. 105–114, 2005.
- [72] A. Kraynov and T. Muller, "Concepts for the stabilization of metal nanoparticles in ionic liquids," in *Applications of Ionic Liquids in Science and Technology*, S. Handy, Ed., Rijeka, InTech, 2011, p. 235–260.
- [73] Y. Nechayev and G. Zvonareva, "Adsorption of gold (III) chloride complexes on a hematite," *Geokhimiya*, vol. 6, p. 919, 1983.
- [74] T. Noda, K. Suzuki, N. Katada and M. Niwa, "Combined study of IRMS-TPD measurement and DFT calculation on Brønsted acidity and catalytic cracking activity of cation-exchanged Y zeolites," *Journal of Catalysis*, vol. 259, p. 203–210, 2008.

- [75] S. Kim, D. Robichaud, G. Beckham, R. Paton and M. Nimlos, "Ethanol dehydration in HZSM-5 studied by density functional theory: evidence for a concerted process," *Journal of Physical Chemistry A*, vol. 119, p. 3604–3614, 2015.
- [76] M. Christiansen, G. Mpourmpakis and D. Vlachos, "Density functional theory-computed mechanisms of ethylene and diethyl ether formation from ethanol on  $\gamma$ -Al<sub>2</sub>O<sub>3</sub>(100)," *ACS Catalysis*, vol. 3, p. 1965–1975, 2013.
- [77] J. Huang, Y. Jiang, V. Reddy Marthala, A. Bressel, J. Frey and M. Hunger, "Effect of pore size and acidity on the coke formation during ethylbenzene conversion on zeolite catalysts," *Journal of Catalysis*, vol. 263, p. 277–283, 2009.
- [78] G. Ertl, H. Knözinger, F. Schüth and J. Weitkamp, *Handbook of Heterogeneous Catalysis*, Weinheim: VCH, 2008.
- [79] Z. Zhou, P. Scales and D. Boger, "Chemical and physical control of the rheology of concentrated metal oxide suspensions," vol. 56, p. 2901–2920, 2001.
- [80] J. Yuan and H. Murray, "The importance of crystal morphology on the viscosity of concentrated suspensions of kaolins," *Applied Clay Science*, vol. 12, p. 209–219, 1997.
- [81] W. Boersma, J. Lave and H. Stein, "Shear thickening (dilatancy) in concentrated dispersions," *American Institute of Chemical Engineers*, vol. 36, p. 321–332, 1990.
- [82] C. Agrafiotis and A. Tsetsekou, "The effect of processing parameters on the properties of  $\gamma$ -alumina washcoats deposited on ceramic honeycombs," *Journal of Materials Science*, vol. 35, p. 951–960, 2000.
- [83] X. Carrier, E. Marceau, J. F. Lambert and M. Che, "Transformations of  $\gamma$ -alumina in aqueous suspensions: 1. Alumina chemical weathering studied as a function of pH," *Journal of Colloidal and Interface Science*, vol. 308, p. 429–439, 2007.
- [84] J. M. Mieth, Y. J. Huang and J. A. Schwarz, "Experimental procedures to evaluate dissolution, metal ion buffering, and catalytic precursor speciation during catalyst preparation," *Journal of Colloid and Interface Science*, vol. 123, p. 366–379, 1988.
- [85] G. B.S, A. Subbotin and V. Yakerson, "On the phenomena of temperature hysteresis in hydrogenation reactions over heterogeneous catalysts," *Reaction Kinetics and Catalysis Letters*, vol. 68, p. 125–132, 1999.
- [86] T. Xu, J. Jin, C. Gregory, J. Hickman and T. Boland, "Inkjet printing of viable mammalian cells," *Biomaterials*, vol. 26, p. 93–99, 2005.

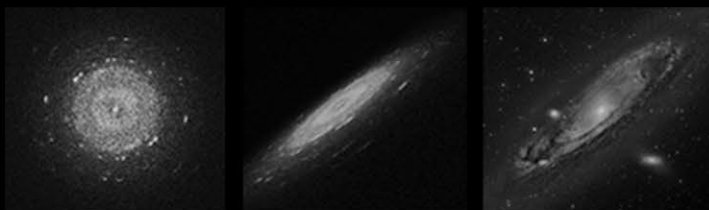
- [87] E. Tekin, P. Smith and U. Schubert, "Inkjet printing as a deposition and patterning tool for polymers and inorganic particles," *Soft Matter*, vol. 4, p. 703–713, 2008.
- [88] K. Woo, D. Kim, J. Kim, S. Lim and J. Moon, "Ink-jet printing of Cu–Ag-based highly conductive tracks on a transparent substrate," *Langmuir*, vol. 25, p. 429–433, 2009.
- [89] S. Lee, T. Boeltken, A. Mogalicherla, U. Gerhards, P. Pfeifer and R. Dittmeyer, "Inkjet printing of porous nanoparticle-based catalyst layers in microchannel reactors," *Applied Catalysis A: General*, vol. 467, p. 69–75, 2013.
- [90] G. Germani, A. Stefanescu, Y. Schuurman and A. van Veen, "Preparation and characterization of porous alumina-based catalyst coatings in microchannels," *Chemical Engineering Science*, vol. 62, p. 5084–5091, 2007.
- [91] T. Kilpiö, E. Behraves, V. Russo, K. Eränen and T. Salmi, "Physical modeling of the laboratory-scale packed bed reactor for partial gas-phase oxidation of alcohol using gold nanoparticles as the heterogeneous catalyst," *Chemical Engineering Research and Design*, vol. 117, p. 448–459, 2017.
- [92] E. Fuller, P. Schettler and J. Giddings, "New method for prediction of binary gas-phase diffusion coefficients," *Industrial & Engineering Chemistry*, vol. 58, p. 18–27, 1966.
- [93] C. Yaws, *Chemical properties handbook*, New York: McGraw-Hill, 1999.
- [94] B. Poling, J. Prausnitz and J. O'Connell, *Properties of gases and liquids*, New York: McGraw-Hill, 2001.
- [95] T. Salmi, J.-P. Mikkola and J. Wärnå, *Chemical reaction engineering and reactor technology*, Boca Raton: CRC Press, 2011.
- [96] C. R. Chang, X. F. Yang, B. Long and J. Li, "A water-promoted mechanism of alcohol oxidation on a Au(111) surface: Understanding the catalytic behavior of bulk gold," *ACS Catalysis*, vol. 3, p. 1693–1699, 2013.
- [97] Y. Guan and E. M. Hensen, "Ethanol dehydrogenation by gold catalysts: The effect of the gold particle size and the presence of oxygen," *Applied Catalysis A: General*, vol. 361, p. 49–56, 2009.
- [98] G. M. Mullen, E. J. Evans JR, B. C. Siegert, N. R. Miller, B. K. Rosselet, I. Sabzevari, A. Brush, Z. Duan and C. B. Mullins, "The interplay between ceria particle size, reducibility, and ethanol oxidation activity of ceria-supported gold catalysts," *Reaction Chemistry & Engineering*, vol. 3, p. 75–85, 2018.
- [99] Y. Guan and E. J. M. Hensen, "Selective oxidation of ethanol to acetaldehyde by Au–Ir catalysts," *Journal of Catalysis*, vol. 305, p. 135–145, 2013.

- [100] P. Topka and M. Klementová, "Total oxidation of ethanol over Au/Ce<sub>0.5</sub>Zr<sub>0.5</sub>O<sub>2</sub> cordierite monolithic catalysts," *Applied Catalysis A: General*, vol. 522, p. 130–137, 2016.
- [101] G. Bond, M. Keane, H. Kral and J. Lercher, "Compensation phenomena in heterogeneous catalysis: General principles and a possible explanation," *Catalysis Reviews*, vol. 42, p. 323–383, 2000.
- [102] D. Murzin, "On apparent activation energy of structure sensitive heterogeneous catalytic reactions," *Catalysis Letters*, vol. 149, p. 1455–1463, 2019.

# Development Of Microreactor Technology For Partial Oxidation Of Ethanol on Gold Catalyst

"The total number of minds in the universe is one. In fact, consciousness is a singularity phasing within all beings." – Erwin Schrödinger

Undoubtedly, nothing has been more astonishing for human being than the glorious space. Every detail designed in the cover is the product of imagination. Indeed, the galaxies shown in the cover are surprisingly nothing but electron diffractions of the gold on alumina catalyst. As shown below, the left picture is an electron diffraction which is rotated to be illustrated from the cross section (middle) in comparison with a real galaxy in space (right). Not a big difference is observed between the electron diffraction taken by a powerful microscope and a galaxy taken by a powerful telescope.



Interestingly, the shining stars at the top right are gold nanoparticles taken by a transmission electron microscope shown together with the real stars of the universe in the other parts of the cover.

Next is to assume a microchannel as a wormhole in space. A wormhole can be visualized as a tunnel with two ends at separate points in space-time (i.e., different locations, or different points in time, or both) which is actually the theory behind the idea of travelling in time. A wormhole could connect extremely long distances such as a billion light years or more, short distances such as a few meters, different universes, or different points in time. Considering the latter, this is analogously observed in microreactors since the reaction rate in microreactors is usually faster than in conventional ones. In other words, microreactors convert the given amounts of reactants to products in less time.

Finally, thought the wormhole/microchannel, we see the Earth our green home as one of the reasons of using microreactors is due to their positive environmental impacts in connection with replacement of fossil fuel-based sources with biomass for chemical production.

